ALMA MATER STUDIORUM
UNIVERSITÀ DI BOLOGNA

DOTTORATO DI RICERCA IN
INGEGNERIA BIOMEDICA, ELETTRICA E DEI SISTEMI

Ciclo XXXVI

Settore Concorsuale: 09/E1 - ELETTROTECNICA
Settore Scientifico Disciplinare:: ING-IND/31 - ELETTROTECNICA

ELECTRODYNAMIC ANALYSIS OF HTS CONDUCTORS FOR FUSION MAGNETS AND FOR NON INSULATED COILS

Presentata da: Antonio Macchiagodena

Coordinatore Dottorato
Prof. Michele Monaci

Supervisore
Prof. Marco Breschi

Co-supervisore
Prof. Pier Luigi Ribani

Esame finale anno 2024

A Lorena, Nicolino,
Iole, Regina,
Mario, Ottorino,
& Mario.

ACKNOWLEDGMENTS

Non ho mai scritto alcun ringraziamento nelle mie precedenti tesi perché non lo ho mai ritenuto necessario in quello che è prima di tutto un documento scientifico ed ufficiale. Tuttavia, essendo questa molto probabilmente l'ultima che scriverò credo sia opportuno porgere i miei ringraziamenti a chi ha reso possibile tutto ciò.

Per primo vorrei ringraziare il professore Marco Breschi che mi ha dato l'opportunità di svolgere questo percorso di crescita personale e lavorativa il cui frutto è racchiuso nel testo di questo documento. La mia collaborazione con il professor Breschi risale a ben prima dell'inizio di questo dottorato. Lo ringrazio quindi per tutte le opportunità datemi in precedenza e per avermi trasmesso una grande passione per lo studio non solo dei temi legati alla superconduttività ma dell'elettrotecnica tutta.

Voglio poi ringraziare il professore Pier Luigi Ribani, il cui contributo a questo lavoro è stato incalcolabile. Ma più di tutto voglio ringraziarlo per l'incredibile esperienza umana che mi ha fornito nei nostri continui dialoghi non sempre su temi ingegneristici. Le sue grandi capacità scientifiche, che ho avuto ben modo di apprezzare in prima persona, impallidiscono difronte alla grandissima caratura morale e umana della persona che più di tutti mi ha supportato e sopportato durante questo dottorato.

Ringrazio gli amici e colleghi che mi hanno aiutato durante questi anni. In particolare, Lorenzo che è stato una guida preziosa e sempre presente e Mattia con cui ho condiviso gioie e dolori di quella che è l'esperienza del dottorato.

Ringrazio poi il Dott. Gianluca De Marzi dell'ENEA, il suo contributo è stato determinante per lo sviluppo di questa tesi e per una mia crescita personale.

Ed infine, ultimi ma non ultimi, voglio ringraziare la mia famiglia tutta, a partire dai miei genitori i cui elogio non tesserò qui perché le mie abilità letterarie non ne sarebbero in grado. Un pensiero speciale va soprattutto a chi non ha potuto esserci durante il mio percorso, ma la cui presenza non è mai stata dimenticata.

Abstract

THE advent of high-temperature superconducting (HTS) materials has ushered in a new era of technological possibilities, propelling them to the forefront of cutting-edge scientific endeavors. HTS devices are frequently subjected to time-dependent transport currents and external magnetic fields during operation, leading to energy losses within the HTS, namely AC losses, a phenomenon that can potentially compromise device performance.

Accordingly, the development of robust tools for accurately estimating AC losses in HTS devices and predicting the behavior of the device during operation is of crucial importance. Conventional approaches, such as finite element method (FEM) models, offer commendable predictive capabilities, yet they suffer from substantial computational costs and are often not compatible with the time scale of the design and prototyping phases of HTS device development. The computational time of 3D FEM models is prohibitively high in the cases of complex magnet geometry like the central solenoid of a Tokamak fusion reactor.

To address this limitation, this thesis investigates alternative solutions: analytical formulae for the assessment of the instantaneous power dissipation, which were applied to study the losses in the central solenoid of the DEMO machine, and a 3D lumped parameter model employed in the study of tapes and no insulation HTS (NI-HTS) coils. The proposed solutions, although not accurate as a full 3D FEM model which remains the most reliable tool for the analysis of HTS devices, offer significant advantages over conventional approaches. The main advantages are reduced computational time, enhanced model flexibility, and improved scalability for complex device geometries.

Contents

List of Figures

List of Tables

1 *Introduction*

This introductory chapter aims to impart readers with a comprehensive grasp of superconductivity, empowering them to contextualize the work presented herein within the broader field of superconductivity and grasp the fundamental principles indispensable for comprehending the subsequent chapters.

1.1 Discovery of superconductivity

The discovery of superconductivity is credited to the Dutch physicist Heike Kamerlingh Onnes (recipient of the 1913 Nobel Prize in Physics), who made this groundbreaking observation in 1911. While conducting experiments on the electrical properties of various materials at low temperatures at Leiden University laboratories in the Netherlands, Onnes achieved a remarkable breakthrough in 1908 when he was the first to liquefy helium, the last of the inert gases to be condensed, reaching an astoundingly low temperature of 4.2 Kelvin. This significant milestone paved the way for a new era of scientific exploration by enabling researchers to conduct experiments at temperatures previously unattainable.

Three years later, in 1911, Onnes made another remarkable discovery when he observed an abrupt and dramatic drop in the electrical resistivity of mercury to negligible values, essentially becoming zero when the material was immersed in liquid helium (Onnes famously described this phenomenon as the "disappearance" of electrical resistance [22]. This remarkable observation, depicted in Fig. 1.1.1, which showcases Onnes's original data on the temperature dependence of mercury's electrical resistivity, defied the prevailing theories of the time, which predicted a gradual decrease in electrical resistance with decreasing temperature. Onnes concluded that mercury had entered a previously unknown state of matter, which he baptized "superconductivity." This phenomenon, however, was not observed in all materials, and it marked the emergence of a new class of materials known as superconductors.

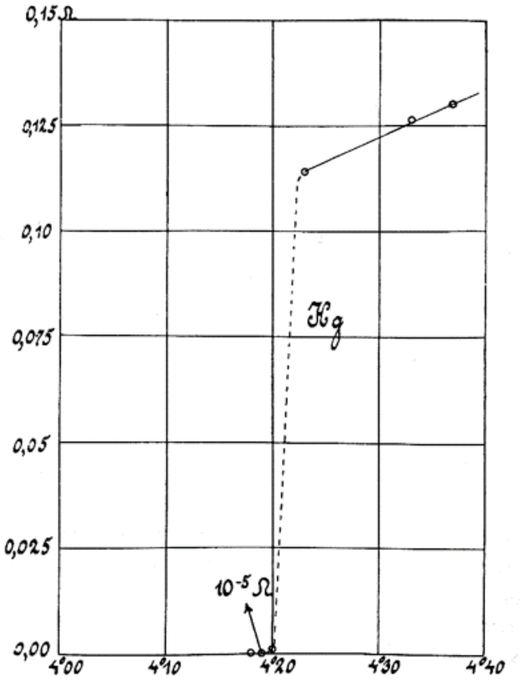

Figure 1.1.1: *Behaviour of the electrical resistance of mercury as a function of the temperature, as reported by H. K. Onnes in 1911* [1].

1.2 Superconducting propierties

After stating that superconductors are materials that exist in a different state of matter, it is important to define the properties of this state. The main difference between the superconducting materials and the others is a sudden variation of the electrical resistivity and perfect diamagnetism [23].

1.2.1 Superconducting transition of electrical resistivity

In classical electromagnetism theory, as the temperature of a material decreases, its electrical resistance diminishes due to the reduced vibrational motion of the ions in its crystal lattice structure.

However, for ordinary metallic conductors, the resistance does not entirely vanish at absolute zero (a temperature that cannot be practically attained) but rather approaches a residual value attributed to imperfections within the crystal lattice. Matthiessen's rule, shown in 1.2.1 serves as an empirical model to quantify this phenomenon [24]:

$$\rho = \rho_t + \rho_0 \tag{1.2.1}$$

Where ρ is the material resistivity, ρ_t is thermal resistivity, which tends to nullify tending to absolute zero, while the resistivity ρ_0 depends on the degree of purity of the crystal lattice. This last parameter can persist regardless of the temperature. In Fig. 1.2.1 the trend of the electrical resistance of an ordinary metal as a function of temperature is compared against that of an ideally pure metal ($\rho_0 = 0$) and a superconductor. It can be seen that when the superconducting material is cooled down below a certain value of temperature its resistance sharply drops to negligible values ($\rho <$ 10-25 Ωm). The temperature value at which the electrical resistance of the superconductor drops is called the critical temperature and is indicated as T_c.

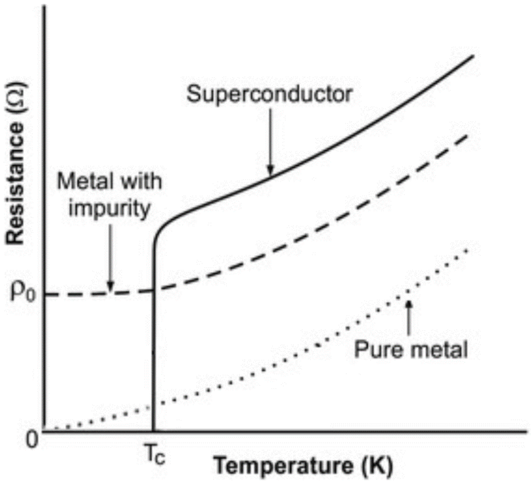

Figure 1.2.1: *Comparison of the electrical resistivity, as a function of temperature, of an ordinary metal an ideally pure metal and a superconductor.*

1.2.2 Perfect diamagnetism: The Meissner-Ochsenfeld effect

Perfect diamagnetism is an idealized property exhibited by hypothetical perfect conductors ($\rho = 0$), which theoretically can perfectly repel any external magnetic field penetrating their interior. However, this phenomenon is restricted, in the case of normal conductors, to materials cooled below a critical temperature (T_c) of approximately 0 Kelvin (absolute zero) before the external magnetic field is applied. If the cooling occurs after the field is applied, the magnetic field cannot be expelled from the material's interior.

In contrast, superconductors can expel an external magnetic field from their interior, regardless of whether the field is applied before or after the material is cooled below its critical temperature, which can be significantly higher than absolute zero. This remarkable phenomenon is known as the Meissner-Ochsenfeld effect [25]. The Meissner-Ochsenfeld effect, a superconductivity hallmark, encapsulates the fundamental distinction between perfect conductors and superconductors. It can be stated that this effect is what truly defines a superconductor even more than the sudden drop of electrical resistivity.

In Fig 1.2.2, the behavior of a perfect conductor, when subjected to an external magnetic field, is shown in comparison to that of a superconductor. The left side of Fig. 1.2.2 illustrates the response when the field is applied after both materials have been cooled below their respective critical temperatures. In contrast, the right side demonstrates the outcome when the field is applied before cooling.

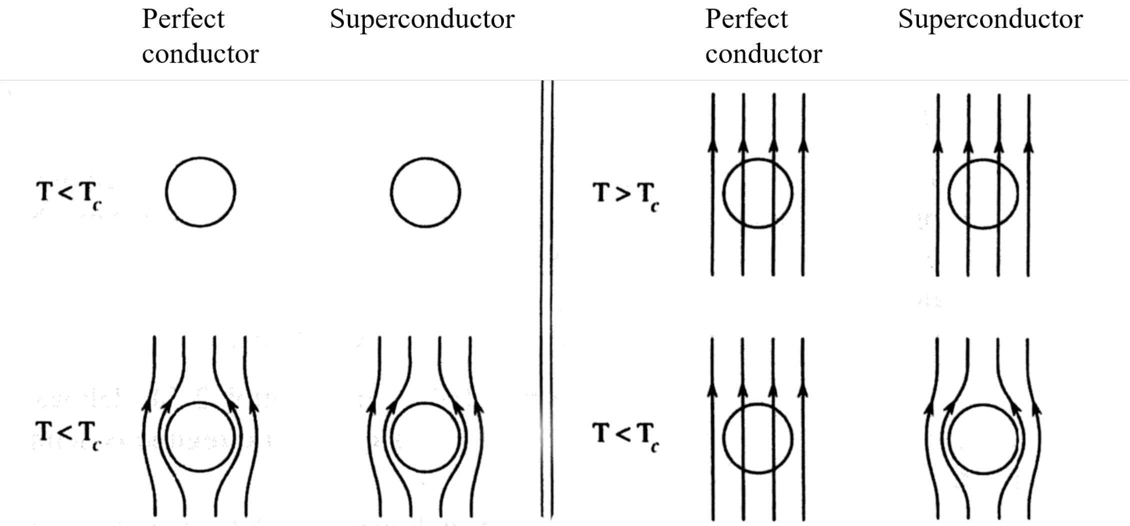

Figure 1.2.2: *Magnetic behavior of a perfect conductor, and a superconductor, when subjected to an external magnetic field, as function on the temperature.*

It is noteworthy that the distinction between a perfect conductor and a superconducting material extends to the underlying mechanisms that produce their diamagnetic properties. The fundamental origins of diamagnetism in superconductors and normal materials differ significantly. In normal materials, diamagnetism arises directly from the orbital motion of electrons around atomic nuclei, induced electromagnetically by the application of an external magnetic field. In superconductors, however, this illusion of perfect diamagnetism is not solely due to orbital spin but arises from the persistent flow of currents, called screening currents, that generates a magnetic field opposed to that applied(the Meissner-Ochsenfeld effect).

The word "illusion" is used to emphasize that in reality, a superconductor is not in a truly perfect diamagnetic state. While the interior of the superconductor expels the external magnetic field, a small residual field persists in a thin layer near the material's surface. This region is defined by a parameter known as the penetration depth, λ [26]. Within this distance, the magnetic field decays exponentially from its external strength to zero, as shown in Fig. 1.2.3.

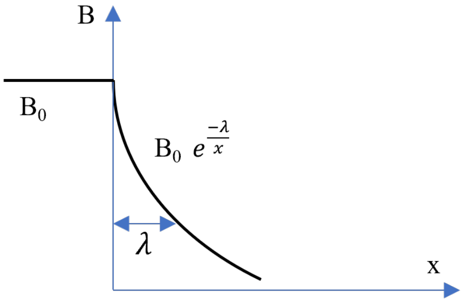

Figure 1.2.3: *Penetration depth and magnetic field inside a superconductor.* B_0 *is the value of the external magnetic field, inside the superconductor the magnetic field follows the exponential law reported in the figure.*

1.2.3 The critical surface: when a superconductor is such

As mentioned earlier, a superconducting material exhibits its peculiar properties only within specific operating conditions, characterized by a set of state variables. Specifically, the temperature, magnetic field, and current density must not exceed their critical values, denoted by T_c, B_c, and J_c, respectively. Exceeding any of these limits triggers the material's transition into a non-superconducting, dissipative state. These three parameters exhibit a strong interrelationship (e.g., increasing the operating temperature reduces the critical current density of the superconductor). Together, they define the so-called critical surface of the superconductor, depicted in Fig 1.2.4. The shape of the critical surface is dependent on the type of superconductor, the quality of the manufacturing process, the impurity content, and any potential damage incurred during operation.

It is important to note that the parameters defining the critical surface of a superconductor are typically measured as average values across the entire material, and often within a complex superconducting device. However, these parameters may vary locally within the material due to possible anisotropies or inhomogeneous manufacturing processes.

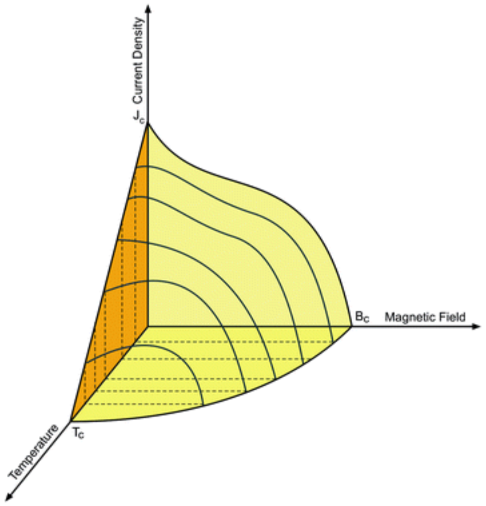

Figure 1.2.4: *Example of a critical surface of a generic superconducting material, taken from* [2].

The temperature, magnetic field, and current density are the main parameters defining when a superconductor is indeed superconducting but are not the only ones. The frequency plays a crucial role, in the behavior of a superconductor, a superconductor is only free of losses only when the frequency is null. The critical current density can be expressed as a function of the frequency [27]. Another parameter that defines the superconducting state is the strain, which represents the mechanical elongation per unit length of the material along a particular direction due to applied stresses. Strain significantly impacts the critical current density of a superconductor [28, 29].

1.3 The superconducting materials

Ever since their discovery in 1911, superconducting materials have captivated the scientific community with the immense potential they embody. Over the years, a plethora of new superconductors have emerged, encompassing fundamental elements, composite alloys, and ceramic materials. Based on their properties and behavior, superconductors can be classified into various categories.

1.3.1 Magnetic classification: Type I and Type II superconductors

It is possible to classify the superconducting materials from an electromagnetic point of view. Their response to an applied magnetic field is what determines if a superconductor is of Type I or Type II.

Type I superconductors exhibit a distinct magnetic behavior, conforming to the principles outlined in Section 1.2.2. Specifically, when subjected to an external magnetic field exceeding its critical value (B_c), the superconducting state of the material abruptly ceases to exist, and its inherent properties vanish. Since B_c typically ranges in the order of a few tens of milliteslas (mT), the practical applications of Type I superconductors are severely limited, particularly in scenarios involving strong magnetic fields, such as electromagnets. This type of superconductor was the first to be discovered, and it encompasses numerous elements (as illustrated in Fig. 1.3.1) and a few metal alloys.

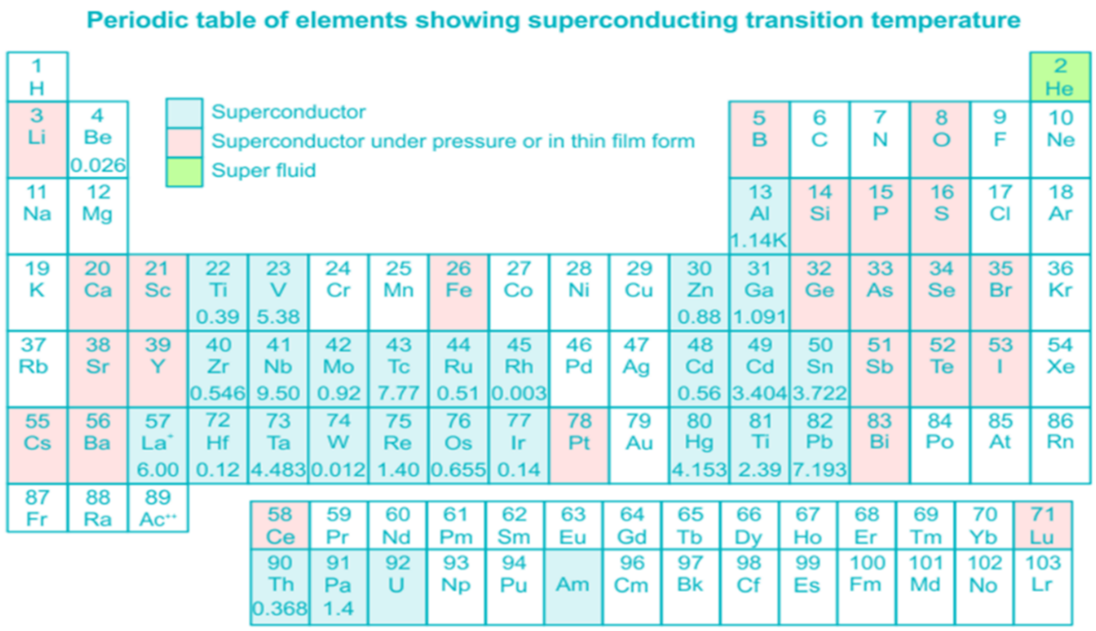

Periodic table of elements showing superconducting transition temperature

🟦 Superconductor
🟥 Superconductor under pressure or in thin film form
🟩 Super fluid

1 H																	2 He
3 Li	4 Be 0.026											5 B	6 C	7 N	8 O	9 F	10 Ne
11 Na	12 Mg											13 Al 1.14K	14 Si	15 P	16 S	17 Cl	18 Ar
19 K	20 Ca	21 Sc	22 Ti 0.39	23 V 5.38	24 Cr	25 Mn	26 Fe	27 Co	28 Ni	29 Cu	30 Zn 0.88	31 Ga 1.091	32 Ge	33 As	34 Se	35 Br	36 Kr
37 Rb	38 Sr	39 Y	40 Zr 0.546	41 Nb 9.50	42 Mo 0.92	43 Tc 7.77	44 Ru 0.51	45 Rh 0.003	46 Pd	47 Ag	48 Cd 0.56	49 Cd 3.404	50 Sn 3.722	51 Sb	52 Te	53 I	54 Xe
55 Cs	56 Ba	57 La* 6.00	72 Hf 0.12	73 Ta 4.483	74 W 0.012	75 Re 1.40	76 Os 0.655	77 Ir 0.14	78 Pt	79 Au	80 Hg 4.153	81 Ti 2.39	82 Pb 7.193	83 Bi	84 Po	85 At	86 Rn
87 Fr	88 Ra	89 Ac**															
				58 Ce	59 Pr	60 Nd	61 Pm	62 Sm	63 Eu	64 Gd	65 Tb	66 Dy	67 Ho	68 Er	69 Tm	70 Yb	71 Lu
				90 Th 0.368	91 Pa 1.4	92 U	93 Np	94 Pu	Am	96 Cm	97 Bk	98 Cf	99 Es	100 Fm	101 Md	102 No	103 Lr

Figure 1.3.1: *Periodic table of elements with a focus on those capable of showing superconducting properties. As shown, some of the elements are superconductors only in particular conditions such as high pressure or laminated into thin film. This is an important statement that reinforces the idea that superconductivity is not an intrinsic property of the materials.*

In 1935, L. Shubnikov and J. N. Rjabinin experimentally discovered a new class of superconductors with distinct magnetic properties, differentiating them from conventional superconductors [30]. Several years later, theoretical explanations for these observations were proposed by V. L. Ginzburg and L. D. Landau [31], later refined by A. A. Abrikosov [32]. These materials, categorized as Type II superconductors, exhibit a unique "double transition" characterized by two distinct magnetic field thresholds (B_{c1},B_{c2}). Within the lower critical magnetic field range, B_{c1}, their behavior mirrors that of Type I superconductors. However, upon exceeding this remarkably low threshold, Type II superconductors do not abruptly transition to a normal state but instead enter a mixed state where the superconducting and normal states coexist. In this phase, the material's perfect diamagnetism is compromised, and magnetic field vortices, also known as fluxons (quantum of magnetic field), begin to penetrate the material. The quantum of the magnetic field is often represented as Φ_0, its value amount to $\frac{h}{2e}$, where h is the Plack constant and e is the charge of the electron. These vortices form closed regions that experience a transition to the normal state, while the surrounding areas retain their superconductivity. The mixed state with the penetration in the superconductor of fluxons is depicted in Fig. 1.3.2.

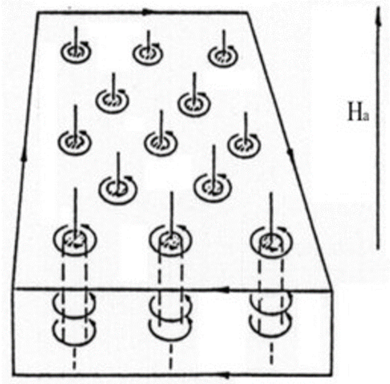

Figure 1.3.2: *Graphic representation of the mixed state of a Type II superconductor.*

From a macroscopic point of view, the material maintains its superconducting behavior due to the limited size of the fluxons. The fluxon density increases as the field strength rises. This mixed state persists until the upper critical magnetic field, B_{c2}, is reached. Beyond this threshold, the material becomes fully penetrated by fluxons, losing its superconductive properties. As a consequence, Type II superconductors offer significantly enhanced operating conditions compared to Type I materials, as their B_{c2} limit is considerably higher. In certain alloys, the upper critical field can exceed the amplitudes of several Teslas (depending on the temperature), making them suitable for magnetic applications. This explains why almost all modern superconducting materials belong to Type II. For a better understanding, Fig 1.3.3 illustrates the contrasting magnetic behaviors of Type I and Type II superconductors.

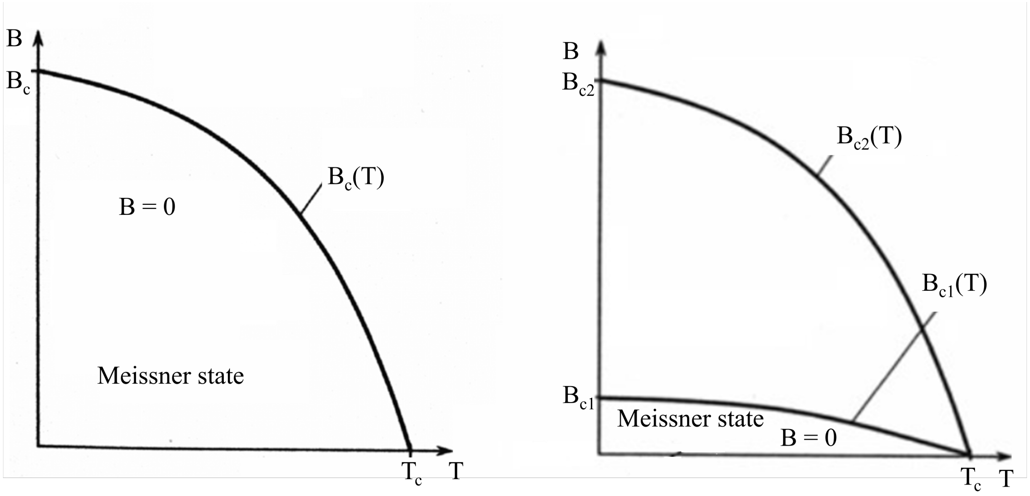

Figure 1.3.3: *On the left the magnetic behavior of a Type I superconductor, on the right a Type II superconductor. The two graph are not in scale,* $B_{c1} << B_c << B_{c2}$.

1.3.2 Temperature classification: Low temperature vs High temperature superconductors

While the classification of superconductors into Type I and Type II is primarily based on their magnetic behavior, an additional classification scheme can be employed based on their critical temperature. The primary concern regarding the practical implementation of superconducting materials in engineering applications is the ability of the superconductor to function within operating conditions without exceeding the critical surface, thereby preserving its worthwhile properties. The most expensive requirement for a superconducting device to be able to work is maintaining the cryogenic temperature. The requirement for operation at low temperatures significantly raises the expense of superconducting technology. As a result, enhancing the T_c of superconductors would not only broaden their applicability but also make them more cost-efficient. In this respect, great progress has been made over the years as shown in Fig. 1.3.4.

The classification of superconductors based on their critical temperatures yields what are commonly referred to as low-temperature superconductors (LTS) and high-temperature superconductors (HTS).

Low-temperature superconductors (LTS) exhibit a critical temperature of a few degrees above absolute zero, necessitating cooling with liquid helium (primarily) or hydrogen, both of which are expensive and require specialized handling. Despite these limitations, the LTS were the first type of superconductor discovered

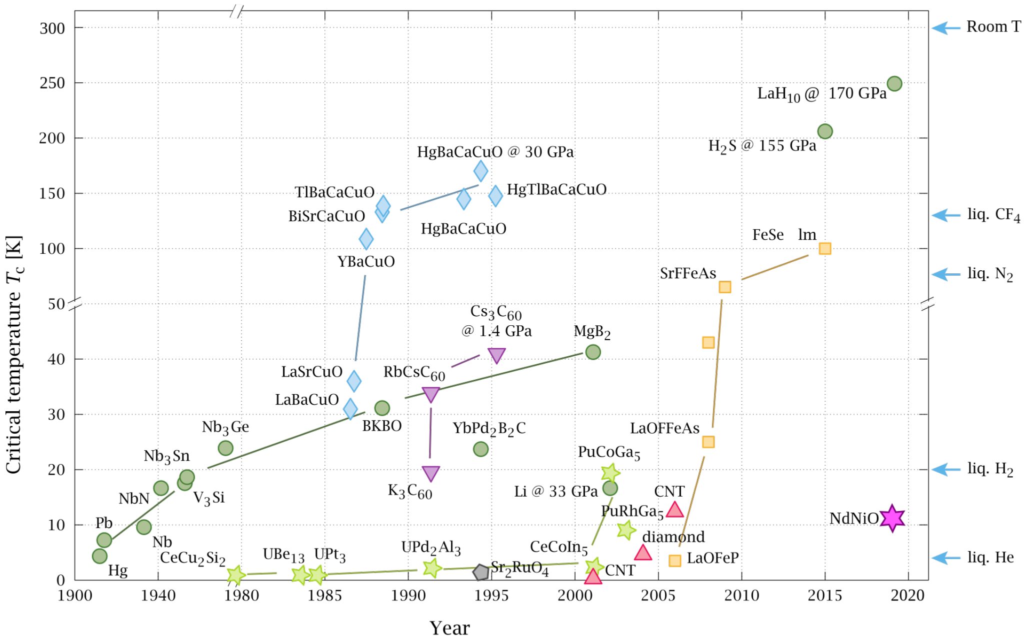

Figure 1.3.4: *Timeline of the critical temperature of superconductors from 1911 to 2020* [3]. *On the right one can see the liquid nitrogen temperature, which usually divides superconductors at high from superconductors at low temperatures. Cuprates are displayed as blue diamonds and iron-based superconductors as yellow squares. Magnesium diboride and other low-temperature or high-pressure metallic BCS superconductors are displayed for reference as green circles.*

and commercialized; their unitary cost is now comparable to that of traditional conductors like copper [33]. Their electromagnetic properties have also undergone significant advancements over the years, making them the primary superconductors employed in biomedical applications [34] and large-scale particle physics devices [35]. Most LTS are based on niobium alloys, particularly NbTi and Nb3Sn. These alloys are fabricated into flexible multifilament cables (e.g., Rutherford cables and Cable-in-Conduit conductors) capable of carrying massive currents. $NbTi$ is preferred due to its ductility, which simplifies and reduces the cost of its fabrication using the powder-in-tube technique [34]. Nb_3Sn, on the other hand, offers superior performance (B_{c2} exceeding 20 T at 4.2 K, while B_{c2} is approximately 12 for $NbTi$ at the same temperature), but its fabrication is more expensive due to its brittleness and the requirement for thermal treatment after the winding into its final configuration, using the so-called wind-and-react techniques.

A groundbreaking breakthrough in the field of superconductivity occurred in 1986 when G. Bednorz and A. Müller successfully transitioned a new class of ceramic materials (known as cuprates) into the superconducting state at a temperature surpassing 30 K, which significantly exceeded the critical temperatures of LTS materials and defied the prevailing theories at the time [36]. This T_c value, conventionally established as the threshold distinguishing HTS from LTS, paved the way for further research into numerous materials, leading to the development of HTS with critical temperatures exceeding 77 K. This development holds immense significance as it enables the utilization of liquid nitrogen as a coolant, a cryogenic fluid less expensive and more readily available compared to liquid helium. To date, the most extensively studied and commercially produced HTS materials belong to two categories: Bismuth-Strontium-Calcium-Copper-Oxides (abbreviated as BSCCO, also known as first-generation HTS) and Rare Earth-Barium-Copper-Oxides (abbreviated as (RE)BCO, also known as second-generation HTS). This thesis work will be focused on the application of HTS materials of the REBCO family so discussions about the characteristics of BSCCO HTS are omitted. The HTS not only can work at a much higher temperature than the LTS but also possesses greater J_c and B_c, meaning that they can work in a much broader space of operating conditions. A comparison of the critical surface of an HTS material and an LTS one is shown in Fig 1.3.5.

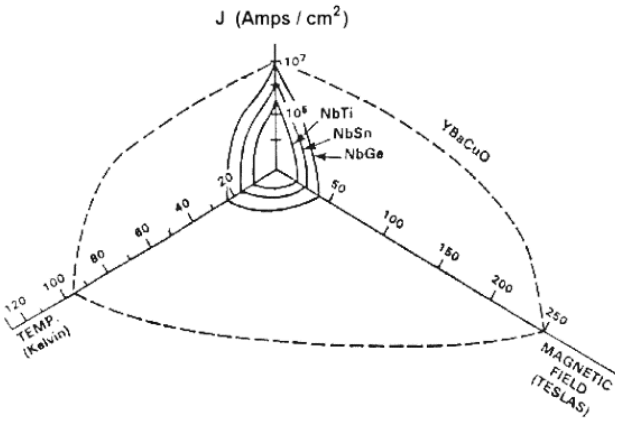

Figure 1.3.5: *Critical surface comparison between HTS (YBCO) and several LTS (Nb based).*

REBCO represents a family of ceramic compounds, where the Rare Earth elements can be Yttrium, Samarium, Neodymium, or Gadolinium. REBCOs stand as the only superconductors capable of operating within a medium-to-high magnetic field range (7–10 T) at temperatures exceeding 77 K. Furthermore, they exhibit reduced anisotropy with respect to the magnetic field compared to BSCCO compounds. Therefore, they are considered promising candidates for the development of future high-field magnets on a large scale.

Second-generation HTS are manufactured as tapes comprising various materials, in which the superconducting compound constitutes a relatively small portion of the conductor. The different materials are arranged in stacked layers, and for this reason, they are often referred to as coated conductors. The REBCO layer undergoes biaxial texturing during the manufacturing process to achieve an optimal arrangement of its grains and ensure optimal performance. Achieving sufficiently long tapes (several hundred meters) with homogeneous properties along their length demands slow and expensive processes, which currently represent a bottleneck for this technology. This is crucial to prevent weak points in a superconducting device, which can compromise overall performance, as in the case of a coil.

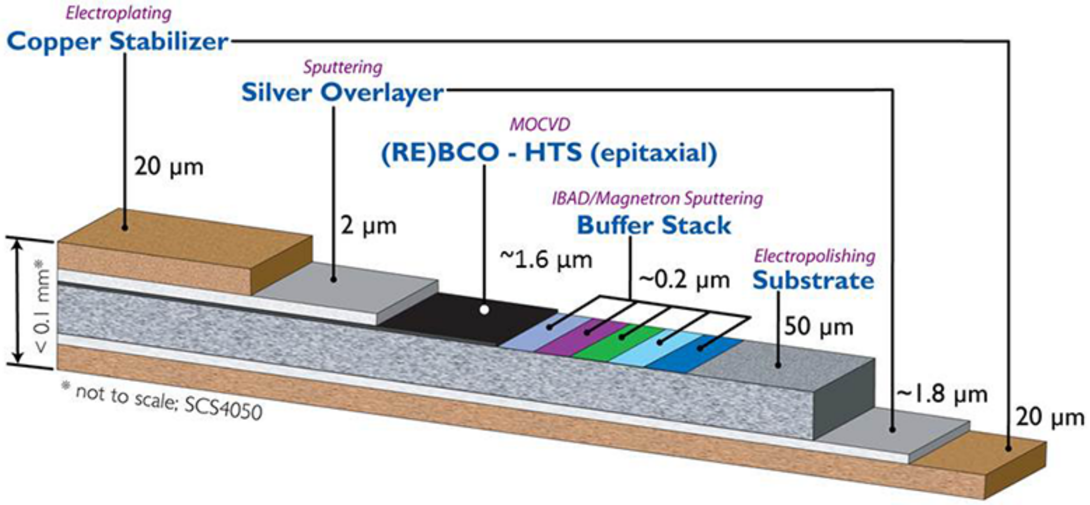

Figure 1.3.6: *Example of a second generation REBCO tape, manufactured by Superpower inc., with all of the thickness of all the components illustrated. As stated before the superconductor is only a small fraction of the tape. The substrate is there for mechanical reasons, while the silver layer is a chemical stabilizer, barring oxygen from disrupting the superconductor chemical structure* [4].

Fig. 1.3.6 provides an example of the structure of a second-generation HTS tape: the metallic substrate ensures the flexibility of the conductor, the thin layers beneath the superconductor are designated as buffer layers and they guarantee the proper "growth" of the superconducting layer by organizing the structure of the grains deposited, while the metallic layers are inserted as electrical and thermal stabilizers. The cross-section of HTS tapes exhibits an unusual aspect ratio: it is a few tens of microns thick and a few centimeters wide.

1.3.3 Thermal stability

Superconducting devices and individual tapes are susceptible to a range of heat sources during operation. These sources can be external, dictated by the specific application (e.g., particle showers in accelerator magnets or leaks/cracks in cryogenic vessels), or internal. Internal heat sources originate from ohmic losses, coupling losses, flux creep and flux flow mechanisms [37], and particularly, AC losses [38], which are meticulously addressed in this work.

Upon cooling and connecting a superconductor to a power supply, the cryogenic system is tasked with effectively removing all heat introduced into the system, maintaining the operating temperature at its designed value. This mandates meticulous design of the refrigeration system and an accurate estimation of the heat input from each source. Failure to achieve this balance or an unforeseen disturbance of sufficient duration and intensity can induce a localized temperature rise within the superconducting material. This in turn is equivalent to a localized reduction of the critical current of the tape and can trigger a transition to the resistive state, resulting in additional power dissipation due to Joule heating. If the refrigeration system cannot remove this additional heat, the heat generation can propagate to neighboring regions, causing the entire material to transition to the resistive state. This irreversible transition is termed a quench, an undesirable phenomenon for most applications. In contrast, if the equilibrium between heat input and heat removal is maintained through diverse cooling mechanisms, the resistive region can contract, a phenomenon known as recovery.

Quench protection systems are incorporated into nearly all devices, either active (utilizing mechanical or superconducting switches) or passive (embedded into the device design and not manually activated). Active quench protection systems necessitate quench detection, which is more intricate in HTS compared to LTS due to the lower Normal Zone Propagation Velocity (NZPV) in the former (ranging from 2-10 cm/s for HTS [39] vs. up to 7.5 km/s for LTS [40]). The slower NZPV in HTS favors the formation of hot spots, demanding finer control over the device. An instance of a passive protection system involves coupling superconducting materials with conventional conductors during tape fabrication. This passive protection method is visible in Fig. 1.3.6, where the copper layers are posed there exactly for this reason in order to guarantee a certain degree of thermal stability.

Incorporating one or more metals that exhibit significantly lower resistivity than the superconductor in its normal state, enhances the thermo-electrical stability of the tape or cable by promoting current-sharing behavior. Fig. 1.3.7 depicts an equivalent electrical circuit of the HTS tape previously shown, illustrating the sequential events that occur when the superconductor's temperature rises due to internal or external heat sources that exceed the cryogenic system's cooling capacity. As long as the temperature remains below a critical threshold value, the current sharing temperature (T_{cs}), the superconductor maintains a low resistance, and the entire operating current flows through the superconducting layer of the tape. This current-sharing temperature, is a function of the conductor configuration, encompassing the properties of the superconductor and the adjacent metallic layers. When the temperature surpasses T_{cs} but has not yet reached the critical value, T_c, the superconductor's resistance begins to approach that of the parallel-connected metal. As a result, a portion of the operating current is transferred to the metal, mitigating the excessive heat generation in the superconductor due to Joule heating. If the temperature exceeds T_c, the superconductor transitions fully to the resistive state, and its resistance exceeds that of the parallel metal. If the current is not promptly interrupted, a substantial amount of heat will be generated in the superconducting layer, potentially leading to permanent damage. In this scenario, the operating current completely shifts to the metallic layers, thereby protecting the superconductor.

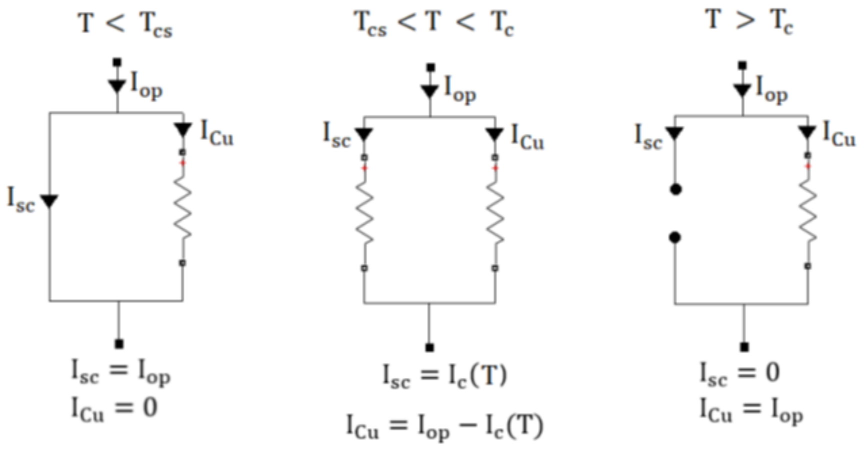

Figure 1.3.7: *Simplified circuit model of the current sharing phenomenon.* I_{sc} *is the current in the superconducting layer* I_{cu} *is the current in the copper layer.*

This state can persist for a brief period, as the cross-sectional area of the metallic layers is insufficient to handle the full operating current. If the current is not terminated expeditiously, these layers will also heat up and risk melting. Furthermore, the high thermal conductivity of the parallel metals facilitates the redistribution of heat along the conductor, reducing the likelihood of hot-spot formation and enhancing quench detection.

1.4 HTS application

This thesis is primarily concerned with the investigation of second-generation HTS. The primary applications examined in this work are cables for fusion applications and non-insulated coils. It is also important to note that these are only two of the many potential applications for these innovative materials, which, despite their relative novelty and complexity, have already begun to find use in a variety of applications or are being investigated to study their implementation. Some of the applications of second-generation HTS are briefly reported here for informational purposes: power cables [41–43], high field magnets [44–47], SMES [48,49] systems, NMR spectrometers [50, 51] and MRI magnets [52, 53], wind generators [54, 55], SFCL [56–58].

1.4.1 Review of HTS Cable Concepts for Fusion Applications

In this section, we intend to make a brief review of the different types/layouts of HTS cables developed in recent years, and of particular relevance for fusion applications. Regarding the development of fusion cables, the literature is growing and enriched every day with new and interesting designs. Several conductor layout and/or cabling methods have been proposed and investigated. Selected conceptual design are here reported: the Roebel Assembled Coated Conductor (RACC) cable [5]; the Twisted Stacked Tape Cable (TSTC) [6, 59] the Round Soldered and Twisted Stacked strand (RSTS) [7,60,61]; The Cross-Conductor (CroCo) [8]; the Stacked Tapes Assembled in Rigid Structure (STARS) [9]; the Quasi Isotropic strand (Q-IS) [10]; the Conductor On Round Core (CORC) [11]; and the Slotted Core TSTC cable (SC-TSTC) [62,63].

- **Roebel Assembled Coated Conductor (RACC) cable**: In Fig. 1.4.1, the Roebel concept for a high current (kA-class) low AC loss cable is shown. RACC is a suitable assembling technique for conductors in magnet windings due to the flat rectangular cross-section. The RACC employs pre-shaped tapes into strands with the Roebel-specific meander geometry. The usually very good bending properties of HTS coated conductors support the assembling procedure of the RACC-cable.

- **Twisted Stacked Tape Cable (TSTC)**: In the TSTC concept, the tapes are simply stacked and twisted in order to increase the current capabilities minimizing the AC losses. Freestanding flat tapes are torsionally twisted

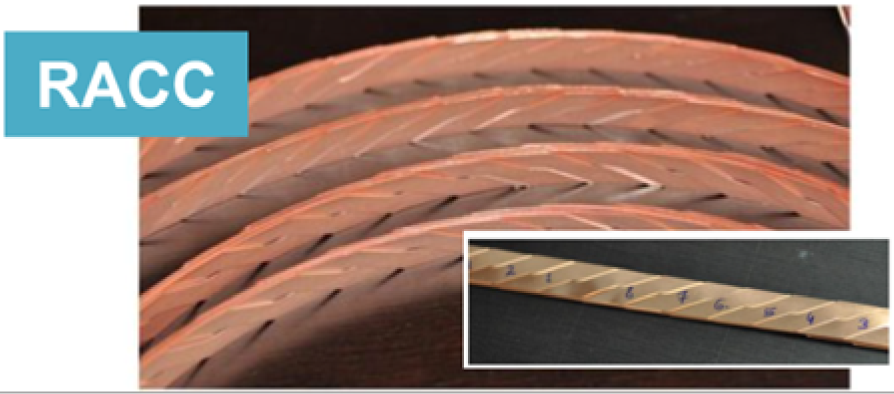

Figure 1.4.1: *The Roeble Assembled Coated Conductor (RACC) cable based on Roebel idea, reproduced from* [5].

along the axis of the stack without an external tensile or compressive longitudinal force, as shown in Fig. 1.4.2. The method allows the development of high current, compact conductors for various applications such as power transmission cables and high field magnets. The twisted stacked-tape cable may be enclosed by an electrically conducting conduit as a stabilizer and supporting structure. There are a few options to make the twisted stacked-tape conductor: 1) Stack and twist, then clad, 2) Stack and clad, then twist, or 3) Stack, and then embed in helical open grooves on a structured conduit. Multi-stage cabling of this basic conductor allows the development of high current conductors such as a cable-in-conduit conductor.

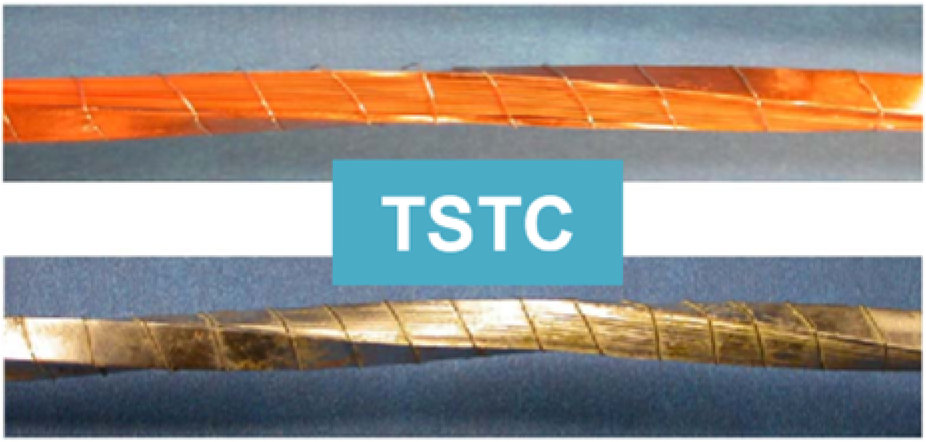

Figure 1.4.2: *The Twisted and Stacked Tape Cable (TSTC), reproduced from* [6].

- **Round Soldered and Twisted Stacked (RSTS) strand**: This concept, illustrated in Fig. 1.4.3, features a stack of soldered tapes enclosed between two copper profiles, forming a round strand. Several of these strands can be twisted together to reach high current capability. The main motivation for twisting at strand and cable level is to obtain a full transposition of the tapes, while the reduction of AC losses is a minor requirement.

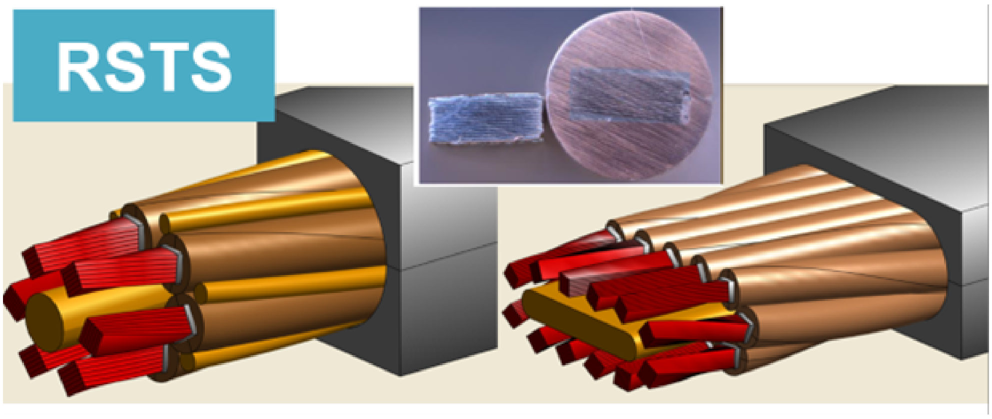

Figure 1.4.3: *The Round Soldered and Twisted Stacked (RSTS), reproduced from* [7].

- **Cross-Conductor (CroCo)**: The Cross-Conductor (CroCo) is the HTS design proposed by KIT. This concept is a modified type of TSTC, in which tapes of different widths are employed in order to optimize the current that can be transported in the same space. The CroCo layout also eases long-length fabrication. This cable design is illustrated in Fig. 1.4.4

Figure 1.4.4: *The Cross-Conductor (CroCo) concept, reproduced from* [8].

- **Stacked Tapes Assembled in Rigid Structure (STARS)**: The large-current capacity HTS conductor shown in Fig. 1.4.5, referred to as STARS, is being developed by the incorporation of several innovative ideas, such as the simple stacking of state-of-the-art REBCO coated conductors embedded in a copper jacket, surrounded by electrical insulation inside a conductor, and an outer stainless-steel jacket cooled by helium gas. This untwisted configuration has the advantage of being simple to assemble and manufacture. The formation of a non-uniform current distribution among the HTS tapes in STARS cables could be accepted because of the high thermal stability.

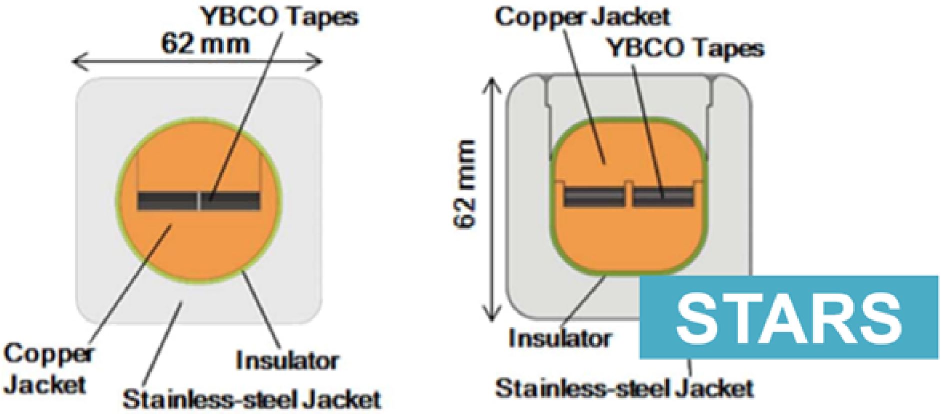

Figure 1.4.5: *The Stacked-Tapes Assembled in Rigid Structure (STARS), reproduced from* [9].

- **Quasi-Isotropic (Q-IS) strand**Another interesting configuration is the Quasi Isotropic strand (Q-IS) shown in Fig. 1.4.6: the idea, in this case, is to compose a strand stacking the HTS tapes horizontally and vertically. To improve the thermal and mechanical properties, the superconducting core is wrapped with aluminum foil about 1 mm thick and copper as the sheath. A cabling method by mature technology of laser welding employed in optical fiber power cable was used in the fabrication of practical long Q-IS. Under a DC magnetic field of 0.1 T and 0.5 T, the maximum anisotropic values of normalized critical current are only 1.73% and approximately 8%, respectively, which indicates that the critical current of Q-IS has good enough isotropy at least at lower magnetic field.

- **Conductor On Round Core (CORC)** In this cable layout, the HTS tapes are wrapped on top of a round metallic core. This concept aims at reaching tens of kA in >10 T magnetic field, which is a typical requirement in fusion magnets. An interesting configuration is the CORC six-around-one Cable-In-Conduit Conductors shown in Fig 1.4.7. This configuration comprises a cable of six CORC strands helically wound around a rod or

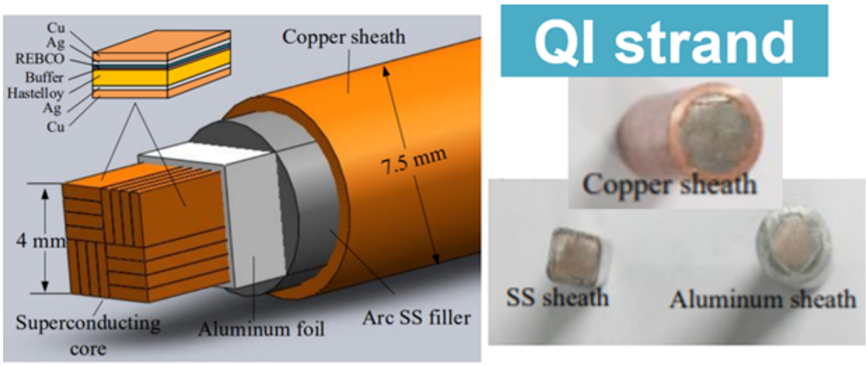

Figure 1.4.6: *The Quasi-Isotropic Strand (Q-IS), reproduced from* [10].

hollow tube. The CORC strands are relatively flexible and allow straight forward twisting around the central core. The cable is inserted into a square, round, or rectangular jacket. The jacket is ideally made of aluminum alloy, which is mechanically strong while maintaining good electrical and thermal properties. Internal forced flow gas cooling can be established via parallel flow in a perforated tube and the voids between strands.

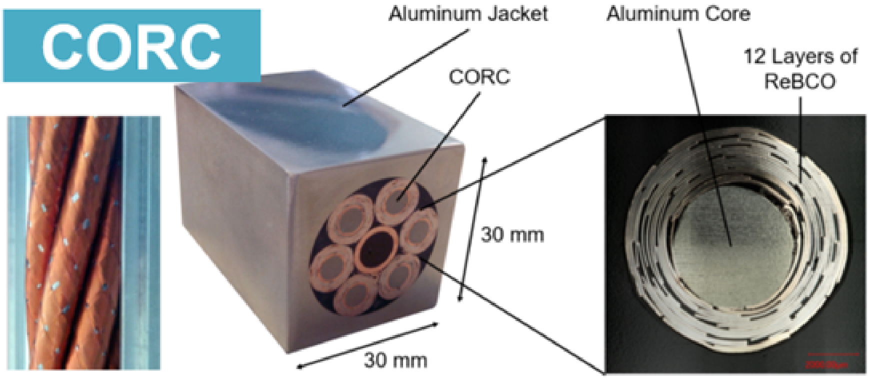

Figure 1.4.7: *The Conductor-On-Round-Core (CORC), reproduced from* [11].

- **Slotted Core TSTC (SC-TSTC)**: The ENEA SC-TSTS CICC consists of an aluminum core with several helical slots. Each slot contains a stack of REBCO tapes, as depicted in Fig. 1.4.8 in the 6-slot version. At the top of each stack, spacers are placed to ensure uniform compaction. To protect the assembly from any damage occurring during drawing compaction and jacketing processes, a stainless steel tape is wrapped around the cable. Each slot has a square cross-section designed to accommodate 20–30 tapes depending on their thickness. The central channel provides a path for the forced flow of supercritical Helium, such as to ensure optimal cooling of the cable. Optionally, to enhance the cooling of the superconducting stacks, it is possible to make use of secondary paths for the coolant, like the lateral gaps and semi-circular grooves at the bottom of the stack. The conductor in Fig. 1.4.8 is targeted for a current of 25–35 kA at 4.2 K and 12–18 T, with the current carrying capabilities determined largely by the choice of the coated conductor tape and on the number of slots (5 or 6).

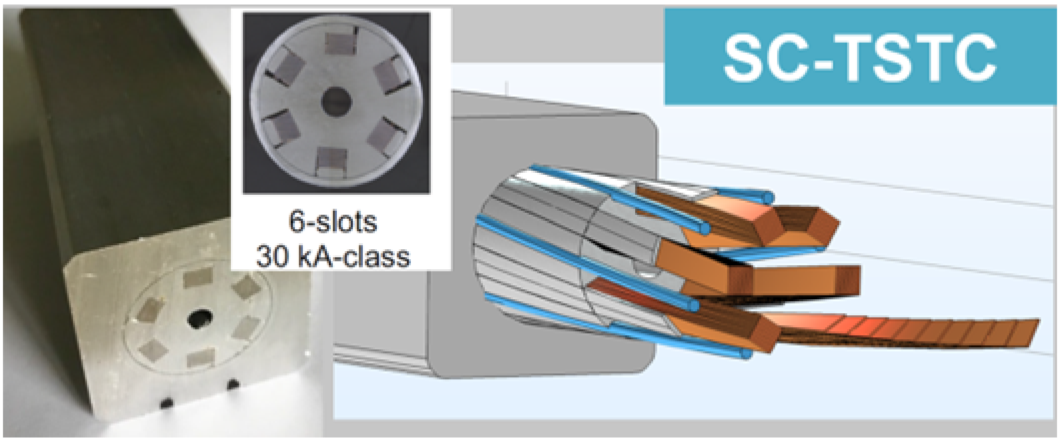

Figure 1.4.8: *The Slotted-Core Twisted-Stacked Tape Conductor (SC-TSTC).*

We end this section by stressing the fact that most of the proposed cables make use of HTS tapes arranged in stacked configurations. The most promising candidates for fusion applications seem to be those cables based on the TSTC concept: a few tens of tapes are stacked together and enclosed in a copper round profile, to emulate a round strand, or putting them on a core, obtaining a cable.

In this thesis, the focus is on investigating AC losses in TSTS, particularly for the SC-TSTC configuration.

1.4.2 Non insulated HTS coils

As discussed in Section 1.3.3, quenches pose a significant challenge to the operation of superconducting devices, particularly for HTS coils. Protection and refrigeration systems are often over-engineered to address this issue, and the current flowing through the windings is kept below the critical current. However, in conventional coils where the turns are electrically insulated from each other, the risk of local hot spot formation remains a concern. This is because the only alternative path for the current is through the metal layers of the tape, which can only handle limited current levels (current-sharing phenomenon). Therefore, prompt detection of local quenches and rapid dissipation of stored energy through active and/or passive protection systems are crucial.

A potential solution to quench protection challenges lies in utilizing non-insulated (NI) coils, wound without electrical insulation between turns [64]. In these windings, the current can also flow in the radial direction (jumping from one turn to the adjacent one), effectively bypassing damaged or quenched areas, thus enhancing overall thermal stability [12, 65–67]. Fig. 1.4.9 depicts a conceptual representation of this defect-irrelevant behavior [12]. These coils are often referred to as self-protecting, indicating their ability to fully recover from quenches without the need for external protection mechanisms to dissipate stored energy [68]. The current redistribution promotes heat diffusion over larger areas (easier to detect), which can involve the entire coil, leading to gradual and global quench propagation thus mitigating the formation of hot spots that would otherwise burn the tape. As a result, the current supply can be more easily interrupted and resumed. Consequently, an NI coil can be wound using tape with a minimal number of stabilizer layers, increasing winding compactness and significantly reducing the amount of tape required compared to its insulated counterpart to achieve the desired magnetic field [69].

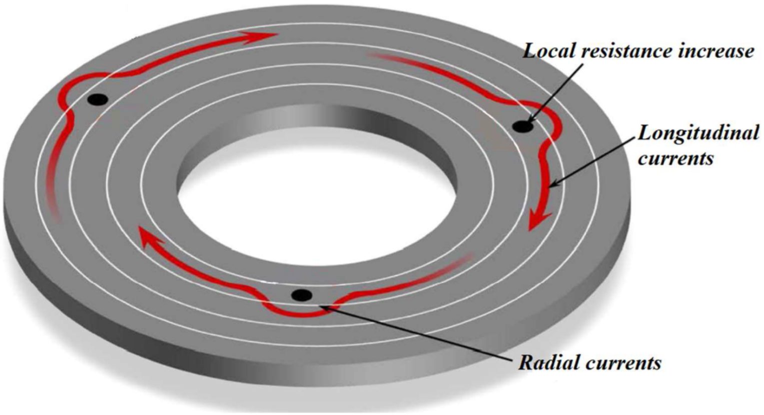

Figure 1.4.9: *Artistic representation of the radial flow of electric current in a NI coil with local high-resistive* sections [12].

The NI-HTS coils can typically be fabricated using either the pancake-wound technique [70–73] or the layer-wound technique [74–79], each resulting in distinct current distributions. In NI pancake coils, the turns are in close radial contact with adjacent layers that are positioned relatively close along the tape length. In NI layer-wound coils, on the other hand, a turn may be in contact with adjacent turns that are significantly spaced apart along the tape length, depending on their location within the layers. As a result, the two configurations must be analyzed independently. This work will provide in the following sections a circuit model for layer wound coils, that can also be employed for other configurations.

2 *AC losses in HTS conductors*

In the design of superconducting magnets, it is often necessary to estimate the electromagnetic losses that result from a change of the external magnetic field and/or the conductor transport current, these losses will be referred to as AC losses. For large-scale magnets especially, a quantitative analysis of the losses becomes quite important in order to determine the thermal budget. In many applications, such as a Tokamak device, the field coils are subjected to time-varying fields and currents, and because of this, power is dissipated by the coils. More in detail, the AC loss is generally subdivided into three contributions, namely the hysteretic loss, originating from the shielding currents, the coupling loss, due to the coupling currents, and the dynamic resistance loss, which is related to the work done by the transport current power supply. The AC loss load, as a function of time, is used as an input for transient thermo-hydraulic (TH) analyses. To date, no tools have been proven reliable for evaluating AC losses in a large-scale high-temperature superconductor (HTS) magnet [80]. Detailed models have been developed for single HTS tapes, stacked tapes, or HTS coils with a diameter of a few cm. The strategy for developing a reliable thermo-hydraulics model of an HTS magnet could be either to apply the tools developed for LTS magnets also for HTS magnets or to upscale the existing detailed models developed for small-scale HTS applications.

This chapter will address the most commonly known numerical and analytical formulation for the evaluation of AC losses in HTS conductors.

2.1 Constititive law of superconductor

2.1.1 Power law

Since the discovery of superconductivity, the scientific community developed several relations for the characterization of the electromagnetic behavior of superconducting materials. The most commonly adopted empirical fit is denominated the power law was first proposed in 1974 and its expression is reported in (2.1.1).

$$\mathbf{E} = E_c \left(\frac{J}{J_c}\right)^n \frac{\mathbf{J}}{|\mathbf{J}|} \tag{2.1.1}$$

where $\mathbf{J}$ is the current density, J_c is the critical current density of the tape, n is the n-value (also called n index or power factor) and E_c is the critical electric field. Conventionally, the critical electrical field is set equal to one of the following values: 10 $\mu V/m$ (lower critical field) or 100 $\mu V/m$ (upper critical field). In the following chapters of this work, the upper critical electric field is selected as the one to use.

From the power law is possible to derive an expression for the resistivity of the superconducting material:

$$\rho_{sc} = \frac{\mathbf{E}}{\mathbf{J}} = \frac{E_c}{J_c}\left(\frac{J}{J_c}\right)^{n-1} \tag{2.1.2}$$

Although the power law is widely used, the power law only well represents the macroscopic behavior of a superconductor for moderate values of current density/electric field. When $J > J_c$ the resistivity of the superconductor given by the power law grows exponentially instead of saturating to the value of the normal state resistance of the superconductor $\rho_n s$.It is easily possible to upgrade (2.1.2) to what is called the bounded power law:

$$\begin{cases} \mathbf{E} = \rho_{sc,bound}(J)\mathbf{J} \\ \rho_{sc,bound} = \frac{\rho_{ns}\rho_{sc}}{\rho_{ns}+\rho_{sc}} \end{cases} \tag{2.1.3}$$

The bounded power law represents the resistivity of a superconductor as a parallel combination of the resistivity of the superconductor in its normal state and its superconducting state.

2.1.2 Critical state model

Less precise than the power law but nonetheless very useful in many analytical formulations, is the critical state model. Many models of the critical state have been proposed in literature here only the bean model is presented in detail.

The Bean critical state model [81,82] describes macroscopically the magnetization of a type II superconductor when it is subjected to a time-varying magnetic field. At the heart of the Bean critical state model lies the concept of maximum current density, a critical value beyond which the superconducting state transitions to a resistive state. This maximum current density, denoted by J_c, represents the limit of superconductivity. Bean states that there is a maximum current density that can flow in a superconductor and that if an electric field, even a small one, is present, it induces the maximum current density. The equations of the Bean model are written in (2.1.4).

$$J(t) = \begin{cases} J_c & \text{if} \quad \exists \quad t' < t \quad | \quad E(t') > 0 \quad \& \quad E(t'') \geq 0 \quad \forall \quad t'' > t' \\ -J_c & \text{if} \quad \exists \quad t' < t \quad | \quad E(t') < 0 \quad \& \quad E(t'') \leq 0 \quad \forall \quad t'' > t' \\ 0 & \text{if} \quad E(t') = 0 \quad \forall \quad t' \leq t \end{cases} \tag{2.1.4}$$

In the Bean model, the critical current density is considered independent of the field which is equivalent to the assumption that the applied fields are much less than the critical fields. There exist several variations of the Bean model that take into account the dependence of the critical current from the magnetic field. These other models still abide by the other assumptions made by Bean and are therefore still called critical state models.

2.2 Main analytical formulae

The computation of losses during electrodynamic transients is of paramount importance for the dimensioning of the cryogenics system of HTS magnets. In general, the application of analytical formulae requires the adoption of numerous assumptions. In the literature, several formulae have been developed in order to calculate losses due to time-varying fields and/or transport currents applied to HTS conductors. The main assumption generally consists of a geometric simplification of the model. As a matter of fact, numerous formulae refer to the case of individual HTS tapes. As for the analyses of tape stacks or cables, several homogenization techniques are required to limit the computational burden. In this section, the main analytical models presented in the literature for the computation of losses in HTS tapes are briefly described. For each of them, the model's main hypotheses are reported along with the main equations for the AC loss computation. Furthermore, the homogenization techniques mentioned above are described, providing the reader with the corresponding analytical formulae.

2.2.1 Norris' formulae

These analytical formulae for loss computation are among the most widely used in the applied superconductivity community and were proposed by W. T. Norris for both a rectangular section thin strip and an elliptical cross-section tape [83]. These formulae are suited to compute the losses due to an alternate transport current flowing in the superconductor. Specifically, the formulae are used for the computation of the so-called surface Bean model losses. The following assumptions are adopted in the model:

- The geometry of the conductor is assumed as a thin strip, i.e. the tape is approximated as a 1D object with the main dimension along its width, neglecting its thickness and length (see next hypothesis).
- The conductor's length is assumed to be infinite.
- The tape's critical current density is independent of the external magnetic field (thus neglecting the field orientation and magnitude).

- The Critical State Model is adopted.

For superconducting wires carrying a transport current equal to their critical current, the losses per cycle per unit length, expressed as L, can be computed as:

$$L = \frac{1}{2}\left(\frac{\mu_0 I_c^2}{\pi}\right) \tag{2.2.1}$$

where I_c is the critical current of the tape. The formula can be generalized by introducing the dependence on the amplitude of the transport current. The general formula for a tape having a circular or elliptical cross-section is the following:

$$L = \frac{\mu_0 I_c^2}{\pi}\left[(1-F)\ln(1-F) + (2-F)\frac{F}{2}\right] \tag{2.2.2}$$

where the parameter F corresponds to the ratio between the amplitude of the transport current and the tape critical current $F = I_{op}/I_c$. For a tape having a rectangular cross-section (as the REBCO tapes), the losses per cycle per unit length can be expressed as

$$L = \frac{\mu_0 I_c^2}{\pi}\left[(1-F)\ln(1-F) + (1+F)\ln(1+F) - F^2\right] \tag{2.2.3}$$

2.2.2 Brandt's formulae

Brandt proposed a formulation to compute the hysteresis losses of a type II superconductor thin strip carrying a transport current and immersed in a perpendicular applied magnetic field, indicated here as H_a [84]. Like the Norris model, Brandt's formulation starts from the critical state model. However, Brandt's approach provides additional information, such as the current density and magnetic field distributions computed in analytical form. The formulae derived can be applied to superconducting tapes with a rectangular cross-section. The losses in the case of a perpendicular field [J/cycle/m] can be expressed as:

$$P = 4\mu_0 a^2 J_c^* H_a g \tag{2.2.4}$$

where

$$g = \frac{2H_c}{H_a} ln\left(cosh\left(\frac{H_a}{H_c}\right)\right) - tanh\left(\frac{H_a}{H_c}\right) \tag{2.2.5}$$

$$H_c = J_c^*/\pi \tag{2.2.6}$$

$$J_c^* = J_c d = \frac{I_c}{2a} \tag{2.2.7}$$

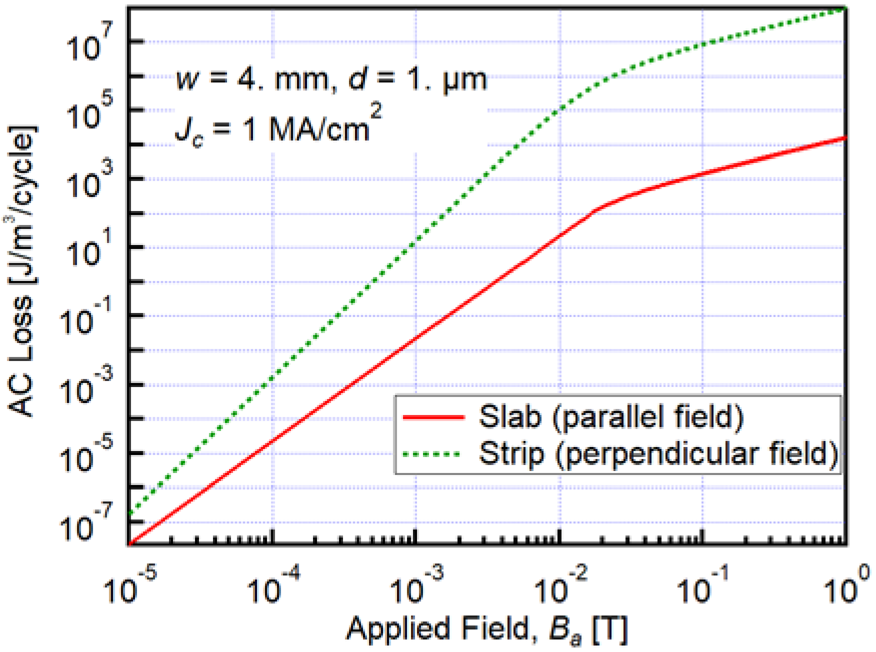

Figure 2.2.1: *Example of application of Brandt's formulae to the computation of losses due to a time-varying field applied to a 1 mm x 4 mm tape with* $I_c = 100$ *A.*

where a is the tape half-width, d is the superconductor thickness, and J_c^* is called the sheet current density. An analytic formula for the losses in a parallel field can also be retrieved through Brandt's model and is presented in equation (2.2.8). The losses are expressed as energy per cycle per unit volume [J/cycle/m3].

$$P = \begin{cases} \frac{2B_a^2}{\mu_0}\frac{\beta}{3} & \text{if} \quad \beta \leq 1 \\ \\ \frac{2B_a^2}{\mu_0}\left(\frac{1}{\beta} - \frac{2}{3\beta^2}\right) & \text{if} \quad \beta \geq 1 \end{cases} \tag{2.2.8}$$

Where:

$$B_a = H_a\mu_0, \quad \beta = \frac{B_a}{B_p}, \quad B_p = \mu_0 J_c d \tag{2.2.9}$$

An example of the application of Brandt's formulae to the calculation of losses due to a time-varying field applied to a 1 *mm* x 4 *mm* tape, considered as a slab (parallel field) or as a strip (perpendicular field) is reported in Fig. 2.2.1.

2.2.3 Müller's and Mawatari's formulae for infinitely stacked tapes

Both K. H. Müller and Y. Mawatari proposed a formulation for the computation of z-stacks and x-arrays of tapes made of metal–superconductor strips [13]. Thus, the tape is considered to be composed of a superconducting thin layer and a metallic substrate. Müller computes both the eddy current AC losses (power dissipated in the metal substrate) and the AC hysteresis losses (power dissipated in the superconductor itself). The losses for both eddy currents and hysteresis losses are computed in the case of self-field and for an AC magnetic field perpendicular to the tape.

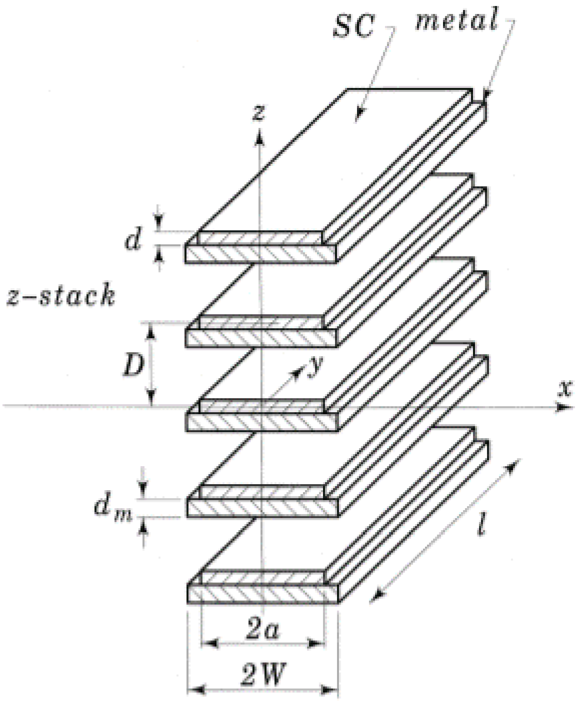

Figure 2.2.2: *Stack of infinitely long metal-superconductor strip along the z-axis used for the application of Müller's formula* [13].

The first configuration for which the formulae were developed is shown in Fig. 2.2.2. The subject of study is a z-stack of infinitely long ($l \to \infty$) metal-superconductor strips. An AC current ($I = I_m cos(\omega t)$ with $I_m < I_c$) is supplied to each metal–superconductor strip along the y-direction of the z-stack. The currents are in phase with each other. The frequency of the current (f $= \omega/2\pi$) is assumed as sufficiently low, so that the magnetic field generated by the eddy currents can be neglected compared to the magnetic field generated by the transport currents. For each tape, the eddy-current AC losses per unit length are given by:

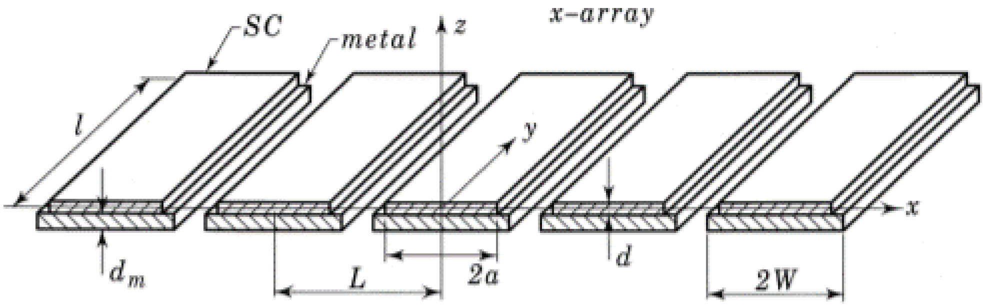

Figure 2.2.3: *Stack of infinitely long metal-superconductor strip along the x-axis used for the application of Muller's formula* [13].

$$P_{ed} = \frac{\mu_0^2}{2\pi^4}\frac{d_m}{\rho}a\omega^2 I_c^2 F \tag{2.2.10}$$

where the meaning of the geometric parameters a and D is illustrated in Fig. 2.2.2, while the function F is defined as follows:

$$F = \frac{D}{a}\left(\frac{I_m}{I_c}\right)^2 \int_0^{\pi} \sin^2(\phi) \left(\int_{\tilde{\eta}(\phi)}^{\pi w/D} acosh^2\left(\frac{sinh(\eta)}{sinh(\tilde{\eta})}\right) d\eta\right) d\phi \tag{2.2.11}$$

$$\tilde{\eta}(\phi) = arcoh\left(\frac{cosh(\pi a/D)}{cosh(\pi a I_m sin^2(\phi/2)/(DI_c))}\right) \tag{2.2.12}$$

The hysteresis losses per unit of length per strip, with a field independent J_c, can be computed as:

$$P_{hy} = \frac{\mu_0}{\pi^4} w I_c^2 \left(\frac{D}{a}\right)^2 \int_{\tilde{\eta}}^{\pi a/D} \left(\frac{a\pi}{D} - \eta\right) arctanh\left(\frac{tanh^2(\eta) - tanh^2(\tilde{\eta})}{tanh^2(\frac{a\pi}{D}) - tanh^2(\tilde{\eta})}\right)^{0.5} d\eta \tag{2.2.13}$$

$$\tilde{\eta} = arcoh\left(\frac{cosh(\pi a/D)}{cosh(\pi a I_m/(DI_c))}\right) \tag{2.2.14}$$

Now the formulae for the computation of the AC losses for a z-stack of tapes due to an AC external magnetic field will be discussed. The assumption for the computation of AC losses in a stack of tapes due to an external time-varying magnetic field is that the AC field ($H_a = H_m cos(\omega t)$) is applied in the z-direction, i.e. perpendicular to the broad face of the tapes. The magnetic field generated by the eddy currents is assumed to be negligible as compared to the sum of the external field and the self-field generated by the superconducting layers only. For each tape, the eddy-current AC losses per unit of length are given by:

$$P_{ed} = \frac{\mu_0^2}{3}\frac{d_m}{\rho}\omega^2 W^3 H_m^2 G \tag{2.2.15}$$

$$G = \left(\frac{D}{a}\right)^3 \left(\frac{W}{a}\right)^{-3} \frac{6}{\pi^4} \int_0^{\pi} \sin^2(\phi) \left(\int_{\tilde{\eta}(\phi)}^{\pi w/D} acosh^2 \left(\frac{cosh(\eta)}{cosh(\tilde{\eta})} \right) d\eta \right) d\phi \tag{2.2.16}$$

$$\tilde{\eta}(\phi) = arcsinh \left(\frac{sinh(\pi a/D)}{cosh(H_m sin^2(\phi/2)/(H_d))} \right) \tag{2.2.17}$$

$$H_d = J_c d/\pi \tag{2.2.18}$$

The term in (2.2.15) by which the function G is multiplied corresponds to the eddy current losses of an isolated metal strip having a width equal to 2W, thickness d_m, and resistivity rho exposed to a perpendicular AC magnetic field of frequency $\omega/2\pi$. The hysteresis losses per unit length per strip with a field independent J_c are given by the following expression [85]:

$$P_{hy} = \frac{2\mu_0}{\pi^2}\omega a^2 H_d^2 \int_0^{H_m/H_d} \left(\frac{H_m}{H_d} - 2\eta \right) ln \left(1 + \frac{sinh^2(a\pi/D)}{cosh^2(\eta)} \right) d\eta \tag{2.2.19}$$

A different configuration can also be considered, consisting of an infinitely long x-array (an infinite number of strips arranged as an array along the x-axis), as shown in Fig. 2.2.3. It is assumed that the strips are electrically insulated from each other. For each tape, the eddy-current AC losses per unit length can be computed as:

$$P_{ed} = \frac{\mu_0^2}{2\pi^4}\frac{d_m}{\rho}\omega^2 a I_c^2 M \tag{2.2.20}$$

Where

$$M = \left(\frac{I_m}{I_c}\right)^2 \left(\frac{L}{a}\right) \int_0^{\pi} \sin^2(\phi) \left(\int_{\tilde{\eta}(\phi)}^{\pi w/L} acosh^2 \left(\frac{sinh(\eta)}{sinh(\tilde{\eta})} \right) d\eta \right) d\phi \tag{2.2.21}$$

$$\tilde{\eta}(\phi) = arccos \left(\frac{cos(\pi a/L)}{cos(\pi a I_m sin^2(\phi/2)/(L I_c))} \right) \tag{2.2.22}$$

The hysteresis losses per unit length per strip with a field independent J_c are given by:

$$P_{hy} = \frac{\mu_0}{\pi^4}\omega I_c^2 \left(\frac{L}{a}\right)^2 \int_{\tilde{\eta}}^{\pi a/L} \left(\frac{a\pi}{L} - 2\eta\right) arctanh \left(\frac{tan^2(\eta) - tan^2(\tilde{\eta})}{tan^2(a\pi/L) - tan^2(\tilde{\eta})}\right)^{0.5} d\eta \tag{2.2.23}$$

Where the following quantity has to be defined:

$$\tilde{\eta} = arccos\left(\frac{cos(\pi a/L)}{cos(\pi a I_m/(L I_c))}\right) \tag{2.2.24}$$

Finally, the formulae for the AC losses for an x-array of tapes due to an AC external magnetic field are shown. For each tape, the eddy-current AC losses due to an external magnetic field applied to the tape array per unit length are provided by the following equation:

$$P_{ed} = \frac{\mu_0^2}{3}\frac{d_m}{\rho}\omega^2 W^3 H_m^2 N \tag{2.2.25}$$

where

$$N = \left(\frac{L}{a}\right)^3 \left(\frac{W}{a}\right)^{-3} \frac{6}{\pi^4} \int_0^{\pi} \sin^2(\phi) \left(\int_{\tilde{\eta}(\phi)}^{\pi w/L} acos^2\left(\frac{cos(\eta)}{cos(\tilde{\eta})}\right) d\eta\right) d\phi \tag{2.2.26}$$

$$\tilde{\eta}(\phi) = arcsin\left(\frac{sin(\pi a/L)}{cosh(H_m sin^2(\phi/2)/(H_d))}\right) \tag{2.2.27}$$

The hysteresis losses per unit length per strip with a field independent J_c [85] are equal to :

$$P_{hy} = -\frac{2\mu_0}{\pi^2}\omega a^2 H_d^2 \left(\frac{L}{a}\right)^2 \int_0^{H_m/H_d} \left(\frac{H_m}{H_d} - 2\eta\right) ln\left(1 + \frac{sin^2(a\pi/L)}{cosh^2(\eta)}\right) d\eta \tag{2.2.28}$$

Both in the case of AC current and for an external AC field, as long as the number of strips is large, the strips are sufficiently long and are supplied with an equal current (if this is accounted for), end-effects can be neglected and the AC losses of infinite arrays and stacks result similar to those of finite arrays and stacks. In contrast, in the self-field case where the strips of an array/stack of finite length are connected at both ends and a single current is supplied to this array/stack, the current does not distribute equally among the strips and the AC losses differ significantly from those computed using the formulae presented in this section.

2.2.4 Infinite slab formulae

The formulae for the losses per unit of volume and cycle ($[J/m^3/cycle]$) of an infinite slab, subjected to an external magnetic field, are well described in [86–88], are here reported in (2.2.29).

$$L = \begin{cases} \frac{2\mu_0 H_m^3}{3H_p} & \text{if} \quad |H_m| \leq |H_p| \\ 2\mu_0 H_p H_m (1 - \frac{2H_p}{3H_m}) & \text{if} \quad |H_m| > |H_p| \end{cases} \tag{2.2.29}$$

Where the parameters are defined as follows, $H_p = J_c a$, H_p is the penetration field expressed in $[A/m]$,a is the half-width of the slab, J_c is the critical current density of the slab. and H_m is the amplitude of the magnetic field.

2.2.5 Schomborg's formulae

Niclas Schonborg developed in his Ph.D. dissertation [89] numerous analytical formulae for the estimation of magnetization losses in various case studies. In [90] Schonborg presented a set of formulae for the magnetization losses, in case of AC transport current in phase with a magnetic field orthogonal to the wide surface of the tape, here reported in (2.2.30). Schonborg's formulae evaluate the losses in $[J/m/cycle]$ and were developed for a thin strip (1D geometry). these formulae are equivalent in the absence of an external magnetic field with Norris' formula (2.2.1). and in the absence of a transport current with Brandt's formula (2.2.2).

$$L = \frac{\mu_0 I_m^2}{\pi} \begin{cases} S_1 & \text{if} \quad \frac{I_m}{I_c} \leq \tanh\left(\frac{B_m}{B_f}\right) \\ S_2 & \text{if} \quad \frac{I_m}{I_c} > \tanh\left(\frac{B_m}{B_f}\right) \end{cases} \tag{2.2.30}$$

where

$$\begin{aligned} S_1 = 2\coth^{-1}\left(\frac{p_1 p_2 + a_0^2}{p_{1a} p_{2a}}\right) - \frac{1}{4}\left(p_2 p_{2a} + p_1 p_{1a}\right)\left(\cosh^{-1}\left(\frac{p_2}{a_0}\right) + \cosh^{-1}\left(\frac{p_1}{a_0}\right)\right) + \\ \frac{1}{2}\left(p_{2a} - p_{1a}\right)\left(p_2 \cosh^{-1}\left(\frac{p_2}{a_0}\right) + p_1 \cosh^{-1}\left(\frac{p_1}{a_0}\right)\right) + \\ \frac{1}{4}\left(p_{2a} - p_{1a}\right)^2 - \frac{1}{2}\left(p_{2a} - p_{1a}\right)\left(p_{1a} + p_{2a}\right) \end{aligned} \tag{2.2.31}$$

$$S_2 = -2\coth^{\text{-1}}\left(\frac{p_1p_2+a_0^2}{p_{1a}p_{2a}}\right) - \frac{1}{4}\left(p_2p_{2a}-p_1p_{1a}\right)\left(\cosh^{\text{-1}}\left(\frac{p_2}{a_0}\right)-\cosh^{\text{-1}}\left(\frac{p_1}{a_0}\right)\right)+ \frac{1}{2}\left(p_{2a}+p_{1a}\right)\left(p_2\cosh^{\text{-1}}\left(\frac{p_2}{a_0}\right)+p_1\cosh^{\text{-1}}\left(\frac{p_1}{a_0}\right)\right)-\frac{1}{4}\left(p_{2a}+p_{1a}\right)^2 \tag{2.2.32}$$

And the parameters used are

$$B_f = \frac{\mu_0 J_c}{\pi} \quad x = w\frac{\sqrt{1-\left(\frac{I_m}{I_c}\right)^2}}{\cosh\left(\frac{B_m}{B_f}\right)} \quad p = w\left(\frac{I_m}{I_c}\right)\tanh\left(\frac{B_m}{B_f}\right)$$

$$a_0 = \frac{x}{w} \quad p_0 = \frac{p}{w} \quad p_1 = (1-p_0) \quad p_2 = (1+p_0) \quad p_{1a} = \sqrt{p_1^2-a_0^2} \quad p_{1a} = \sqrt{p_2^2-a_0^2} \tag{2.2.33}$$

Equation (2.2.31) holds in the low-current high-field regime, while (2.2.32) holds in the high-current low-filed regime. The J_c used in the definition of the penetration field for the strip geometry B_f in (2.2.33) is the critical surface current density measured in $[A/m]$, it can be obtained from the critical current density used in the previous sections by dividing it for the thickness of the tape. The length of the wide surface of the tape (so the width) is the parameter w in (2.2.33). Comparison between (2.2.30), (2.2.2) and (2.2.6) is shown in Fig. 2.2.4, the data reported are for a REBCO tape which parameters are in Table 2.2.1.

Table 2.2.1: Tape Parameters

Tape thickness	150 μm	*Tape width*	4 mm
Superconductor thickness	1 μm	*critical current density (J_c)*	10^{10} A/m^2

As shown in Fig. 2.2.4 Schonborg's formulae perfectly overlap with Brand's one when the transport current is null. The results from (2.2.30) are missing for magnetic field above the value of $5B_f$ due to the hyperbolic functions in (2.2.30) diverging. In Fig. 2.2.5 it is possible to better appreciate the impact of the transport current in the AC losses, the penetration field B_f is equal to 4 mT with the data provided in table 2.2.1.

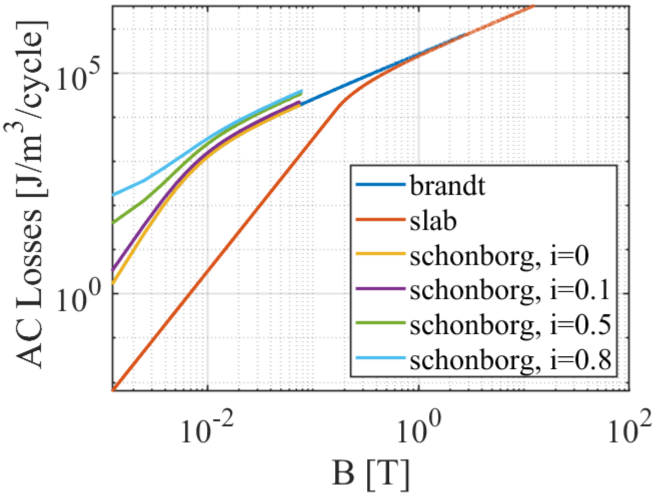

Figure 2.2.4: *Comparison between Brandt's formula, the slab formula, and Schonborg's formulae at different values of i, defined as the ratio between* I_m *and* I_c.

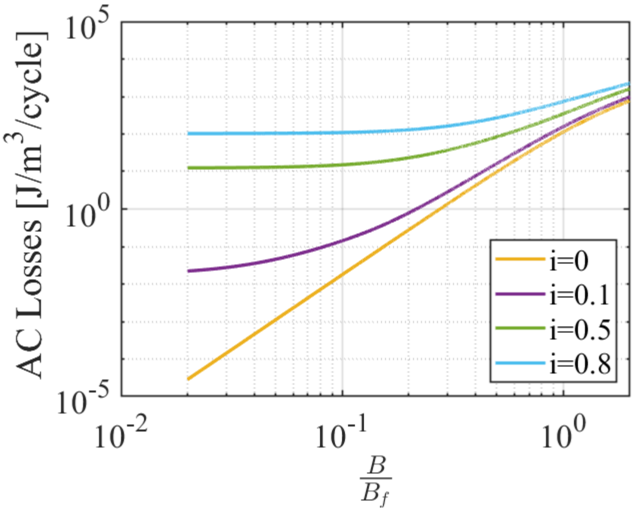

Figure 2.2.5: *Enlarged view of Fig.* 2.2.4, *showing only the results of Schonborg's formulae in the low field region* (B_f = 4 mT).

2.2.6 Kajikawa's formulae

The last analytical formulation proposed is the one that inspired the work regarding a new analytical formulation in this thesis. These formulae were presented by K.Kajikawa and S. Awaji in [91–93]. The formulae in (2.2.34) can evaluate the

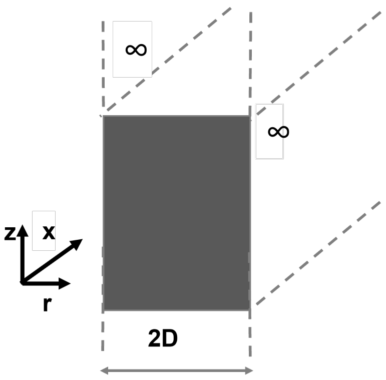

Figure 2.2.6: *Sketch of an infinite slab, the dimensions of the slab along the x and r coordinates are considered infinite.*

instantaneous power losses per unit of volume of an infinite superconducting slab due to the action of both a transport current and an external magnetic field. The transport current and the magnetic field are required to be in phase with each other. These formulae hold only for the first energization of the slab, and only when the time derivative of the transport current (and so the magnetic field in phase with it) is positive. The main hypotheses used in the determination of these formulae are:

- Use of the critical state model.
- use of the slab approximation: each superconducting stack is homogenized and treated as an infinite slab, only one dimension is considered finite, and its length is indicated as 2D (see Fig. 2.2.6).

$$P = \frac{B_p^2}{2\mu_0}\begin{cases} K_1 & \text{if} \quad 0 \leq B_e < B_i \\ K_2 & \text{if} \quad B_i \leq B_e < B_p \\ K_3 & \text{if} \quad B_e \geq B_p \end{cases} \tag{2.2.34}$$

with K_1, K_2 and K_3 defined as follows:

$$K_1 = \frac{\dot{B}_e B_e^2}{B_p^3} + \frac{\dot{B}_e}{B_p}\left[2\frac{B_e}{B_p}\frac{I}{I_c} - \left(\frac{B_e}{B_p}\right)^2\right] + \frac{\dot{I}}{I_c}\left[\left(\frac{B_e}{B_p}\right)^2 + \left(\frac{I}{I_c}\right)^2\right] \tag{2.2.35}$$

$$K_2 = \frac{\dot{B}_e B_e^2}{B_p^3} + \left(\frac{I}{I_c}\right)^2 \frac{\dot{B}_e}{B_p} + 2\frac{B_e}{B_p}\frac{I\dot{I}}{I_c^2} \tag{2.2.36}$$

$$K_3 = \frac{\dot{B}_e}{B_p} + 2\frac{I\dot{I}}{I_c^2} + \frac{\dot{B}_e}{B_p}\left(\frac{I}{I_c}\right)^2 \tag{2.2.37}$$

In (2.2.34) B_p is the penetration field, is the value of the magnetic field that once reached lets the superconducting slab be fully penetrated by the current density.

$$B_p = \mu_0 J_c D \tag{2.2.38}$$

J_c is the critical current density, while B_i is the self-field [93], defined as

$$B_i = B_p \frac{I(t)}{I_c} \tag{2.2.39}$$

I(t) and I_c are the transport current and the critical current of the slab respectively. $\dot{B}_e$ is the time derivative of the external field, while $\dot{I}$ is the time derivative of the transport current.

Despite the limitations previously described and the approximation introduced by the hypothesis formulated, these formulae have successfully been used for the evaluation of the hysteresis losses in large magnets [91].

2.2.7 Final remarks on analytical formulae

The analytical models described in this section have to be considered with great care, given some relevant limitations. As a first limitation, their applicability is limited to simple geometries; their reliability for use in structured tapes (filaments, stabilizers, magnetic materials, etc.) or more complex geometries should be carefully checked. As a second limitation, these formulae are based on the Bean critical state model. Thus, they cannot account for the magnetic field dependence of the superconductor's critical current density, as well as possible inhomogeneities of the conductor itself. Typically, the formulae assume that the tapes have an infinite length so that the end-effects cannot be taken into account. It is also assumed that the external magnetic field is uniform and that the self-fields have simple time dependencies, such as those generated by an AC current or a current ramp. Although they are very easy to implement, analytical models unfortunately cannot give accurate results in complex cases. Another issue that arises is that most of the formulae presented in this section provide an evaluation of AC losses in terms of energy per cycle rather than instantaneous power. This limitation can hinder the assessment of real-time device performance, as instantaneous power is a more relevant metric for dynamic conditions especially for the evaluation of the temperature margin. Nonetheless, analytical models are still extremely useful for a quick assessment of the losses in simple configurations and for the validation of numerical models, which are discussed in the next section.

2.3 Main numerical methods

Throughout the years, numerous finite element methods (FEM) models have been devised to investigate the electromagnetic behavior of HTS tapes. These models employ the time-dependent form of Maxwell's equations to calculate the temporal evolution of electric field and current density distributions in coated conductors. The quantification of these quantities begins with the differential formulation of Maxwell's equations:

$$\begin{cases} \nabla \cdot \mathbf{E} = \frac{\rho_c}{\epsilon} \\ \nabla \cdot \mathbf{B} = 0 \\ \nabla \times \mathbf{E} = -\frac{\partial \mathbf{B}}{\partial t} \\ \nabla \times \mathbf{B} = \mu \left(J + \epsilon \frac{\partial \mathbf{E}}{\partial t} \right) \end{cases} \tag{2.3.1}$$

Where ρ_c is the charge density, μ is the magnetic permeability, and ϵ is the electric permittivity.

Numerical models can give more reliable results than analytical ones, but they require a much greater computational burden and are significantly more complex to implement. In the first part of this section, the various formulations proposed in the literature are briefly described. In the second part, selected numerical models are presented, given their promising characteristics for application in the field of fusion magnets. In the third part, homogenization techniques required to deal with tape stacks or complex structures are described. The numerical models for the calculation of AC losses in superconducting tapes are based on various formulations of the laws of electromagnetism. Among these, it is worth mentioning the *H formulation*, the *A-V formulation*, the *T- Φ formulation*, the *T- A formulation* and the *E formulation*. The latter is not extensively adopted in the scientific community and is thus not fully treated here. The fundamental equations of these formulations are reported in Table 2.3.1. Each method utilizes a different set of equations and state variables, despite that the losses are always evaluated as the scalar product of **E** and **J**. The comparisons between numerical models available in the literature are not very numerous. Many comparisons were done in different configurations, with corresponding different problem geometry, dimensionality, constraints, etc. This might explain why the conclusions on the convenience of each method are not unanimous in the scientific community, as explained in [94].

Table 2.3.1: Preminent numerical methods

Formulation	*Equations*	*Definitions*	*References*
H formulation	$\nabla \times \rho \nabla \times \mathbf{H} = -\mu \frac{\partial \mathbf{H}}{\partial t}$	$\mathbf{J} = \nabla \times \mathbf{H}$	[95–101]
A-V formulation	$\nabla^2 \mathbf{A} = \mu\sigma\left(\frac{\partial \mathbf{A}}{\partial t} + \nabla V\right)$ $\nabla \cdot \sigma\left(\frac{\partial \mathbf{A}}{\partial t} - \nabla V\right)$	$\mathbf{B} = \nabla \times \mathbf{A}, \mathbf{E} = -\frac{\partial \mathbf{A}}{\partial t} - \nabla V$ $\sigma = \sigma(\mathbf{E})$	[102–107]
T- Φ formulation	$\nabla \cdot \mu(\mathbf{T} - \nabla \Phi) = 0$ $\nabla \times \rho \nabla \times \mathbf{T} = -\mu \frac{\partial(\mathbf{T} - \nabla \Phi)}{\partial t}$	$\mathbf{J} = \nabla \times \mathbf{T}, \mathbf{H} = \mathbf{T} - \nabla \Phi$ $\rho = \rho(\mathbf{J})$	[108–112]
T- A formulation	$\nabla \times \left(\frac{1}{\mu} \nabla \times \mathbf{A}\right) = \mathbf{J}$ $\nabla \times (\rho \nabla \times \mathbf{T}) = -\frac{\partial \mathbf{B}}{\partial t}$	$\mathbf{J} = \nabla \times \mathbf{T}$ $\mathbf{B} = \nabla \times \mathbf{A}$	[94, 100] [113–119]
E formulation	$\nabla \times \nabla \times \mathbf{E} = \frac{\partial(\sigma \mathbf{E})}{\partial t}$	$\sigma = \sigma(\mathbf{E}), \frac{\partial \mathbf{B}}{\partial t} = -\nabla \times \mathbf{E}$	[120–123]

2.3.1 H formulation

The H-formulation is one of the most widely adopted for the calculation of losses in HTS tapes in the scientific community. It is derived from a combination of the Ampere's law and the Faraday's law as follows in (2.3.2):

$$\nabla \times \rho \nabla \times \mathbf{H} = -\mu \frac{\partial(\mathbf{H} + \mathbf{H_0})}{\partial t} \tag{2.3.2}$$

where $\mathbf{H_0}$ is the external magnetic field source term. This model can easily be implemented in commercial software such as COMSOL Multiphysics® [124]. A major drawback of this formulation is the need to set a finite resistivity in the region outside the conductor (air), which may result in observing non-physical leakage currents, as reported in [117]. This issue can be prevented through the use of cohomology basis functions, treated in [100].

2.3.2 A- V formulation

The A-V formulation is one of the most extensively adopted approaches for the solution of electromagnetic problems in different fields of application. However, it is applied less frequently than the H-formulation in the modeling of HTS tapes. The state variables are the electric scalar potential (V) and the magnetic vector potential ($\mathbf{A}$), defined by:

$$\mathbf{B} = \nabla \times \mathbf{A}, \quad \mathbf{E} = -\frac{\partial \mathbf{A}}{\partial t} - \nabla V \tag{2.3.3}$$

The A-V formulation is represented by the following system of equations

$$\begin{cases} \nabla^2 \mathbf{A} = \mu\sigma\left(\frac{\partial \mathbf{A}}{\partial t} + \nabla V\right) \\ \nabla \cdot \sigma\left(\frac{\partial \mathbf{A}}{\partial t} - \nabla V\right) \end{cases} \tag{2.3.4}$$

This formulation is particularly advantageous when the vector potential can be reduced to a scalar quantity, as is typical in 2D axisymmetric problems. The major drawback of this approach is that numerical oscillations can be observed when the superconductor power law is too sharp, i.e. is characterized by high values of n-index ($n > 25$) [119]. These oscillations are mainly related to the numerical calculation of the time derivative of the vector potential. Moreover, expressing the constitutive law as $\mathbf{E} = \sigma\mathbf{J}$ may cause problems in the non-linear solver since σ can reach exceeding high values in a superconductor.

2.3.3 T - Φ formulation

This formulation is derived from Faraday's law and Gauss's magnetic law ($\nabla \cdot B = 0$). The state variables are the current vector potential $\mathbf{T}$ and the magnetic scalar potential Φ, defined according to the following expressions:

$$\nabla \times \mathbf{T} = \mathbf{J}, \quad \mathbf{H} = \mathbf{T} + \mathbf{T_0} - \nabla\Phi \tag{2.3.5}$$

where $\mathbf{T_0}$ represents the current source term. This formulation can be expressed as:

$$\begin{cases} \nabla \cdot \mu(\mathbf{T} + \mathbf{T_0} - \nabla\Phi) = 0 \\ \nabla \times \rho\nabla \times (\mathbf{T} + \mathbf{T_0}) = -\mu\frac{\partial(\mathbf{T}+\mathbf{T_0}-\nabla\Phi)}{\partial t} \end{cases} \tag{2.3.6}$$

Although this method is sufficiently reliable, it is generally not adopted in commercial software and thus it is not widely used. The main drawback of this formulation, which hinders its wide diffusion in the scientific community, is the complexity of the corresponding implementation. The main advantage of this approach is that it automatically guarantees that the divergence of the current density is always null. Therefore, differently from the H-formulation, this method does not allow the numerical generation of leakage currents.

2.3.4 T- A formulation

This formulation was recently proposed by H. Zhang in [118], where it was validated in the case of a thin-disc magnetization by comparing the results to analytical ones. The model was also validated for a large number of HTS tapes against the well-established H-formulation [113] and was implemented in the study of stacks of REBCO coated conductors, coils [113], and HTS cables, such as conductors on round core and twisted stacked-tape conductors [116]. The computation regions are subdivided into two parts: a superconducting region and a non-superconducting one. The superconducting sheet is modeled using the T formulation, while the non-superconducting space is modeled using the A formulation. In this approach, the magnetic vector potential A is computed in the entire geometry as:

$$\nabla \times \left(\frac{1}{\mu} \nabla \times \mathbf{A} \right) = \mathbf{J} \tag{2.3.7}$$

where **J** is the current density, µ the permeability of the material and **A** is defined as the magnetic vector potential, defined by the usual relation $\mathbf{B} = \nabla \times \mathbf{A}$.

The field vector **T** is also a vector potential, defined as $J = \nabla \times T$, and is only computed in the superconducting domain as:

$$\nabla \times (\rho \nabla \times \mathbf{T}) = -\frac{\partial \mathbf{B}}{\partial t} \tag{2.3.8}$$

where ρ is the resistivity of the superconductor, derived from the power law. It is important to notice that the A–formulation can be exchanged with the classic H–formulation, leading in this case to the so-called T–H formulation.

2.4 Consideration on the main model and alternatives

The pros and cons of the numerical formulations described in the previous sections are reported in Fig. 2.4.1, taken from references [14, 123, 125]

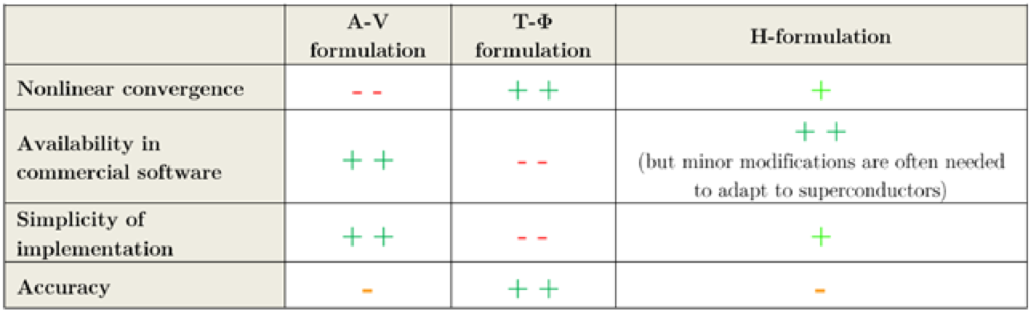

	A-V formulation	T-Φ formulation	H-formulation
Nonlinear convergence	- -	+ +	+
Availability in commercial software	+ +	- -	+ + (but minor modifications are often needed to adapt to superconductors)
Simplicity of implementation	+ +	- -	+
Accuracy	-	+ +	-

Figure 2.4.1: *Advantages and drawbacks of the different formulations for the computation of AC losses* [14].

The following considerations can be made in the comparison between formulations:

- Among the T- Φ formulation, the E formulation and the A- V formulation to compute AC losses in straight tapes, the T- Φ formulation is the most efficient.
- Although the A- V formulation only requires the computation of one variable ($\mathbf{A}$) at each node, the need to differentiate the vector potential with respect to time and then insert it into a $\mathbf{J(E)}$ constitutive law generally leads to convergence issues.
- The E formulation can be used too when the n index is not too large ($n < 20$). An example is presented for BSCCO tapes in [125]).

A comparative analysis should be applied to determine the best method for the determination of AC losses in a superconducting device since proper benchmarking is missing in the literature, as stated in [94]. In fact, starting from the tape level and moving to more complex geometries, few comparative studies are reported in the literature. Several other modeling techniques have been developed to determine efficient numerical solutions for the computation of losses in HTS tapes. Some of these other models will now be presented.

2.4.1 Campbell model

Proposed by A. M. Campbell in [126], this approach is based on the Bean critical state model. In the literature, few applications of this model are presented, but its peculiarities make it a useful tool for modeling HTS superconductors. The model is based on the consideration that the numerical methods to compute the losses in superconductors can be essentially divided into two categories:

- Methods computing the critical state directly (not implementable in commercial FEM software).
- Models using a non-linear **E**- **J** law, such as $\mathbf{E} \propto \mathbf{J}^n$, where n is high (high values of the n-index produce numerical instabilities). Thus, the "exact" critical state ($n \to \infty$) can be seen as the limit of the power law characteristics for high values of n.

The method proposed by Campbell solves the critical state directly, but it can also be implemented in commercial software, which is the main peculiarity of this approach. The method is based on the force–displacement curve of the vortex flux lines and the equation can be expressed in terms of the magnetic vector potential. The flux flow resistivity can be added and, since the term 1/n appears (instead of the term n), the numerical instabilities can be avoided. The author of the method states that it is particularly advantageous for problems involving trapped flux where assuming a power law would lead to a decay, with a decay rate dependent on the power index. For a tape subjected to an external field **B**, carrying a transport current density **J**:

$$\mu_0 \mathbf{J} = \nabla \times \nabla \mathbf{A} = -\mu_0 \mathbf{J_c} \left(1 - e^{\left|\frac{A}{Bd}\right|}\right) \tag{2.4.1}$$

where d is the characteristic distance, typically about a quarter of the vortex spacing. The final expression considering both the flux flow resistivity and the variation of the direction of movement of the vortex, is equal to:

$$\nabla \times \nabla \mathbf{A} = -\mu_0 \mathbf{J_p} + k \left[\left(1 - e^{-\left|\frac{\mu_0 J_c (A-A_p)}{kBd}\right|}\right)\right] \tag{2.4.2}$$

where ρ is the flux flow resistivity, which is current dependent, A_p is the peak value of vector potential when the current or the field are raised from zero to their maximum values, J_p is the corresponding current density, and k is given by the expression

$$k = \mu_0 J_c \mathrm{sgn}(A_p - A) - \mu_0 J_p \tag{2.4.3}$$

The electric field and current density can be expressed as:

$$\mathbf{E} = k\mathbf{J}^n; \quad \mathbf{J} = \left(\frac{\dot{\mathbf{A}}}{k}\right)^{\frac{1}{n}} \tag{2.4.4}$$

which allows the viscous term in (2.4.2), namely ($\mu_0 \dot{\mathbf{A}}/\rho$), to be simplified as$\mu_0 J$, which is generally a small number. This feature of the model is crucial for granting the numerical stability of the problem. After solving (2.4.2) for the main model unknown, which is the vector potential, the fields **E** and **J** can be determined as in (2.4.4). Finally, the AC losses can be evaluated as

$$\int \mathbf{E} \cdot \mathbf{J} dV \tag{2.4.5}$$

2.4.2 Thin strip approximation

This model was widely adopted by N. Amemiya in [15] to compute AC losses in twisted multifilamentary coated superconductors. The model proposed was developed from the power law of the superconductor and a thin strip geometric approximation of the tape. The model was then implemented in a FEM code for the calculus of the currents and the magnetic flux distribution, from which the temporal evolution of the AC losses can be derived. The AC losses computed by the model are due to an AC transverse magnetic field applied to the tape.

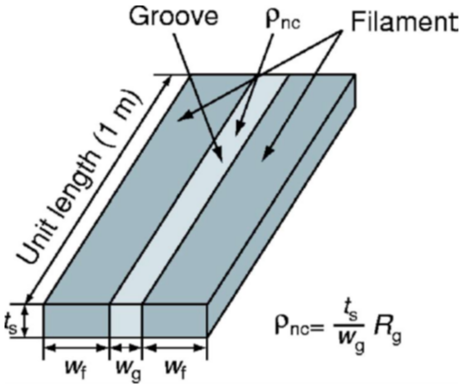

Figure 2.4.2: *Model of filaments and groove between filaments: a conductive layer comprising superconductor filaments and grooves filled with resistive material R_g is the transverse resistance of groove between two filaments per unit of length* [15].

The superconductor filaments are connected with each other through transverse resistances and it is assumed that the grooves between filaments are filled with a resistive material, as shown in Fig. 2.4.2.

The finite resistance between the filaments and the finite twist pitch in twisted multifilamentary coated superconductors results in the frequency dependence of the magnetic flux penetration process and frequency-dependent AC loss characteristics. Since the conductive layer comprising the superconductor filaments and grooves filled with resistive material is very thin, the thin strip approximation described in [127] is adopted. It is assumed that the current flows only in the direction tangential to the wide face of the conductor.

The electromagnetic field distribution is assumed to be uniform along the thickness of the tape, whereas the superconductor layer is modeled as a thin curved surface that follows the three-dimensional shape of the tape (when the tape is not straight), as shown in Fig. 2.4.3. The model proposed is based on the current density vector potential T, with the use of the constitutive material law between the electric field and the current density. Adding the Faraday's law and the Biot - Savart's law yields:

$$\nabla \times \left(\frac{1}{\sigma} \nabla \times \mathbf{T} \right) + \frac{\partial}{\partial t} \left(\frac{\mu_0}{4\pi} \iiint_V \frac{(\nabla \times \mathbf{T}') \times \mathbf{r}}{r^3} dV \right) + \frac{\partial \mathbf{B_{ext}}}{\partial t} = 0 \qquad (2.4.6)$$

By applying the thin strip approximation, (2.4.6) can be reduced to:

$$\left(\nabla \times \left(\frac{1}{\sigma} \nabla \times \mathbf{nT} \right) \right) \cdot \mathbf{n} + \frac{\partial}{\partial t} \left(\frac{\mu_0 t_s}{4\pi} \iint_{S'} \frac{(\nabla \times \mathbf{n}'\mathbf{T}') \times \mathbf{r} \cdot \mathbf{n}}{r^3} dS' + \mathbf{B_{ext}} \cdot \mathbf{n} \right) = 0 \qquad (2.4.7)$$

where **T** and **T'** are the current vector potentials at the field point and source point of the self-magnetic-field, respectively; **n** and **n'**, the normal vectors of the wide face of the conductor at the field point and source point, respectively. $\mathbf{B_{ext}}$ is the external magnetic field, which is assumed orthogonal to the conductor at the center of the twist pitch, as shown in Fig. 2.4.3.

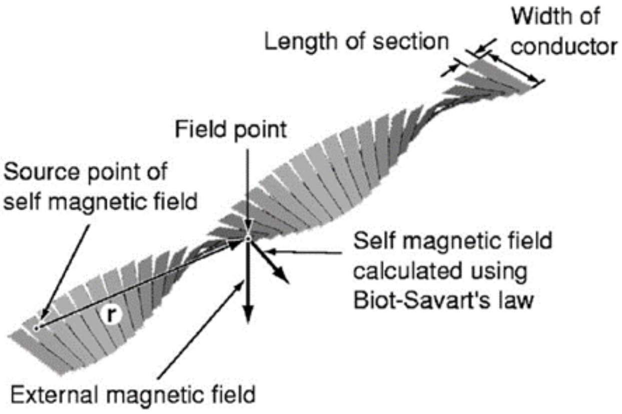

Figure 2.4.3: *Twisted multifilamentary coated conductor described with the thin strip approximation model. The coated conductor is subdivided axially into short flat sections and rotated along the conductor axis to form a twisted geometry* [15].

Thanks to the thin strip approximation, the current density component orthogonal to the wide face of the conductor is neglected. Thus, **T** has a component normal to the wide face of the conductor alone, and the problem is reduced to a two-dimensional problem for the scalar variable **T** on the plane parallel to the wide face of the conductor.

2.4.3 Other, less widespread, numerical models

Integral approaches could help reduce the computation time when simulating complex three-dimensional geometries; however, their reliability must be carefully assessed. Integral methods solve the integral form of the PDE (partial differential equation) instead of the differential ones presented in the previous sections. The main weakness of the integral methods is that the matrix describing the system is a full matrix instead of a sparse matrix typical of the finite element method (FEM) approach. The full matrix needs to be stored using a large amount of memory, much greater than the one required for sparse matrices. The memory requirements typically increase with the square of the number of degrees of freedom (Dofs), which creates problems when dealing with large structures. Due to these issues, the integral methods have not been widely applied in the scientific community. However, given the recent development of efficient techniques of matrix compression and the increase of memory in modern computers, these methods could become a useful resource. The main integral methods are the boundary integral methods (BIM) and the volume integral methods (VIM). The former is based on solving the problem PDEs at the boundaries of the domain, thus generating a small number of Dofs, but is not suited for solving problems involving superconductors, due to their inability to handle non-linearities [125]. The latter can instead represent a valid solution even in cases involving non-linear constitutive laws. The drawback is that the number of Dofs generated is greater than the one resulting from the application of BIM methods. All the numerical methods proposed in this document are general and can be applied to a large variety of problems (structural analysis, fluid dynamics, etc.), but the partial element electric circuit (PEEC) proposed by A. Ruehli in [128] was developed specifically for electromagnetic problems. The PEEC relies on a semi-analytical integral method to determine the electrical components of an electric circuit representing the system. Essentially, the domain is subdivided into a number of sub-domains, to each of which an electric circuit is associated. This method was successfully applied by Noguchi and Wang in the study of non-insulated REBCO pancakes [76]. Its main advantage is to enable a connection between the model of the device under analysis and an external electric circuit such as other electric components or the electric network itself. Sophisticated variational methods may be more efficient and flexible for the solution of 3D problems, but they require a very significant work for the identification of the various parameters and regimes. Several examples of variational methods were proposed by L. Prigozhin [129] and E. Pardo [130].

2.5 Homogeneization techniques

To reduce the computational burden of the solvers, homogenization techniques [16,17,129,131,132] must be adopted, although the solutions obtained are intrinsic approximations of the real ones. Thus, the choice of the homogenization technique must be carefully evaluated. An overview of the homogenization methods proposed in the literature is presented in this section. The homogenization models that will be presented are mainly applied to a stack of tapes. However, a model employed for the study of coils (Neighbor approximation) is also reported, to better express the idea that homogeneization is not exclusively used for stacks. Homogenization techniques aggregate detailed microscopic properties of the conductor into bulk properties that can be used to represent the homogenized system at larger length scales and hence reduce computational cost.

2.5.1 Anisotropic homogeneous-medium approximation

This approach represents the most classical and widely used type of homogenization. As shown in the sketch of Fig. 2.5.1, it is based on the assumption that a finite stack of height 2b of thin superconducting tapes, all carrying a fixed current I, can be approximated through an anisotropic superconducting bar with critical current density defined as:

$$J_c = \frac{I}{2aD} \tag{2.5.1}$$

where a is the half-width of the tape, and D is the distance between two consecutive parallel tapes of the stack.

The current density in the homogenous bulk conductor must respect the following integral constraint:

$$\int J dx = \frac{I}{D} \tag{2.5.2}$$

For small values of the ratio D/a, the anisotropic homogeneous-medium approximation gives a reasonably accurate estimate of the AC losses in a finite stack. Then, the results obtained for a stack can be used to calculate the transport losses in a pancake coil. Under the assumption of the critical state model that the critical current density is independent of the magnetic flux density, an analytical formula was obtained by Clem [16] for the calculation of the transport current AC losses per unit of length along the y direction:

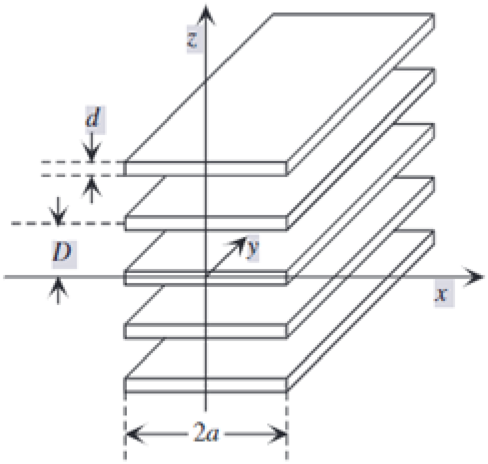

Figure 2.5.1: *Sketch of a finite stack of height 2b in the z direction of superconducting tapes of infinite length in the y direction to be homogenized in a single bulk type conductor* [16].

$$Q' = 4Q'_{init} \tag{2.5.3}$$

where Q'_{init} is the energy per unit length dissipated upon the initial penetration of magnetic flux and is expressed as follows

$$Q'_{init} = -4J_c \int_0^b dz \int_{c(z)}^a (a-x)B_z(x,z)dx \tag{2.5.4}$$

where b is the half height of the stack, c(z) defines the border of the region, comprised between c(z) and a, over which the magnetic flux density in z direction penetrates and the current density reaches its critical value. B_z is the component of $\mathbf{B}$ along the direction orthogonal to the tape's broad face. Prigozhin and Sokolovsky improved in [129] the anisotropic homogeneous-medium approximation introduced by Clem, by removing unnecessary simplifying assumptions on the current density in the subcritical zone and on the shape of the boundary of such zone. They could then derive a numerical algorithm based on the variational formulation mentioned in Section 2.4.3. They demonstrated that if the number of tapes reaches the order of one hundred, the numerical computations through variational methods become very time-consuming while the homogeneous approximation gets more advantageous.

2.5.2 Neighbor approximation

This approach was presented by E. Pardo in [17] as a technique to accelerate the computing process of an MMEV (multi magnetic energy variational) method and to provide an alternative to another widely adopted homogenization method, namely the uniform approximation. The neighbour approximation technique is quite general, and can also be applied to FEM-based models. The approach is based on approximating the effect of the whole coil on a certain turn as a given applied magnetic field. In this sense, the technique is similar to the uniform approximation. However, in the uniform approximation, the current density is assumed uniform in all remaining turns apart from the one under analysis. The issue with this approach is that the neighbouring turns shield the background magnetic field, in a similar way as in a stack of tapes [130].

Therefore, neglecting this shielding effect of the neighbouring turns the usual uniform approximation fails to predict the current density distribution in the coil and the corresponding AC losses. In particular, this effect is important in windings manufactured as stacks of pancake coils wound from coated conductors. As a matter of fact, in these windings, the shielding effect is very strong. In this respect, good advances were made with the anisotropic homogeneous approximation detailed in the previous Sectio but Pardo states that this approach cannot be applied neither to coils based on tapes or wires with a superconducting core of non-negligible thickness (such as Bi-2223 tapes or Bi-2212 or MgB2 wires) nor to pancake coils with a large separation between turns.

The neighbour approximation solves these issues by accounting for the magnetic shielding effect due to the magnetization currents flowing in the neighbouring turns. This approximation is based on the fact that the radial distance from the tape under analysis where the magnetic field is affected by the non-uniformity of the current density distribution is of the same order as the tape width. Therefore, this methodology assumes that the current distribution is uniform only in the turns that are located at a distance from the turn under analysis greater than a certain threshold distance δ. As shown in Fig. 2.5.2 [17], this influence distance is in the order of the tape width. In particular, the results reported in Fig. 2.5.2 were obtained for a constant J_c, a transport current equal to 20% of the critical current, and no applied magnetic field. The two curves shown in the plot correspond to geometric lines parallel (grey) and perpendicular (red) to the tape surface, with their origin at the center of the tape.

In the neighbour approximation to obtain J (or another state variable) in turn i, the numerical method used calculates the non-uniform current distribution of J in the set of turns T_i that respect the condition:

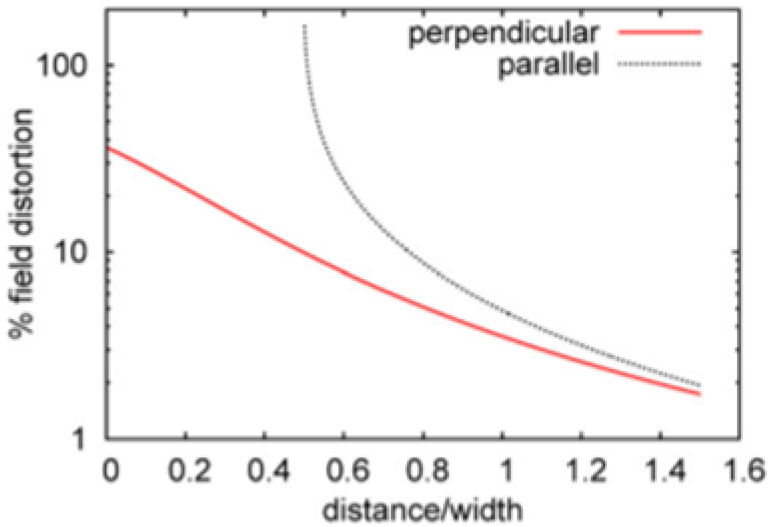

Figure 2.5.2: *Sketch of a finite stack of height 2b in the z direction of superconducting tapes of infinite length in the y direction to be homogenized in a single bulk type conductor* [17].

$$|\mathbf{r_j} - \mathbf{r_i}| \leq \delta \tag{2.5.5}$$

where $j \in T_i$, and r_j and r_i are the central positions of the cross-section of turns j and i, respectively. In the calculation, a certain total current I in each turn of T_i and the applied magnetic field B_a and vector potential A_a created by the rest of the turns are fixed. The values of B_a and A_a are

$$\begin{aligned} \mathbf{B_a}(\mathbf{r}) &= I \sum_{j \in T_i} \mathbf{b_j}(\mathbf{r}) \frac{1}{S_j} \\ \mathbf{A_a}(\mathbf{r}) &= I \sum_{j \in T_i} \mathbf{a_j}(\mathbf{r}) \frac{1}{S_j} \end{aligned} \tag{2.5.6}$$

where S_j is the cross-sectional area of turn j, and $\mathbf{b_j}(\mathbf{r})$ and $\mathbf{a_j}(\mathbf{r})$ are the magnetic field and vector potential, respectively created by turn j per unit of current density, assuming a uniform current density. It is important to note that the distribution of J is calculated in all turns of T_i, not only in the i^{th} turn. Thus, the shielding currents in the turns surrounding the turn of study are taken into account.

Indicating with n_T the number of turns discretized in detail (essentially the turns belonging to the set T_i), which is referred to as the order of the method, and with N the total number of turns of the coil, it was found out that only if

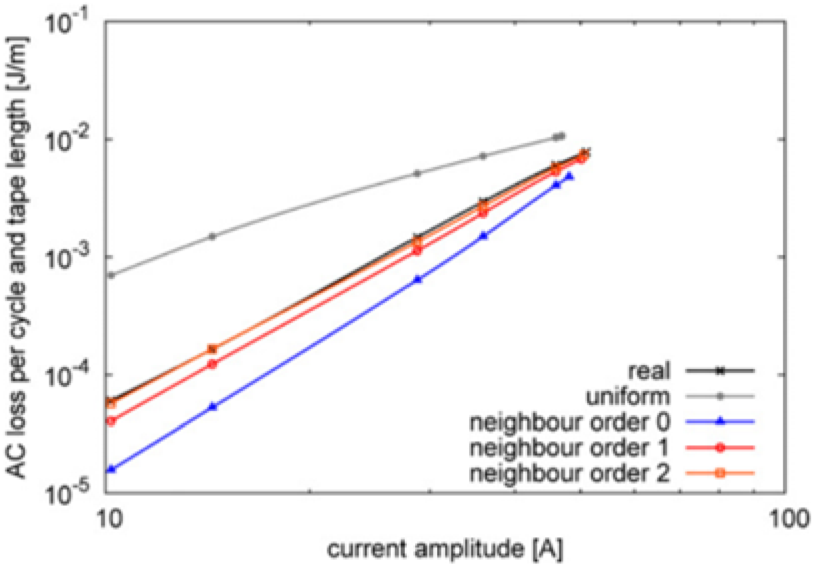

Figure 2.5.3: *Comparison of AC losses per cycle and tape length in a single pancake obtained using different orders of the neighbour approximation, the uniform approximation and the real ones* [17].

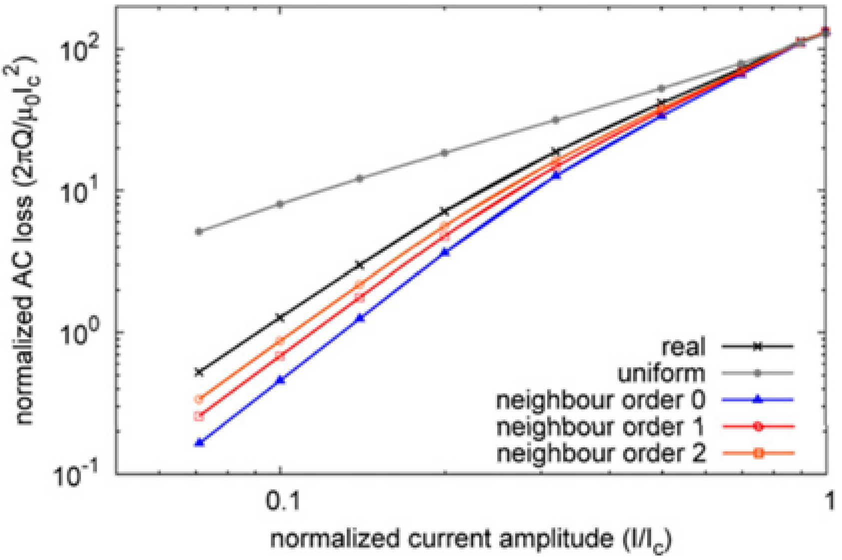

Figure 2.5.4: *Comparison of the normalized AC losses for a stack of pancakes obtained through different orders of the neighbour approximation, the uniform approximation, and the real ones* [17]).

the condition in (2.5.7) is verified, then the neighbour approximation reduces the overall computing time.

$$n_T^2 < N \tag{2.5.7}$$

As shown in Figs. 2.5.3 and 2.5.4, this homogenization technique gives excellent results, by speeding up the calculation without remarkable loss of accuracy with respect to the detailed modeling of all individual turns.

2.5.3 Densification method

The densification is not regarded as a proper homogenization technique but serves the same purpose of reducing the computational burden and is therefore described here. This method was recently proposed by E. Berrospe-Juarez et al. in [18]. In the densification method, the number of elements is reduced by employing a reduced number of densified tapes. The densified tapes merge a given number of tapes into a single tape, during the densification process. The obtained densified tapes preserve their original geometry and concentrate the transport current of their surrounding tapes, while the surrounding tapes are erased, as shown in Fig. 2.5.5. In classical homogenization, the electromagnetic behavior of the original stack is preserved through the distribution of the transport current all over the homogenized bulk, while with the densification technique, this requirement is met using the concentration of the transport current in the densified tapes. The densified model does not include the normal conductors forming part of the HTS tapes, the resistivity of superconducting subdomains of the densified tapes is derived from the power law shown and is shown in (2.1.2), and the definition of the critical current reported in (2.5.8) based on Kim's critical state model [38].

$$J_c(\mathbf{B}) = \frac{J_{c0}}{1 + \frac{\sqrt{k^2 B_\parallel^2 + B_\perp^2}}{B_0}} \tag{2.5.8}$$

Where k is the anisotropic factor, $B_\parallel$ and $B\perp$ the components of $\mathbf{B}$. The value of J_c is replaced by a densified critical current density J_{cd} defined as

$$J_{cd} = dJ_c \tag{2.5.9}$$

where d is the number of tapes merged into a single densified tape. The transport current in the densified tapes is given by:

$$I_{tr} = dI_k \tag{2.5.10}$$

where I_k is the transport current in the original non-densified tapes

It is necessary to add one integral constraint per densified tape with the proper transport current I_{tr}. It is important to notice that d doesn't need to be an integer

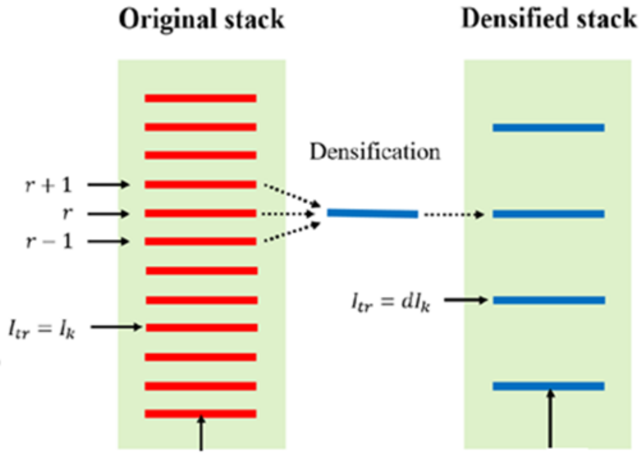

Figure 2.5.5: *Example of application of densification for a stack of superconducting tape* [18].

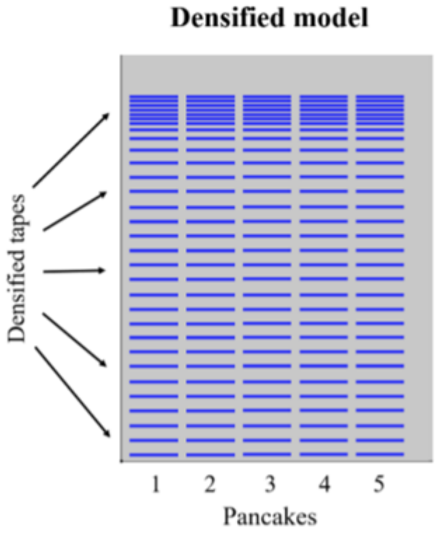

Figure 2.5.6: *Example of non-homogeneous densification* from [18].

and it can even differ from one densified tape to another, for example, a stack of five tapes can be discretized with two densified tapes both with d = 2.5 or one with d = 2 and the other with d = 3. Once the current density distribution is computed, the losses can be calculated in the densified tapes. The losses in the densified tapes are divided by their corresponding d, and these values are used to interpolate the losses in each tape of the original stack. The accuracy of the densified models may be degraded due to the nature of the densified tapes, which generate larger self-fields and are located at larger distances between tapes than in the original non-densified model. Therefore, the number and the position of the densified tapes must be carefully assessed. In the region where there is a larger variation of the current density, it can be convenient to increase the number of densified tapes. The densification of the tapes can be non-homogeneous, meaning that in the region of interest more densified tapes can be used (dense region) than in the other regions, see Fig. 2.5.6.

2.6 Final remarks on literature formulae and models

The main issues that may arise when simulating AC losses in a twisted stacked conductor are listed in the following.

- Coupling of the tapes: the current distribution depends on the mutual interferences between tapes, at least those belonging to the same stack of the cable. It is therefore not possible to neglect the mutual interaction between tapes; homogenization techniques such as the neighbor approximation should be considered to describe the stack.
- 3D geometry: a 2-D approximation can reduce the computational burden when considering short cable segments. However, when simulating large magnets, these simplifying assumptions might not hold.
- Computational burden: the twisted stacked configuration introduces a greater number of unknowns as compared to individual tapes. The formulation to be adopted, as well as the solving approach (integral or differential), must be carefully evaluated.

Concerning the tools available for modeling HTS, different approaches with increasing levels of detail have been developed, both analytically and numerically. Detailed 2D and 3D Finite Element models have been developed for HTS stacks or small pancake coils, or peculiar cable layouts, such as power cables, TSTC, CORC, and Roebel cables. The main purpose of these models has been so far the study of AC losses or quench propagation in HTS tapes, stacks, small coils or cables. However, scaling up such very detailed models to the magnet size has not been yet achieved. The main issues that may arise when simulating AC losses in a twisted stacked conductor are the coupling of the tapes and the current redistribution among them, and the computational burden due to the huge number of elements to be included in the model.

3 *New analytical formulation*

3.1 Motivation

The European Union is working to develop a roadmap for harnessing fusion energy beyond the ITER project [133]. The main goal is to create a conceptual design for the demonstration power plant (DEMO) machine, which is expected to be operational around 2050. Several studies have been conducted on the DEMO magnet configuration [134–136] and the technologies that could be used [63, 137, 138]. One option being considered for the DEMO central solenoid (CS) is the insertion of an HTS insert. The twisted stacked tape cable in conduit conductor (CICC) configuration for HTS conductors is a promising solution to achieve the required magnetic field of 15 T [139]. A possible design of the HTS cable based on this technology is shown in Figure 3.1.1.

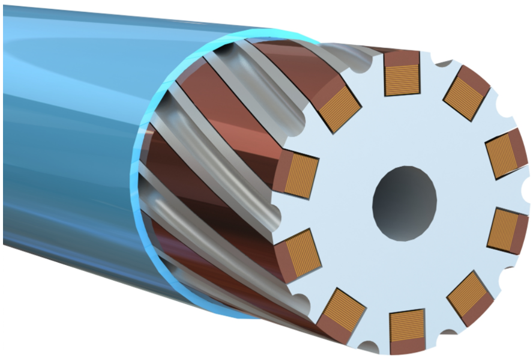

Figure 3.1.1: *Artistic view of the REBCO CICC layout designed by ENEA, composed of 10 stacks each with 30 tapes per stack* [19].

As mentioned in previous chapters, calculating losses during magnet operation is a crucial aspect of superconducting magnet design, particularly for pulsed coils like the CS of a tokamak. Accurate knowledge of the instantaneous values of these losses is essential to determine the magnet's temperature margin [80]. Accurately calculating these losses would require a 3D finite element method (FEM) model, but the computational time for such models would be prohibitively high for the complex geometry of a fusion reactor. As a result, the use of analytical formulae has been proposed as an alternative approach [19, 91, 92, 140, 141]. This chapter will present an original analytical formulation and methodology for estimating the hysteresis losses in the SC-TSTC cable configuration described in Section 1.4.1 and shown in Figure 3.1.1. The formulation presented will give the instantaneous power losses for the case when both transport current and external magnetic field are present. The twisted stacked geometry cannot be tackled straightforwardly with analytical formulae (or even 1D/2D FEM model) so a methodology for the application of analytical formulae to this kind of geometry will also be presented.

This work was carried out in collaboration with ENEA and Politecnico di Torino under the auspices of the EUROfusion consortium to investigate the AC losses in a potential HTS insert of the central solenoid of DEMO.

3.2 Analytical formulation

The idea was to follow the method used to obtain the formulae developed by Kajikawa and Awaji, shown in section 2.2.6, to extend them after the first magnetization. These formulae differently from all of the others presented have the merit to give the hysteresis losses as instantaneous power losses instead of energy loss (so averaged over a cycle), and to apply to the realistic case of both a transport current and an external magnetic field present. Having an analytical formulation that can predict, albeit with a certain error due to the assumption, the instantaneous power losses of a cable design can be an important asset in the designing phase of these kinds of conductors.

3.2.1 Hypothesys of study and developed formulae

The main assumptions made in this work are the following:

- Slab approximation: each superconducting stack is homogenized and treated as an infinite slab, only one dimension is finite, and its length is indicated as 2D (see Fig. 2.2.6).
- Critical state model: the current density in a superconducting slab can only assume the values 0 or $\pm J_c$. J_c is the superconductor critical current density.

The formulae presented in this section enable the computation of the losses per unit volume of a slab, P, expressed in $[W/m^3]$. The general equation used to develop these formulae is:

$$P = \frac{1}{2D} \int_{-D}^{D} \mathbf{E}(x) \cdot \mathbf{J}(x) dx \tag{3.2.1}$$

E(x) is the electric field profile inside the slab, while **J**(x) is the current density profile. Via the two assumptions presented in the previous section, it is possible to analytically describe the expressions of both.

E(x) can be obtained from Faraday's Law:

$$\nabla \times \mathbf{E} \quad = \quad -\frac{\partial \mathbf{B}}{\partial t} \tag{3.2.2}$$

In the slab geometry (see Fig. 3.2.1), with an external field directed along the y axis (3.2.2) is reduced to (3.2.3)

$$\frac{\partial E_z}{\partial x} \quad = \quad \frac{\partial B_y}{\partial t} \tag{3.2.3}$$

J(x) is obtained from Ampere's law:

$$\nabla \times \mathbf{B} \quad = \quad \mu_0 \mathbf{J} \tag{3.2.4}$$

which in the slab geometry is reduced to:

$$J_z \quad = \quad \frac{1}{\mu_0}\frac{\partial B_y}{\partial x} \tag{3.2.5}$$

Other important parameters for the formulation are the penetration field B_p (the value that the external field (B_e) must reach during the first magnetization to let the magnetic field fully penetrate the slab), and the self field B_i (the field generated by the transport current).

$$B_p = \mu_0 J_c D, \quad B_i = B_p \left(\frac{I}{I_c}\right) \tag{3.2.6}$$

The parameter D is half of the finite dimension of the slab (Fig. 3.2.1), while I is the value of the transport current, I_c is the critical current of the slab, and J_c the critical current density.

During a ramp-up of the external field (and transport current), the profile of **B** is as in (3.2.7). In (3.2.7) the field is written as a scalar having already stated that the only non-null component is directed along the y axis.

$$B(x,t) = \begin{cases} sgn(B_e - B_i)[|B_e - B_i| - \mu_0 J_c(D - x)] & \text{with} \quad x_1 \leq x \leq D \\ 0 & \text{with} \quad x_2 < x < x_1 \\ B_e + B_i - \mu_0 J_c(D + x) & \text{with} \quad -D \leq x \leq x_2 \end{cases} \tag{3.2.7}$$

The term $sgn(B_e - B_i)$ in 3.2.7 is needed to account for $B_i > B_e$, as a reminder for what will come $|B_e - B_i| = sgn(B_e - B_i)(B_e - B_i)$, and by definition $B_i \leq B_p$.

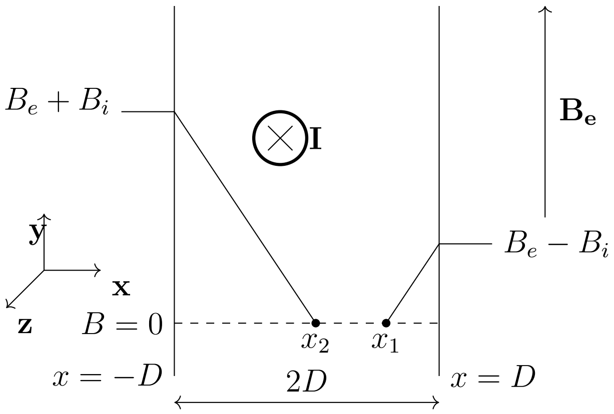

Figure 3.2.1: Graphic representation of the field profile inside the slab, during the first magnetization before the external magnetic field reaches B_p (case $B_e > B_i$).

Recalling the definitions of B_p and B_i given in (3.2.6) the expressions of x_1 and x_2 can be obtained imposing that $B(x_2) = B(x_1) = 0$:

$$\begin{aligned} x_1 &= D\frac{B_p - |B_e - B_i|}{B_p} \\ x_2 &= D\frac{B_e + B_i - B_p}{B_p} \end{aligned} \tag{3.2.8}$$

The first equation of 3.2.7 can also be written, for better clarity, as:

$$B(x,t) = B_e - B_i - \frac{\mu_0 J_c(D - x)}{sgn(B_e - B_i)} \quad \text{with} \quad x_1 \leq x \leq D \tag{3.2.9}$$

In case the external field reaches the penetration field, x_1 and x_2 collapse into a single value x_3, which defines the position of the neutral axis (where B=0). Recalling that $B_i \leq B_p$ when $B_e = B_p$ then $B_e - B_i \geq 0$

$$x_3 = D\frac{I}{I_c} \tag{3.2.10}$$

The value of x_3 is not fixed, as the transport current increases, so does x_3, meaning that the neutral axis shifts towards the right edges of the slab. A graphic representation of the field profile during the first magnetization is shown in Fig. 3.2.1. The reaching of the penetration field is shown in Fig. 3.2.2.

Applying 3.2.3 the profile of **E** is obtained by integrating in space along the x coordinate. The integration is performed separately on the left and right of the neutral axis (coordinate where the electric field becomes null). The integration constant is 0 due to **E** being null on the neutral axis. From now on, having

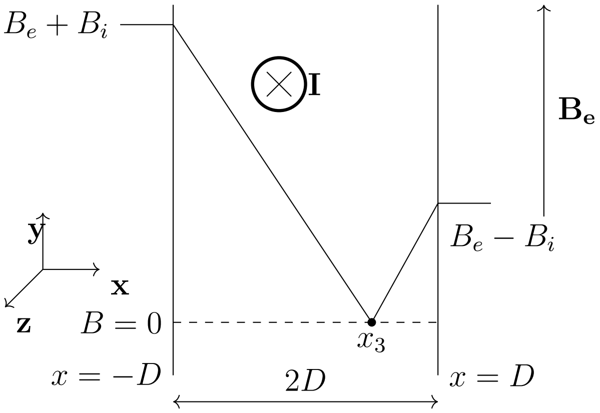

Figure 3.2.2: Graphic representation of the field profile inside the slab, during the first magnetization when the external field reaches B_p (case $B_e > B_i$).

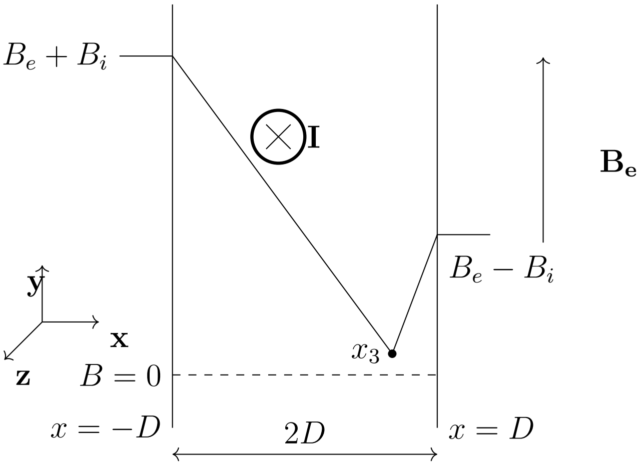

Figure 3.2.3: Graphic representation of the field profile inside the slab, during the first magnetization after the external field exceeds B_p (case $B_e > B_i$).

established that all the fields (**E**,**B**, and **J**) have only one component, the vectorial notation will be omitted.

$$\begin{aligned} E(x) &= \int_{x_1}^{x} \frac{\partial E}{\partial x} dx = \int_{x_1}^{x} \frac{\partial B(x)}{\partial t} dx = \int_{x_1}^{x} \frac{\partial \left[sgn(B_e - B_i)[|B_e - B_i| - \mu_0 J_c(D - x)] \right]}{\partial t} dx \\ &= \int_{x_1}^{x} \frac{\partial \left[sgn(B_e - B_i)[|B_e - B_i| - \mu_0 J_c(D - x)] \right]}{\partial t} dx \\ &= \int_{x_1}^{x} \frac{\partial (sgn(B_e - B_i))^2 (B_e - B_i)}{\partial t} dx \end{aligned} \tag{3.2.11}$$

In the case under exam where the current and field are in phase, the term $sgn(B_e - B_i)$ is constant. Knowing that E(x_1) = 0 the integration constant is therefore null. On the right side of the slab, the expression for E is the one in (3.2.12)

$$E(x) = \frac{\partial(B_e - Bi)}{\partial t}(x - x_1) \tag{3.2.12}$$

For the left side is mostly the same, knowing that E(x_2) = 0, the expression of the electric field is reported in (3.2.13)

$$E(x) = -\int_x^{x_2} \frac{\partial E}{\partial x} dx = \frac{\partial(B_e + Bi)}{\partial t}(x - x_2) \tag{3.2.13}$$

Written below are the equations for the electric field and the current density profile in a slab during the first positive magnetization ($\dot{I}\&\dot{B} > 0$).

$$B_e < B_p \quad E(x,t) = \begin{cases} \frac{\partial(B_e - Bi)}{\partial t}(x - x_1) & \text{with} \quad x_1 \leq x \leq D \\ 0 & \text{with} \quad x_2 < x < x_1 \\ \frac{\partial(B_e + Bi)}{\partial t}(x - x_2) & \text{with} \quad -D \leq x \leq x_2 \end{cases} \tag{3.2.14}$$

$$B_e \geq B_p \quad E(x,t) = \begin{cases} \frac{\partial(B_e - Bi)}{\partial t}(x - x_3) & \text{with} \quad x_3 \leq x \leq D \\ \frac{\partial(B_e + Bi)}{\partial t}(x - x_3) & \text{with} \quad -D \leq x \leq x_3 \end{cases} \tag{3.2.15}$$

$$B_e < B_p \quad J(x,t) = \begin{cases} sgn(B_e - B_i) J_c & \text{with} \quad x_1 \leq x \leq D \\ 0 & \text{with} \quad x_2 < x < x_1 \\ -J_c & \text{with} \quad -D \leq x \leq x_2 \end{cases} \tag{3.2.16}$$

$$B_e \geq B_p \quad J(x,t) = \begin{cases} sgn(B_e - B_i) J_c & \text{with} \quad x_3 \leq x \leq D \\ -J_c & \text{with} \quad -D \leq x \leq x_3 \end{cases} \tag{3.2.17}$$

The electric field and current density profile, inside the slab, are shown in Fig. 3.2.4 for the case depicted in Fig. 3.2.2. Where

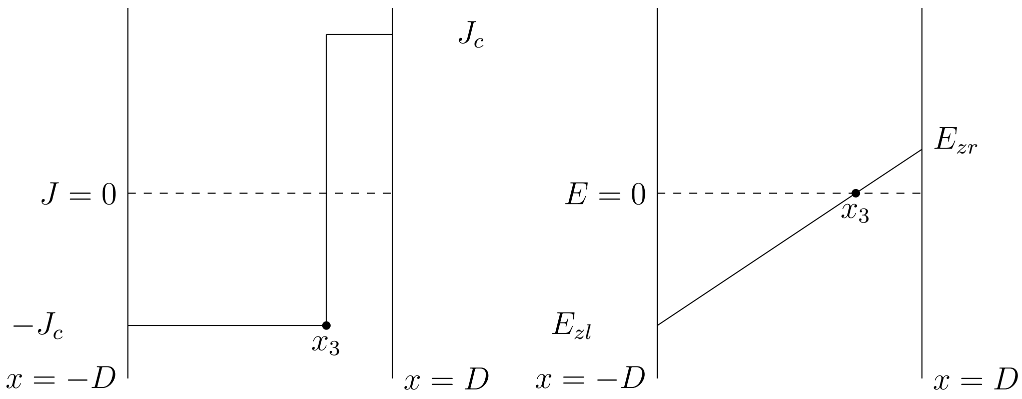

Figure 3.2.4: Graphic representation of the electric field and current density profile inside the slab, during the first magnetization when the external magnetic field reaches B_p (case $B_e > B_i$).

$$E_{zl} = -(D + x_3)\frac{\partial(B_{em} + B_{im})}{\partial t}, \quad E_{zr} = (D - x_3)\frac{\partial(B_{em} - B_{im})}{\partial t} \tag{3.2.18}$$

Applying 3.2.1 and the expressions of the field profiles ((3.2.17),(3.2.16),(3.2.15),(3.2.14)) it is possible to obtain 2.2.6. In (3.2.19) the steps for the third equation in 2.2.34(condition $B_e > B_p$).

$$\begin{aligned}
P &= \frac{1}{2D}\int_{-D}^{D}\mathbf{E}\cdot\mathbf{J}dx = \frac{1}{2D}\left[\int_{-D}^{x_3} -J_c\frac{\partial(B_e + Bi)}{\partial t}(x - x_3)dx + \int_{x_3}^{D} J_c\frac{\partial(B_e - Bi)}{\partial t}(x - x_3)dx\right] \\
&= \frac{J_c}{2D}\left[(\dot{B}_e - \dot{B}_i)\left[\frac{x^2}{2} - xx_3\right]_{x_3}^{D} - (\dot{B}_e + \dot{B}_i)\left[\frac{x^2}{2} - xx_3\right]_{-D}^{x_3}\right] \\
&= \frac{J_c}{2D}\left[(\dot{B}_e - \dot{B}_i)\left[\frac{x^2}{2} - xx_3\right]_{x_3}^{D} - (\dot{B}_e + \dot{B}_i)\left[\frac{x^2}{2} - xx_3\right]_{-D}^{x_3}\right] \\
&= \frac{J_c}{2D}\left[(\dot{B}_e - \dot{B}_i)\left[\frac{D^2}{2} - Dx_3 - (\frac{{x_3}^2}{2} - x_3^2)\right] - (\dot{B}_e + \dot{B}_i)\left[\frac{{x_3}^2}{2} - x_3^2 - (\frac{D^2}{2} + Dx_3)\right]\right] \\
&= \frac{J_c}{2D}\left[\dot{B}_e\left(D^2 + x_3^2\right) + \dot{B}_i\left(2Dx_3\right)\right]
\end{aligned} \tag{3.2.19}$$

Including the definition of x_3, B_i B_P in (3.2.19) it is possible to obtain:

$$P = \frac{B_p^2}{2\mu_0}\left(\frac{\dot{B}_e}{B_p} + \frac{\dot{B}_e}{B_p}\left(\frac{\dot{I}}{I_c}\right)^2 + 2\frac{I}{I_c}\frac{\dot{B}_i}{B_p}\right) \tag{3.2.20}$$

Drawing upon the preceding discussion, it is possible to derive the formulae for the instantaneous losses under conditions of negative ramp rates for both the transport current and external magnetic field. These formulae are exact replicas of the one in (2.2.34) with the sole modification of a sign change. A compact formulation for the first magnetization can therefore be expressed as in (3.2.21).

$$P = sgn(\dot{I})\frac{B_p^2}{2\mu_0}\begin{cases} K_1 & \text{if} \quad 0 \leq sgn(\dot{I})B_e < sgn(\dot{I})B_i \\ K_2 & \text{if} \quad sgn(\dot{I})B_i \leq sgn(\dot{I})B_e < B_p \\ K_3 & \text{if} \quad sgn(\dot{I})B_e \geq B_p \end{cases} \tag{3.2.21}$$

$$K_1 = \frac{\dot{B}_e B_e^2}{B_p^3} + \frac{\dot{B}_e}{B_p}\left[2\frac{B_e}{B_p}\frac{I}{I_c} - \left(\frac{B_e}{B_p}\right)^2\right] + \frac{\dot{I}}{I_c}\left[\left(\frac{B_e}{B_p}\right)^2 + \left(\frac{I}{I_c}\right)^2\right] \tag{3.2.22}$$

$$K_2 = \frac{\dot{B}_e B_e^2}{B_p^3} + \left(\frac{I}{I_c}\right)^2\frac{\dot{B}_e}{B_p} + 2\frac{B_e}{B_p}\frac{I\dot{I}}{I_c^2} \tag{3.2.23}$$

$$K_3 = \frac{\dot{B}_e}{B_p} + 2\frac{I\dot{I}}{I_c^2} + \frac{\dot{B}_e}{B_p}\left(\frac{I}{I_c}\right)^2 \tag{3.2.24}$$

In the compact and extended version of the Kajikawa formulae, the function $sgn(\dot{I})$ was used. This function's only scope is to correct the application conditions and the overall sign of the resulting losses, detecting if the magnetization is a positive or negative one. In case the transport current is null, (3.2.21), are still applicable but $sgn(\dot{I})$ must be changed with $sgn(\dot{B}_e)$. Equation (3.2.21) holds only for the first magnetization. After that, the newly developed formulae must be utilized.

The *magnetic field of electric penetration*,B^*, will now be defined it represents the the value that B_e must reach after the first magnetization for the electric field to fully penetrate the slab. The penetration of the electric field is not monotonous: when B_e reaches B^* there is a jump in the magnetic field profile inside the slab, and E abruptly fills the slab. An example of a typical field profile inside the slab is shown in Fig. 3.2.6. When B_e is in phase with B_i, it is possible to obtain B^* from geometrical considerations on the magnetic field profile inside the slab. To derive the expression of B^*, the following relation between B^* and B_i^* (value reached by the self-field when $B_e = B^*$), is applied:

$$B_i^* = B^*\frac{B_{im}}{B_{em}}, \tag{3.2.25}$$

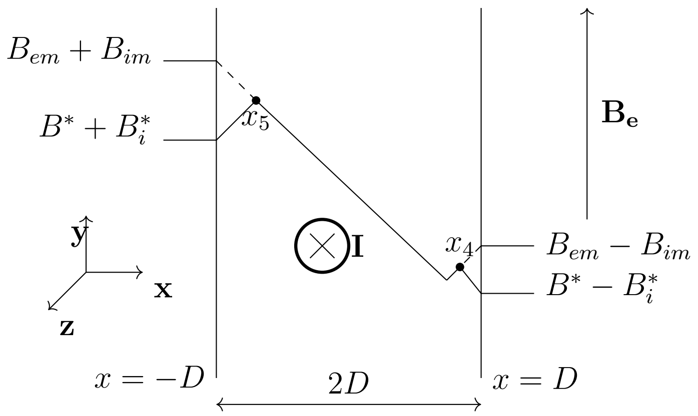

Figure 3.2.5: Sketch of the magnetic field profile inside the slab after the external magnetic field starts decreasing after reaching its maximum value B_{em}, (after a previous ramp-up in the case of $B_e > B_i$).

B_{em} and B_{im} represent the peak values of the external magnetic field and self-field, respectively. Due to the assumption of the critical state model, the slope of the magnetic field profile inside the slab, $\tan(\alpha)$, is fixed at $\mu_0 J_c$. The following system can thus be written:

$$\begin{cases} \tan(\alpha) = \mu_0 J_c \\ \tan(\alpha) = \frac{(B_{em}+B_{im})-(B^*-B_i^*)}{2D} \end{cases} \tag{3.2.26}$$

By combining (3.2.25) and (3.2.26) the expression of B^* is obtained as:

$$B^* = B_{em}\left(\frac{B_{em}+B_{im}-2B_p}{B_{em}-B_{im}}\right) \tag{3.2.27}$$

During the ramp down from the maximum values reached in the first magnetization, the field profile inside the slab is reported in (3.2.28). T' is the instant at which the first magnetization ends. It coincides with the start of the ramp down.

$$B(x,t) = \begin{cases} sign(B_e-B_i)[|B_e-B_i|+\mu_0 J_c(D-x)] & \text{with} \quad x_4 \leq x \leq D \\ B(x,t=T') & \text{with} \quad x_5 < x < x_4 \\ B_e+B_i+\mu_0 J_c(D+x) & \text{with} \quad -D \leq x \leq x_5 \end{cases} \tag{3.2.28}$$

The first equation of (3.2.28) can also be written as :

$$B(x,t) = B_e - B_i + \frac{\mu_0 J_c(D-x)}{sign(B_e-B_i)} \quad \text{with} \quad x_4 \leq x \leq D \tag{3.2.29}$$

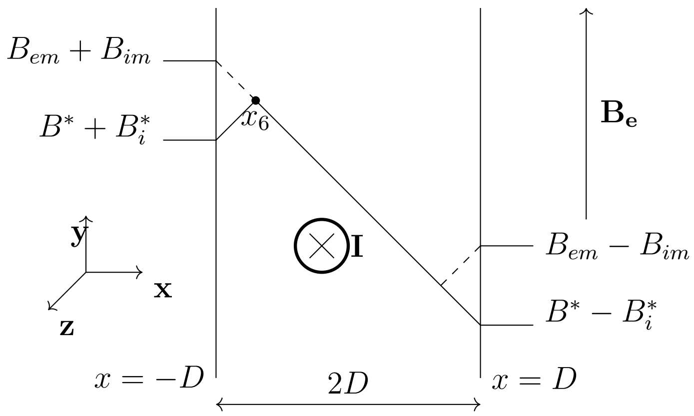

Figure 3.2.6: Sketch of the magnetic field profile inside the slab when the external magnetic field reaches B^*, after a previous ramp-up in the case of $B_e > B_i$.

The second condition in (3.2.28) is the initial condition of the ramp down, the field profile at the end of the previous cycle (first magnetization). As previously done, the term $sign(B_e - B_i)$ is necessary to consider the possibility that $B_e < B_i$, which implies that the field profile is reversed. To derive the definitions of x_4 and x_5 (see Fig. 3.2.5) it is necessary to impose that the magnetic field evaluated by (3.2.28) is equal to that obtained at the end of the first magnetization (so when $B_e = B_{em}$ and $B_i = B_{im}$). The first equation in 3.2.7 and 3.2.28 evaluated in $x = x_4$ must be equal. The same is done for the third equation in 3.2.7 and 3.2.28 at $x = x_5$. Obtaining:

$$x_4 = \frac{D}{2B_p}\left(2(B_{im} - B_{em} + B_e - B_i)\frac{sign(B_e - B_i)sign(B_{em} - B_{im})}{sign(B_e - B_i) + sign(B_{em} - B_{im})} + 2B_p\right) \tag{3.2.30}$$

$$x_5 = D\frac{B_{em} + B_{im} - B_e - B_i - 2B_p}{2B_p} \tag{3.2.31}$$

The intersection point x_4 exists only as long as $B_e > B^*$. When B_e reaches B^*, x_4 collapse into x_5, both becoming x_6 (see Fig. 3.2.6). So (3.2.30) can be rewritten as (3.2.32) and x_6 is defined as equal to x_5.

$$x_4 = D\frac{B_{im} - B_{em} + B_e - B_i + 2B_p}{2B_p} \tag{3.2.32}$$

As long as the external magnetic field is higher than the magnetic field of electric penetration the region comprised between x_4 and x_5 is free of electric field, due to the magnetic field profile inside the slab not changing over time. This means that the region of the slab comprised between x_4 and x_5 is not contributing to the power dissipation. The expressions of the field profiles are provided in (3.2.44), (3.2.45),(3.2.46) and (3.2.47).

$$B_e > B^* \quad E(x,t) = \begin{cases} \frac{\partial(B_e - Bi)}{\partial t}(x - x_4) & \text{with} \quad x_4 \leq x \leq D \\ 0 & \text{with} \quad x_5 < x < x_4 \\ \frac{\partial(B_e + Bi)}{\partial t}(x - x_5) & \text{with} \quad -D \leq x \leq x_5 \end{cases} \tag{3.2.33}$$

$$B_e > B^* \quad J(x,t) = \begin{cases} -sign(B_e - B_i)J_c & \text{with} \quad x_4 \leq x \leq D \\ J(x, t = T') & \text{with} \quad x_5 < x < x_4 \\ J_c & \text{with} \quad -D \leq x \leq x_5 \end{cases} \tag{3.2.34}$$

$$B_e < B^* \quad E(x,t) = \begin{cases} \frac{\partial(B_e - Bi)}{\partial t}(x - x_6) & \text{with} \quad x_6 \leq x \leq D \\ \frac{\partial(B_e + Bi)}{\partial t}(x - x_6) & \text{with} \quad -D \leq x \leq x_6 \end{cases} \tag{3.2.35}$$

$$B_e < B^* \quad J(x,t) = \begin{cases} -sign(B_e - B_i)J_c & \text{with} \quad x_6 \leq x \leq D \\ J_c & \text{with} \quad -D \leq x \leq x_6 \end{cases} \tag{3.2.36}$$

By using the equation of the field profiles in (3.2.1) we can reach a set of formulae that describe the instantaneous losses in an infinite slab after the first magnetization, during a ramp down of the transport current and magnetic field (3.2.37). It is important to note that no assumptions have been made about the shape of the wave of I and B_e, these formulae are completely generic and can be applied to whichever waveform of I and B_e.

$$P = -\frac{1}{16\mu_0 B_p} \begin{cases} A_{1d} & \text{if} \quad B_{em} < B_{im} \\ A_{2d} & \text{if} \quad B_e \geq B^* \\ A_{3d} & \text{if} \quad B_e < B^* \end{cases} \tag{3.2.37}$$

Where

$$\begin{aligned} A_{1d} = & \left(\dot{B}_e + \dot{B}_i\right)\left(B_{em} + B_{im} - (B_e + B_i)\right)^2 \\ & - \left(\dot{B}_e - \dot{B}_i\right)\left(-(B_{im} - B_{em}) - B_e + B_i\right)^2 \end{aligned} \tag{3.2.38}$$

$$\begin{aligned} A_{2d} &= \left(\dot{B}_e + \dot{B}_i\right)\left(B_{em} + B_{im} - (B_e + B_i)\right)^2 \\ &+ \left(\dot{B}_e - \dot{B}_i\right)\left(-(B_{im} - B_{em}) - B_e + B_i\right)^2 \end{aligned} \tag{3.2.39}$$

$$\begin{aligned} A_{3d} = 4{B_p}^2 \Bigg[&\left(\dot{B}_e + \dot{B}_i\right)\left(1 - \frac{B_i}{B_p}\right)^2 \\ &+ \left(\dot{B}_e - \dot{B}_i\right)\left(1 + \frac{B_i}{B_p}\right)^2 \Bigg] \end{aligned} \tag{3.2.40}$$

The same procedure employed insofar can be used to obtain the analytical expression for the instantaneous power losses due to a ramp-up of the transport current (and magnetic field) after the first magnetization. As already shown, what matters is the knowledge of the field profiles inside the slab. Assuming the ramp up starts after the end of the previous ramp down, the magnetic field profile is shown in Fig. 3.2.7. The ramp-down ended reaching the values of $-B_{em}$ and $-B_{im}$.

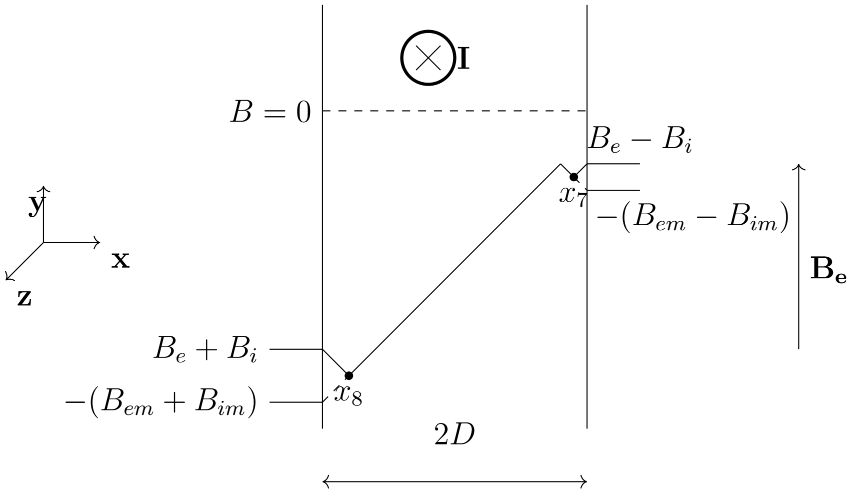

Figure 3.2.7: Graphic representation of the field profile inside the slab, during the first instant of a ramp up right after a ramp down (case $B_e > B_i$).

When B_e reaches $-B^*$ the intersection point x_7 collapses into x_8. The new point is therefore called x_9, causing the abrupt penetration of the electric field in the whole slab. In (3.2.41), T'' is the instant of time at which the ramp-down stops.

$$B(x,t) = \begin{cases} sign(B_e - B_i)[|B_e - B_i| + \mu_0 J_c(D-x)] & \text{with} \quad x_7 \leq x \leq D \\ B(x, t = T'') & \text{with} \quad x_8 < x < x_7 \\ B_e + B_i - \mu_0 J_c(D+x) & \text{with} \quad \text{-}D \leq x \leq x_8 \end{cases} \tag{3.2.41}$$

$$x_7 = D\frac{B_{im} - B_{em} - B_e + B_i + 2B_p}{2B_p} \tag{3.2.42}$$

$$x_8 = D\frac{B_{im} + B_{em} + B_e + B_i - 2B_p}{2B_p} \tag{3.2.43}$$

$$B_e < -B^* \quad E(x,t) = \begin{cases} \frac{\partial(B_e - Bi)}{\partial t}(x - x_7) & \text{with} \quad x_7 \leq x \leq D \\ 0 & \text{with} \quad x_8 < x < x_7 \\ \frac{\partial(B_e + Bi)}{\partial t}(x - x_8) & \text{with} \quad -D \leq x \leq x_8 \end{cases} \tag{3.2.44}$$

$$B_e < -B^* \quad J(x,t) = \begin{cases} -sign(B_e - B_i)J_c & \text{with} \quad x_7 \leq x \leq D \\ J(x, t = T'') & \text{with} \quad x_7 < x < x_7 \\ -J_c & \text{with} \quad -D \leq x \leq x_8 \end{cases} \tag{3.2.45}$$

$$B_e > -B^* \quad E(x,t) = \begin{cases} \frac{\partial(B_e - Bi)}{\partial t}(x - x_9) & \text{with} \quad x_9 \leq x \leq D \\ \frac{\partial(B_e + Bi)}{\partial t}(x - x_9) & \text{with} \quad -D \leq x \leq x_6 \end{cases} \tag{3.2.46}$$

$$B_e > -B^* \quad J(x,t) = \begin{cases} -sign(B_e - B_i)J_c & \text{with} \quad x_9 \leq x \leq D \\ -J_c & \text{with} \quad -D \leq x \leq x_9 \end{cases} \tag{3.2.47}$$

The analytical formulae for the ramp-up are expressed in (3.2.48).

$$P = \frac{1}{16\mu_0 B_p} \begin{cases} A_{1u} & \text{if} \quad B_{em} < B_{im} \\ A_{2u} & \text{if} \quad B_e \leq -B^* \\ A_{3u} & \text{if} \quad B_e > -B^* \end{cases} \tag{3.2.48}$$

Where

$$\begin{aligned} A_{1u} = &\left(\dot{B}_e + \dot{B}_i\right)\left(B_{em} + B_{im} + (B_e + B_i)\right)^2 \\ &- \left(\dot{B}_e - \dot{B}_i\right)\left((B_{im} - B_{em}) - B_e + B_i\right)^2 \end{aligned} \tag{3.2.49}$$

$$\begin{aligned} A_{2u} = &\left(\dot{B}_e + \dot{B}_i\right)\left(B_{em} + B_{im} + (B_e + B_i)\right)^2 \\ &+ \left(\dot{B}_e - \dot{B}_i\right)\left((B_{im} - B_{em}) - B_e + B_i\right)^2 \end{aligned} \tag{3.2.50}$$

$$\begin{aligned} A_{2u} = 4{B_p}^2 \Bigg[&\left(\dot{B}_e + \dot{B}_i\right)\left(1 + \frac{B_i}{B_p}\right)^2 \\ &+ \left(\dot{B}_e - \dot{B}_i\right)\left(1 - \frac{B_i}{B_p}\right)^2 \Bigg] \end{aligned} \tag{3.2.51}$$

The formulae for the ramp-down and ramp-up after the first magnetization (3.2.37) and (3.2.48) can be combined in a compact form as shown in [19]. The final formulation can be written as:

$$P = \frac{\operatorname{sgn}(\dot{I})}{16\mu_0 B_p} \begin{cases} A_1 & \text{if} \quad B_{em} < B_{im} \\ A_2 & \text{if} \quad \operatorname{sgn}(\dot{I}) B_e \leq -B^* \\ A_3 & \text{if} \quad \operatorname{sgn}(\dot{I}) B_e > -B^* \end{cases} \tag{3.2.52}$$

Where:

$$\begin{aligned} A_1 = &\left(\dot{B}_e + \dot{B}_i\right)\left(B_{em} + B_{im} + \operatorname{sgn}(\dot{I})(B_e + B_i)\right)^2 \\ &- \left(\dot{B}_e - \dot{B}_i\right)\left(\operatorname{sgn}(\dot{I})(B_{im} - B_{em}) - B_e + B_i\right)^2 \end{aligned} \tag{3.2.53}$$

$$\begin{aligned} A_2 = &\left(\dot{B}_e + \dot{B}_i\right)\left(B_{em} + B_{im} + \operatorname{sgn}(\dot{I})(B_e + B_i)\right)^2 \\ &+ \left(\dot{B}_e - \dot{B}_i\right)\left(\operatorname{sgn}(\dot{I})(B_{im} - B_{em}) - B_e + B_i\right)^2 \end{aligned} \tag{3.2.54}$$

$$\begin{aligned} A_3 = 4{B_p}^2 \Bigg[&\left(\dot{B}_e + \dot{B}_i\right)\left(1 + \operatorname{sgn}(\dot{I})\frac{B_i}{B_p}\right)^2 \\ &+ \left(\dot{B}_e - \dot{B}_i\right)\left(1 - \operatorname{sgn}(\dot{I})\frac{B_i}{B_p}\right)^2 \Bigg] \end{aligned} \tag{3.2.55}$$

As already mentioned for the formulae in (3.2.21), in (3.2.52) the term $sgn(\dot{I})$ can be exchanged with $sgn(\dot{B}_e)$ in case the transport current is null.

3.2.2 Validation trough FEM models comparison

The formulae in (3.2.52) together with (3.2.21) can be applied to compute the losses in a slab for any cycle of transport current and magnetic field, as long as the two are in phase with each other. The formulae can be applied to the study of tapes and stacks of tapes, to compute the losses due to either an orthogonal magnetic field or a parallel one [19,91,92]. The direction of the field is determined with respect to the wide surfaces of the tapes. Examples of instantaneous losses in time for a sinusoidal transport current and external orthogonal magnetic field, at 50 Hz, are shown from Fig. 3.2.8 to Fig. 3.2.13. The losses presented refer to an infinite slab which can then be assumed as a representation of a stack of an extremely high number of tapes. The infinite stack's tape main data are reported in Table 3.2.1. These cases are used to illustrate the instantaneous loss behavior and the impact of the transport current on the losses. Due to their reliance on simplified slab geometries, these formulae may introduce inaccuracies when applied to geometries significantly different from slabs (even the 40-tape stack presented). An analysis of the inaccuracies introduced is shown later in this section.

Table 3.2.1: Tape Parameters

Tape thickness (t)	150 μm	*Tape width* ($w = 2a$)	4 mm
Superconductor thickness (d)	1 μm	*critical current density* (J_c)	10^{10} A/m^2

It can be seen from Fig. 3.2.8 to Fig. 3.2.13 that the transport current has a role in enhancing the peak value of the instantaneous losses. The impact of the transport current is more noticeable in the low-field region where the main contribution to the losses is due to the transport current itself. In the case of a low external magnetic field (Figs. 3.2.8 to 3.2.10) the peak of the instantaneous losses amount to 1.8 kW/m^{-3} without any transport current. However, when the transport current reaches half of its critical value, the losses peak jumps to 254 kW/m^3. This trend continues as the current increases further. At 70% of the critical current, the losses peak reaches a substantial 660 kW/m^3. The presence of a transport current causes an increase of the losses peak, in the cases proposed, of 14000% and 36000% respectively. A steady increase of the peak value of the losses due to the transport current is present also in the high-field case (Figs. 3.2.11 to 3.2.13). The effect of the transport current is less pronounced, causing an increase of only 67% and 117% respectively compared to the case without current applied (peak power loss 2.4 MW/m^3).

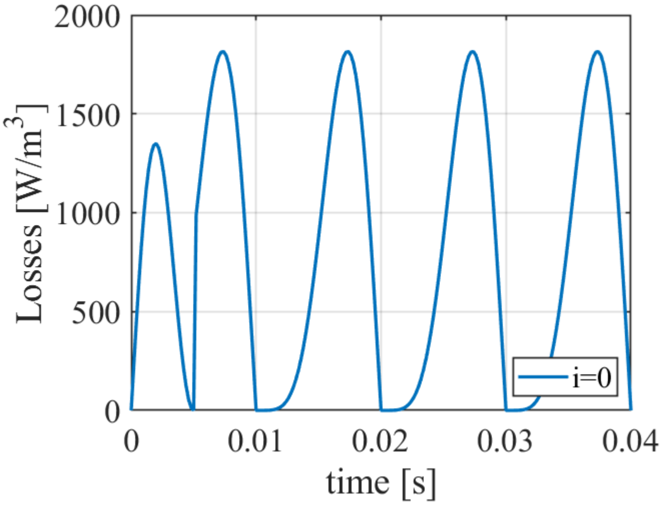

Figure 3.2.8: *Instantaneous power losses in a superconducting infinite slab subjected to a sinusoidal, magnetic field orthogonal to the wide surface of amplitude* $0.1B_p$ *and no transport current .*

The definitions in (3.2.56) are needed to understand how to define the penetration field and scale the losses when using (3.2.52). If the external field is orthogonal to the wide surface of the tape/ stack of tapes under study, then the finite dimension of the slab (2D) is the width of the tape. If the external field is parallel to the wide surface the finite dimension is the thickness of the tape.

$$\begin{gathered} B_e = B_{\|} \quad D = d/2 \quad Q_{\|} = P \cdot V \\ B_e = B_{\perp} \quad D = a \quad \lambda = d/t \quad Q_{\perp} = P \cdot V/\lambda \end{gathered} \tag{3.2.56}$$

$Q_{\perp}$ are the losses to the ortogonal field, $Q_{\|}$ those due to the parallel field, P the losses evaluated by (3.2.52) and V is the volume of superconducting material. In the case of a field with a generic orientation it was demonstrated in [92] that the losses can be treated as shown in (3.2.57) by decomposing the magnetic field.

$$Q \approx Q_{\perp} + Q_{\|} \tag{3.2.57}$$

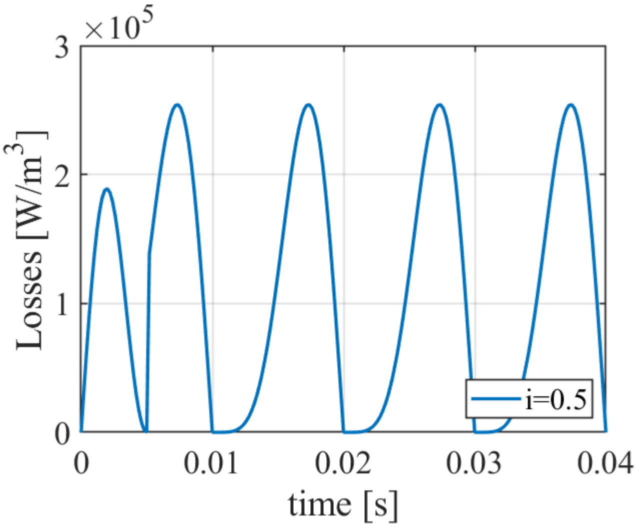

Figure 3.2.9: *Instantaneous power losses in a superconducting infinite slab subjected to a sinusoidal magnetic field orthogonal to the wide surface of amplitude* $0.1B_p$ *and transport current of amplitude* $0.5I_c$.

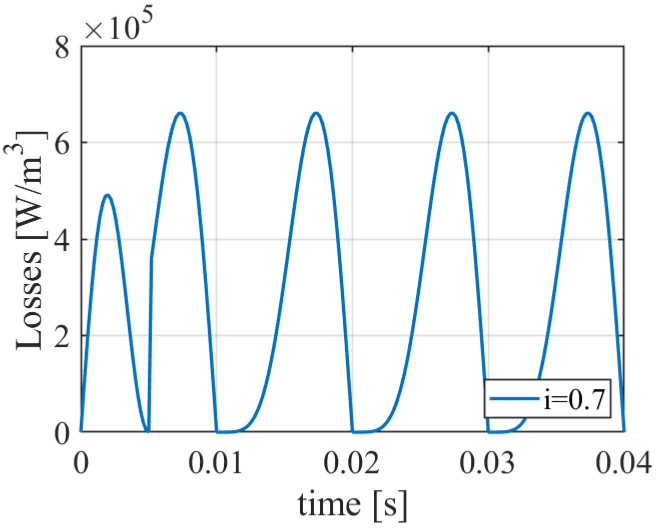

Figure 3.2.10: *Instantaneous power losses in a superconducting infinite slab subjected to a sinusoidal, magnetic field orthogonal to the wide surface of amplitude* $0.1B_p$ *and transport current of amplitude* $0.7I_c$.

The developed formulae were applied to analyze a simplified case study, in which a superconducting slab is subjected to an external magnetic field applied orthogonal to its wide face. The superconducting slab results from a homogenization of a stack composed of 40 tapes. Each tape is 4 mm wide and 100 μm thick;

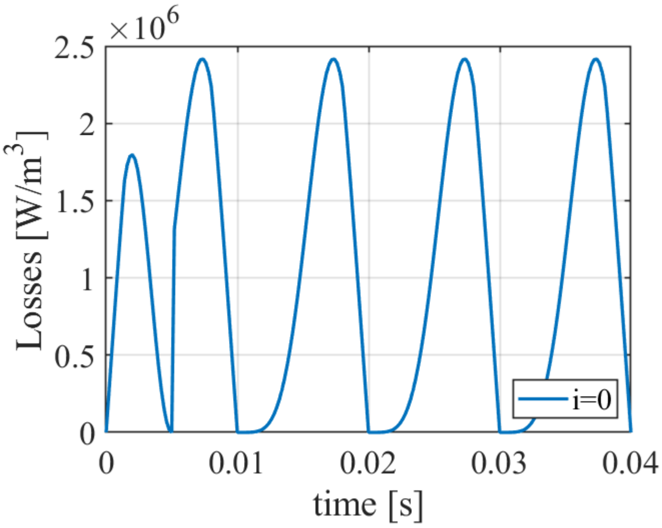

Figure 3.2.11: *Instantaneous power losses in a superconducting infinite slab subjected to a sinusoidal, magnetic field orthogonal to the wide surface of amplitude* $1.1 B_p$ *and no transport current.*

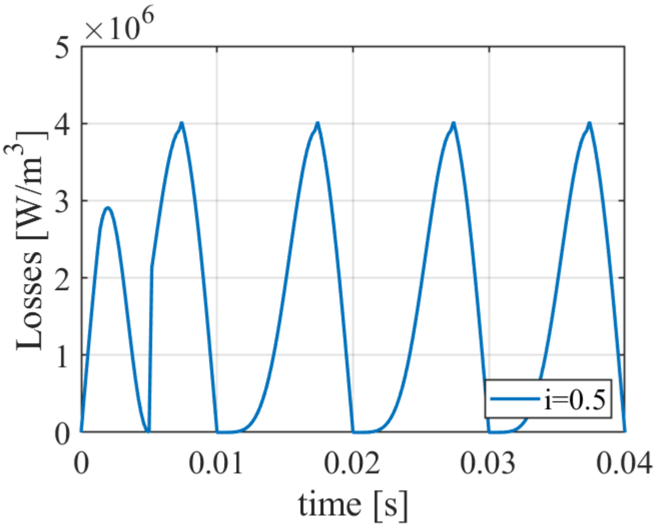

Figure 3.2.12: *Instantaneous power losses in a superconducting infinite slab subjected to a sinusoidal, magnetic field orthogonal to the wide surface of amplitude* $1.1 B_p$ *and transport current of amplitude* $0.5 I_c$.

the engineering critical current density ($J_{c,e}$) is set to 2.2×10^9 Am^{-2}. The field varies sinusoidally in time at a frequency of 50 Hz, in phase with the transport current. Homogenization is the key to treating stacks of tapes as slabs (although non-infinite), the homogenization performed is based on the one described in sec-

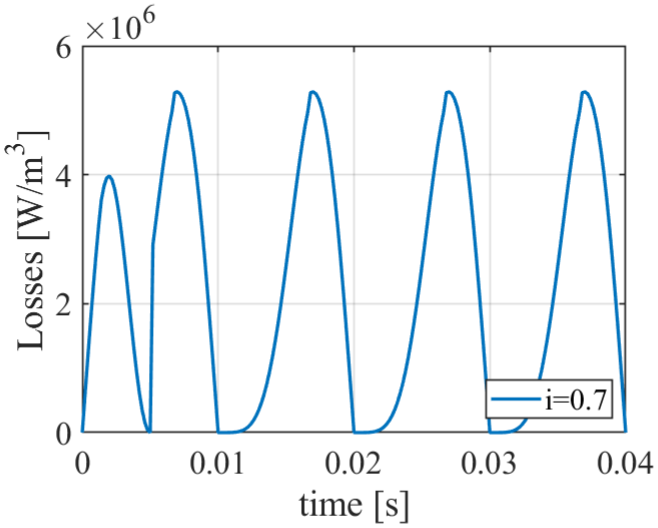

Figure 3.2.13: *Instantaneous power losses in a superconducting infinite slab subjected to a sinusoidal, magnetic field orthogonal to the wide surface of amplitude* $1.1B_p$ *and transport current of amplitude* $0.7I_c$.

tion 2.5.1. The current density of the superconductor is spread along the whole stack, for the case of a single tape it would mean that $J_0 = J_c\lambda$, where J_0 is the homogenized current density.

The results of the analytical formulae were compared in two case studies with those of a 1D FEM model implemented in COMSOL Multiphysics® [124] (see Fig. 3.2.14). The 1D model solves the following magnetic field diffusion equation:

$$\begin{cases} \dfrac{\partial B(x,t)}{\partial t} - \dfrac{\partial}{\partial x}\left(\dfrac{\rho}{\mu_0}\dfrac{\partial B(x,t)}{\partial x}\right) = 0 \\ B(x,t) = (\mathrm{sgn}(x)B_{im} + B_{em})\sin(t) \quad ; \quad |x| = D \end{cases} \tag{3.2.58}$$

The second equation in (3.2.58) represents the Dirichlet boundary conditions applied, t is time, x the spatial coordinate ($|x| \leq D$), and ρ the resistivity of the superconducting slab. $B(x,t)$ is the field profile along the x direction at time t. Two case studies were analyzed:

a) the amplitude of the external field is 1 T and the ratio between the amplitude of the transport current and the critical current ($i = I_m/I_c$) is set to 0.2.

b) the amplitude of the external field is 1 T and i is set to 0.4.

The maximum difference between the 1D FEM model and the analytical formulae is respectively 34 W/m for the first case study and 118 W/m for the second one. The average relative error between the results of the two formulations is 1%. The losses in $J/(m^3 cycle)$ can be obtained by integrating the power values reported in Fig. 3.2.14, and dividing by the cross-section area of the stack. The losses estimated by the analytical formulae are 3.5×10^5 J/m^3 in case *a)* and 1.2×10^6 J/m^3 in case *b)*. The values of the losses per cycle have the same order of magnitude ($1MJ/(m^3 cycle)$) as those experimentally measured on similar stacked cables [142], and also on different geometries (CORC) [143]. As can be seen in Fig. 3.2.14, the impact of the transport current on the magnetization losses is not negligible.

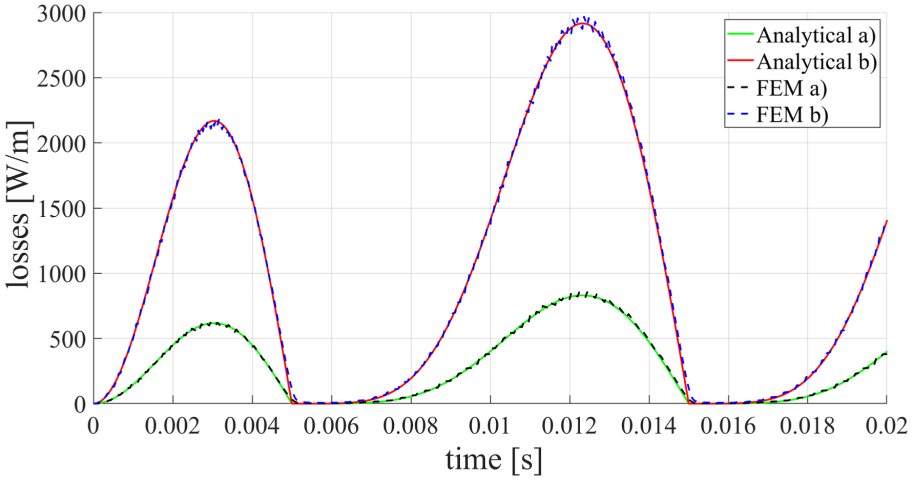

Figure 3.2.14: *Comparison between the results of the analytical formulae in* (3.2.52) *and of the 1D FEM model* [19]. The two cases presented here refer to a sinusoidal transport current in phase with an orthogonal magnetic field applied, to a 40-tape stack. The amplitude of the magnetic field in both cases a) and b) is set to 1 T while the amplitude of the transport current is set in case a) to $0.2I_c$ and in case b) to $0.4I_c$.

The comparison between the analytical formulae and the 1D fem model is extremely good, and this is to be expected. FEM models operating in 1D implicitly make the same assumptions as a slab model. A more representative comparison is shown in Fig. 3.2.15, which shows the behavior of the AC losses predicted by three different analytical formulations (the Brandt formula, the slab formula, and the presented formulation), and a 2D FEM model based on the H-formulation. The models were applied to study a 100-tape stack subjected to an orthogonal external magnetic field and different values of transport current, both sinusoidal at 50 Hz and in phase with each other. The main parameters of the stack are reported in Table 3.2.2. The Brandt formula holds only for a single strip of superconductor without transport current, and is, therefore, unable to account for the shielding effect of the stack even in the case of no transport current (i = 0). The shielding effect determines a reduction of the losses in a stack of tapes due to magnetic shielding of the tapes at the edges with respect to those at the center of the stack. This situation is similar to the behavior of the shielding currents in a single tape tape where the center of the tape carries a lower current than the edges. This effect is shown via simulation with the 2D FEM in Fig. 3.2.16. The slab formula can take into account the shielding effect of the tapes but only hold with no transport current. The new formulation developed can take into account the shielding effect of the tapes of the stack and holds even in the presence of transport current (i > 0). It is worth noting that without transport current the curves of the AC losses for the new formulation and the slab formulae are perfectly overlapped.

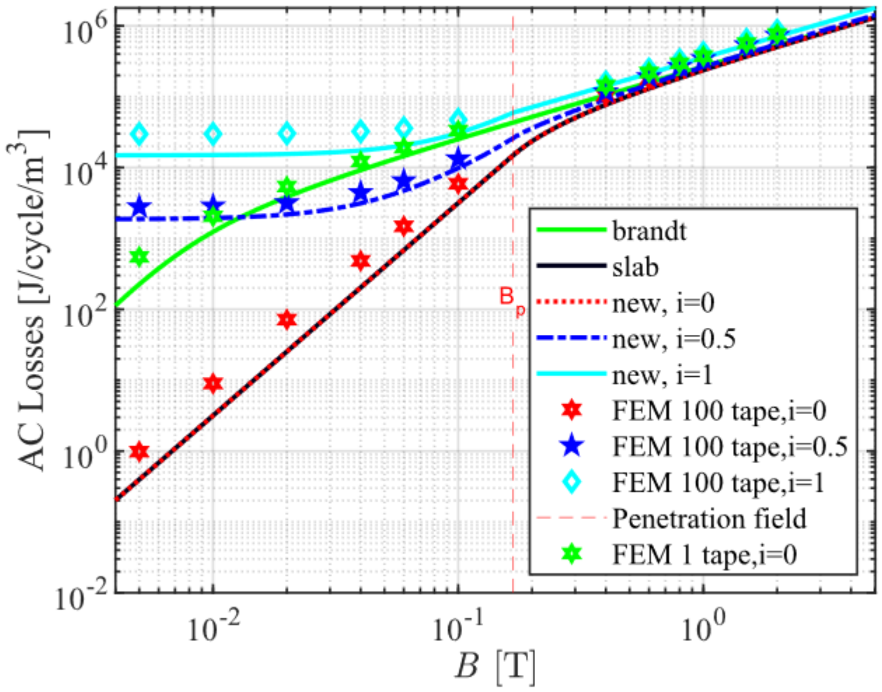

Figure 3.2.15: *AC losses in a 100-tape stack subjected to an orthogonal external magnetic field and different values of transport current, both sinusoidal at 50 Hz. Labeled as "new" the results obtained from the proposed formulae.*

The 2D FEM model is also based on a homogenization, which was necessary to reduce the computation burden and allow the simulation to reach convergence.

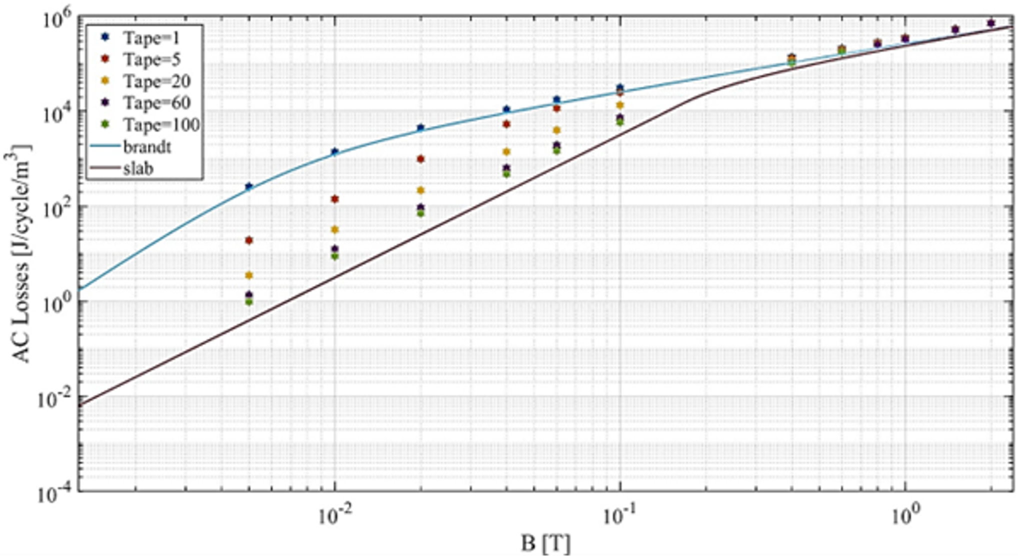

Figure 3.2.16: *AC losses with no transport current as a function of the external field, and of the number of tapes in the stack. The dots represents the results obtained from the 2D FEM model while the lines are the losses predicted by analytical formulae for a thin strip (Brandt) and an infinite slab (Brandt).*

Table 3.2.2: Simulation Parameters 2D FEM comparison

Tape thickness	150 μm	Tape width	4 mm
Number of tapes	100	Superconductor thickness	1 μm
J_c	$1 \times 10^{10} A/m^2$	Homogenized J_c	$6.67 \times 10^7 A/m^2$

Two different homogenizations were applied one after the other. At first, only the superconducting layers of the stack were modeled, then each superconducting layer was homogenized with the tape to which it belongs. Finally, all the homogenized tapes were further homogenized between themselves. The final result is a slab with a width equal to the width of the tapes, and a thickness equal to the sum of the thickness of all the tapes. Simulations were performed to determine the error committed between the results of the model based on the final homogenization and the initial one. The percentage error ranges from 5% at low values of the external field and drops to 0.1% for $B_e > B_p$. Fig. 3.2.15 stress once again the importance of including the effect of the transport current in the AC loss computation. At lower values of the magnetic field, the losses due to the transport current are highly relevant. For high values of the magnetic field, the contribution of the transport current is less dominant but still present, and the analytical formulae predict a higher value of loss when the transport current is present in the slab geometry than in the single tapes (Brandt).

Discrepancies between the analytic and the 2D FEM results are due to the aspect ratio of the stack not being representative of an infinite slab. For a 100-tape stack, with the parameters in Table 3.2.2, the aspect ratio is only 3.75. Despite that, the behavior of the losses is correctly represented by the formulae developed here (3.2.52).

3.3 Application to SC-TSTC

This study only focuses on the computation of the hysteresis losses in HTS conductors realized with the twisted stacked CICC configuration. The losses due to coupling currents between the different stacks are not computed here. It should be recalled that recent designs allow reducing these losses by a factor of 10 thanks to a sectorized core including inserts of high-resistivity material [144]. Thus the main contribution to the losses of a conductor are the hysteresis losses. A framework for the qualitative assessment of AC losses in SC-TSTC (the one in Fig. 3.1.1 was studied) via analytical formulation was developed and applied for the study of an HTS insert in the magnet configuration of the central solenoid of DEMO. Currently, the framework is comprised of:

- A software for the computation of the magnetic field created by the magnet system under investigation
- A software for the analysis of the losses through the analytical formulae developed
- A post processor for the display and print of the data

For the tools developed to work some assumptions are needed:

- Axis symmetry: the external magnetic field in the magnet configuration studied is axisymmetric, which allows treating the electromagnetic problem as a 2D one, greatly reducing the computational burden.
- Magnetic field homogenization: all the stacks of the same cable are considered subjected to the same external magnetic field, computed at the center of the cable (z = r = 0, in Fig. 3.3.1).

- Substitutive stacks: one twist pitch of the cable of length L_p, is subdivided into a given number of elements N along the twist pitch itself. The losses are then calculated over straight pieces of stacks having different angular positions along the twist pitch. The straight stack composed of N elements, each with length l $= L_p/N$, is called a substitutive stack, see Fig. 3.3.1. The use of the substitutive stacks makes it possible to treat the twisting of the conductor with the formulae presented here;

- Magnetic coupling: the magnetic coupling between different stacks is not taken into account.

The computation of the magnetic field is performed through a 2D axisymmetric FEM model implemented In FORTRAN [145]. The software for the evaluation of the magnetization losses was developed in MATLAB [146], and it is available as a stand-alone program working in any Windows environment. The framework developed is extremely flexible and can be adapted to various analytical formulations.

In Fig. 3.3.1 the angular positions of the N elements are presented in the same plane, even though they are located on different rz planes at a distance l from each other. These stacks belong to the same *substitutive stack* (see Fig. 3.3.1). $\mathbf{B_e}$ is the external magnetic field, which is calculated at the center of the cable, and $\angle\mathbf{B_e}$ is the angle between $\mathbf{B_e}$ and the r-axis. n is the unit vector orthogonal to the tape surface, and α is the angle between n and the r-axis. $B_\perp$ and $B_\parallel$ are the orthogonal and parallel components of the magnetic field with respect to the tape.

3.3.1 Input data

The required inputs for the computation of the magnetization losses are:

1. Evolution in time of the currents in the magnets (input from file)

2. Geometry of the magnets (input from keyboard, position, and number of turns)

3. Coordinates of the field points, i.e. points where the magnetic field is evaluated (in our case the center of the cables

The configuration studied is a combination of the central solenoid (CS) magnets and poloidal field magnets, which are those mainly contributing to the total field in the CS magnets. The Geometry of the magnets is not reported as it is a property of the EUROfusion Consortium and is still under development.

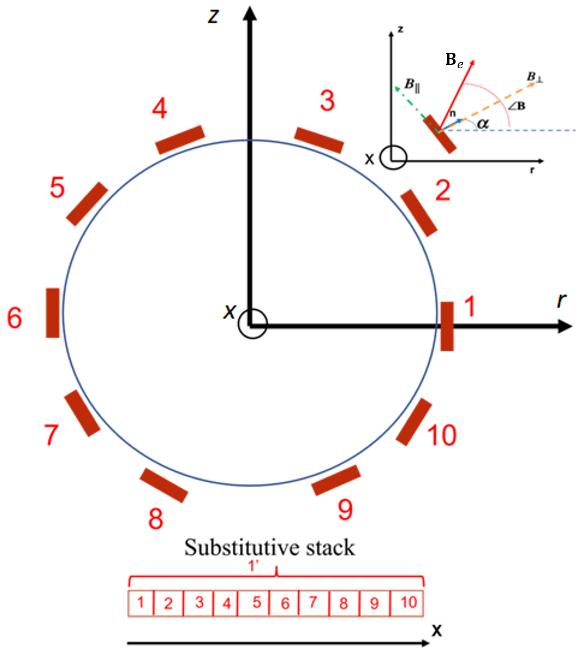

Figure 3.3.1: *Example of a subdivision in 10 elements, of a twisted stack and and resulting substitutive stack.*

3.3.2 Procedure details

Details about the procedure followed in this framework are shown in Fig. 3.3.2, operating with the analytical formulation developed, the losses are those of a slab and are evaluated per unit of volume. The start of the process, for the evaluation of the AC losses within the framework developed, is supplying the input data regarding the geometry and the currents of the magnets together with the coordinates of the field points in which the magnetic field will be evaluated. Then the software will compute the magnetic field generated and the time derivative of both the currents and the magnetic field. It will then start evaluating the losses in each of the N elements composing the substitutive stack representing one twist pitch of the REBCO cable. Once the losses per unit of volume of a slab are evaluated for each longitudinal element of a substitutive stack, these values are multiplied by the volume of the superconductor in each element and then summed up to obtain the losses of a stack. Since by hypothesis, there is no magnetic coupling between the stacks of a cable, the total loss of one twist pitch of the cable is the sum of the losses of the single stacks. The losses of a twist pitch are then multiplied by the number of twist pitches along a turn of the central solenoid and summed to the losses of the other turns to obtain the total losses of the insert. Table 3.3.1 illustrates the parameters of the cable and tapes used in the

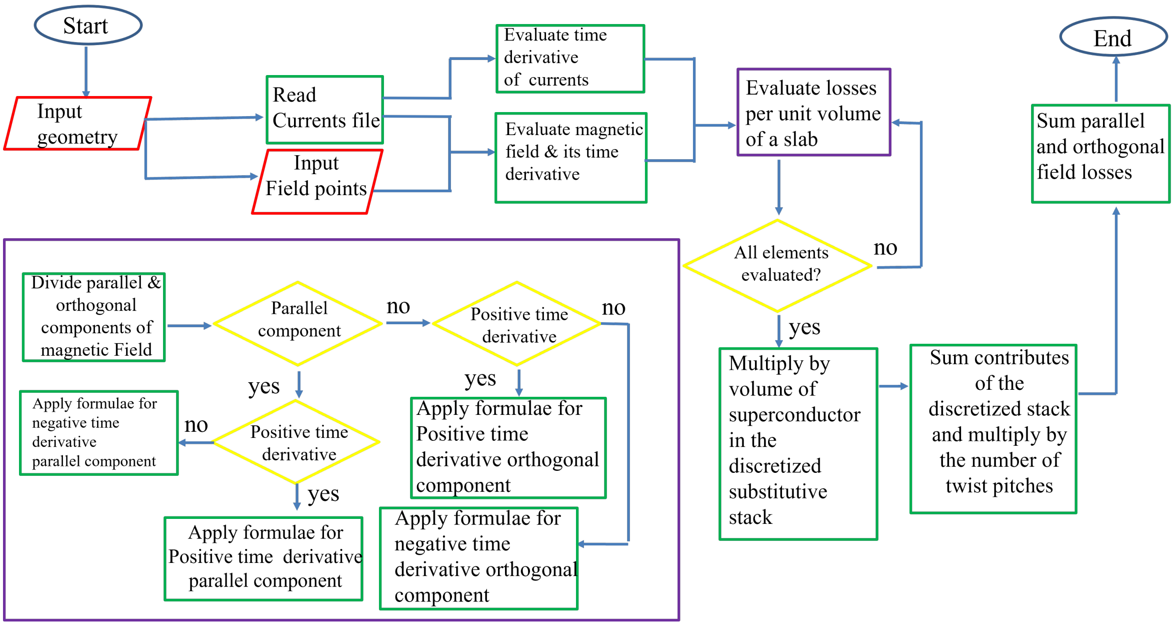

Figure 3.3.2: *Flowchart of the developed procedure, the content of the box in the bottom left is a detailed description of the step "evaluate losses per unit of volume of a slab".*

simulation alongside other parameters such as the operating temperature and the time step. The temperature is considered to be fixed and does not change during the simulation time.

3.3.3 Results

The developed procedure was tested by computing losses in the HTS insert of the DEMO CS for a simplified test-case study. In this analysis, the transport current in all the conductors (so the current in both the central solenoid magnets

Table 3.3.1: Simulation Parameters DEMO insert

Temperature	4.5 K	*Number of turns*	460
Tape thickness (t)	150 μm	*Tape width (2a)*	4 mm
Tapes per stack	30	*Stacks per cable*	10
Cable diameter	33 mm	*Twist pitch*	1 m
Superconductor thickness (d)	2 μm	*Time step*	0.5 s
Inter-distance (g)	148 μm	*Volume element (V)*	2ad/N m^3

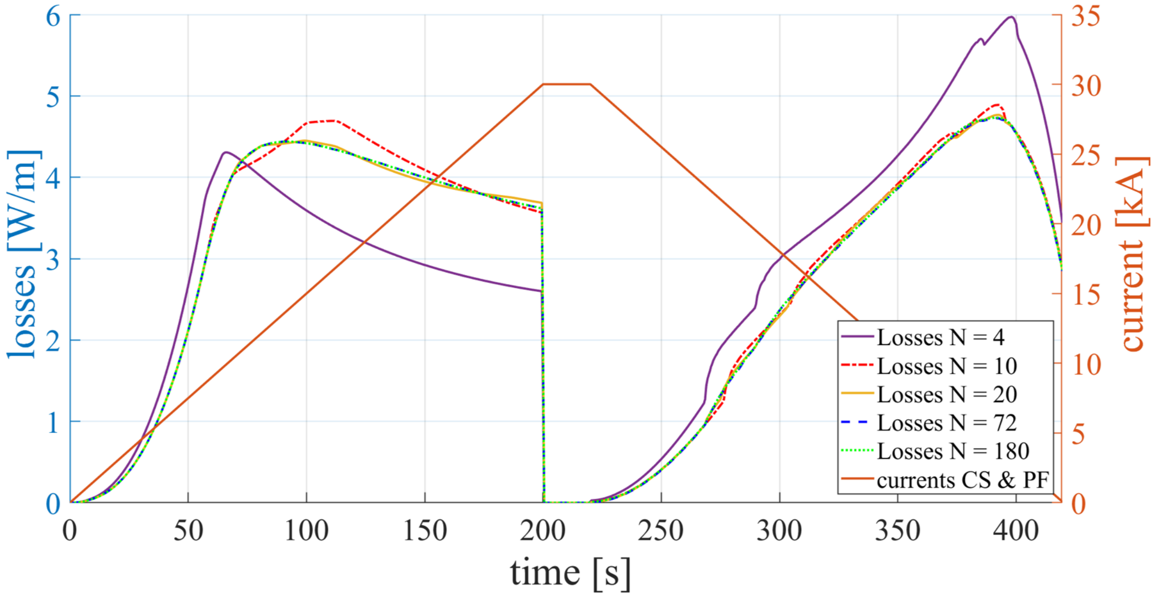

Figure 3.3.3: *Total losses of the REBCO insert in all the CS modules per meter, calculated with different numbers of elements in the substitutive stack* [19].

and poloidal field magnets) follows a trapezoidal cycle with a current ramp-rate of 150 A/s and a flat-top value of 30 KA. The peak magnetic field obtained in this test case is 10 T, with a ramp rate of 50 mT/s. This case study does not follow a real plasma scenario for the DEMO tokamak, in which the transport current is not in phase with the magnetic field and each conductor of the CS and PF may have a different evolution in time of the transport current. The case study investigated was only used to probe the results of the analytical formulation in a simplified plasma scenario, with nominal values of the transport current. The corresponding losses were computed with a different number of elements, changing the discretization of the conductor twist pitch with values of N ranging from 4 to 180. Fig. 3.3.3 shows the total losses in the HTS insert for the different discretizations adopted. Apart from the case with 4 and 10 elements, a good agreement between the curves is found with N greater than 20. As proof of the good quality of the convergence of the results the L2-norm of the difference between the results obtained with N = 180 and all other cases is presented in Table 3.3.2.

Table 3.3.2: L2 norm of results with different number of elements

N=4	N=10	N=20	N=72
4	2.1	0.54	0.13

The L2-norm drops from 14 for N = 4 to 0.13 for N = 72. The discretization with N = 20 represents a reasonable trade-off between accuracy and computation time. The overall CPU time for N = 20 is 45 minutes for the whole computation of both the magnetic field and the magnetization losses, for a 4-core, 3.60 GHz Intel(R) Core(TM) i7-7700 processor. The peak value of the losses amounts to 4.7 W/m, while the total losses per cycle are equal to 6.4 MJ/m [19].

3.4 Extension beyond the "in phase" assumption

Although the presented formulae are valuable, they are constrained by the assumption of in-phase transport current and external magnetic field. In practical applications, this condition is often not satisfied. To address this limitation, we can employ the methodology introduced at the beginning of this Chapter to derive new formulae that hold for not-in-phase current and field configurations. The configuration of the current and field chosen for the application of the new formulae is that proposed in Fig. 3.4.1. The transport current (indicated in Fig. 3.4.1 via the self-field B_i generated, see (3.2.6)) increases from 0 to 0.7 times the critical current I_c in 1.5 seconds, then remains constant for 1 second before decreasing to 0 in the following 1.5 seconds. The external magnetic field increases from 0 to 1.2 times the penetration field B_p in 2 seconds, then remains constant for 0.5 seconds before decreasing to 0 in 1 second and staying at 0 T for the remainder of the simulation. The scenario analyzed is similar in its behavior to one of the proposed plasma cycles of the divertor tokamak test (DTT) facility currently under construction at ENEA [147]. To study this current-field configuration an analytical formula was developed that holds when the external magnetic field is null and the self-field is ramping down [20]. The new formula presented in (3.4.1) has a limited range of applications. However, other formulations can be derived for all the possible combinations of current and field profiles. The purpose of this section is to prove that analytical formulae can still be found and be useful in case studies of technical interest.

$$P = -\frac{\dot{B}_i}{16 B_p \mu_0} \left[(2B_p - B_{i0} - B_i))^2 + (B_{i0} - B_i)^2 \right] \tag{3.4.1}$$

The term B_{i0} is the value of the self-field when B_e becomes zero. The case study in Fig. 3.4.1 was chosen to show all the different loss mechanisms in a slab, and is representative of a real plasma scenario [147].

The condition occurring when B_e reaches zero is not accounted for in (3.2.52). The reason for this is apparent by looking at the magnetic field profile in Fig. 3.4.2. When $t = 3.5$ s, there is a rigid shift down of the magnetic field profile. The

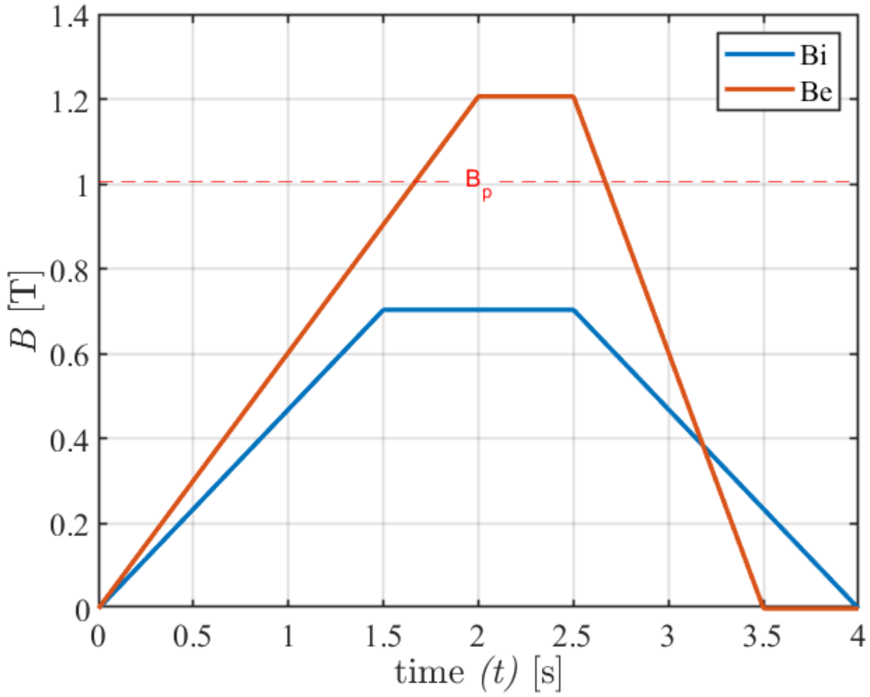

Figure 3.4.1: *Time evolution of the external magnetic field (B_e) and the self-field (B_i), in the studied case* [20].

electric field fills the slab increasing the losses in a similar way as already described during the derivation of (3.2.52), when B_e reaches B^*. therefore, to compute the losses in the last 0.5 s of simulation, (3.4.1) has to be employed.

The parameters of the stack under study, with the new formula, are reported in Table 3.4.1, while the behaviors of B_e and B_i are shown in Fig. 3.4.1. The results obtained are shown in Fig. 3.4.3. They are compared to those of the 1D FEM model used previously for the validation of (3.2.52). An excellent agreement is found between the two validating the novel formula proposed. To obtain these results, from t = 0 s to t = 2 s the formulae for the first magnetization (3.2.21) are applied. At t = 1.5 s the drop in the losses is due to the transport current being stationary, and the plateau seen in Fig. 3.4.3 from t = 1.5 s to 2 s, is due to B_e reaching, and then overcoming B_p. Once $B_e = B_p$, the whole slab is filled with current and electric field, thus all the slab contributes to the loss process.

After t = 2.5 s a combination of (3.2.52) and (3.4.1) must be used to calculate the losses. From t = 2.5 s to t = 3.5 s B_e and B_i are apparently ramping down

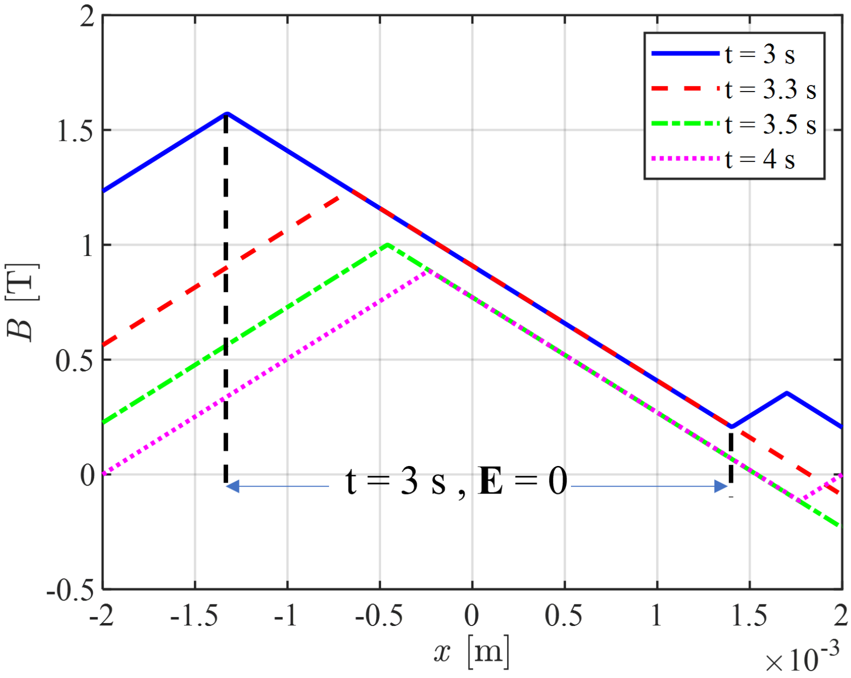

Figure 3.4.2: *Time-resolved representation of the magnetic field profile within the slab, in the case under consideration. Data obtained from 1D COMSOL simulation. The region enclosed by the two dotted lines is devoid of electric field (E) at* $t = 3$ *s, having the profile not changed until then* [20].

in phase with each other: using (3.2.52) it might seem possible to evaluate the losses, but this is incorrect. At t = 3.18 s it is possible to notice that the self-field outvalues the external one. This condition is not taken into consideration in (3.2.52). The expression presented in (3.2.52) can still be applied to evaluate the losses in this time interval, but the definition of B^* in (3.2.27) cannot be applied. The real value of the magnetic field of electric penetration must be obtained from the field profile in the slab. At t = 3.3 s, $B_e = B^*$, and a spike in the value of the losses is found, due to the fact that the slab is filled with both current and electric field. Before reaching the condition $B_e = B^*$, the slab is fully penetrated by the current but the central part is free of electric field thus not generating any losses.

Table 3.4.1: Simulation Parameters new formulae

Tape thickness	100 μm	Tape width	4 mm
Number of tapes	40	Superconductor thickness	1 μm
J_c	$4 \times 10^{10} A/m^2$	Homogenized J_c	$4 \times 10^{8} A/m^2$

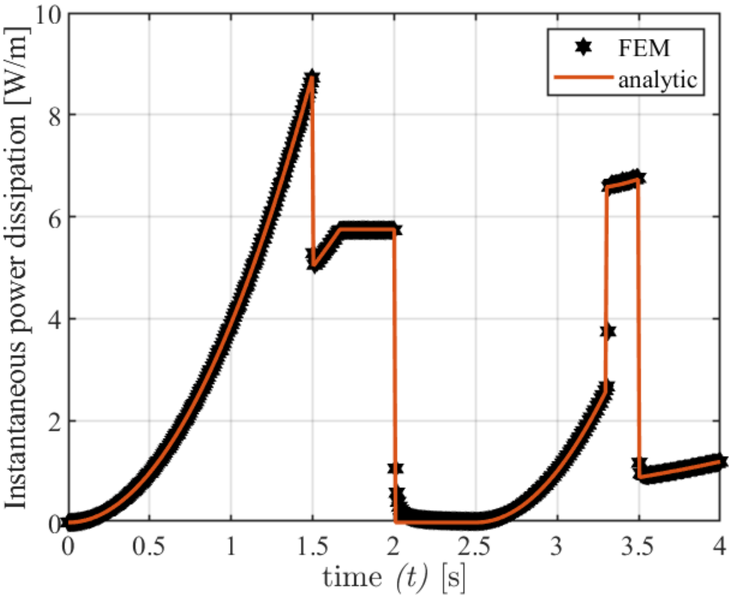

Figure 3.4.3: *Comparison of instantaneous power dissipation in a 40 tape stack, between the 1D FEM model and the analytical formulation developed. Evolution in time of the external and self magnetic field is shown in* Fig. 3.4.1 [20].

3.5 Final considerations

A novel set of equations for the analytical evaluation of hysteresis losses in an infinite slab, subjected to the actions of both a transport current and an external magnetic field, has been developed. The formulae presented here allow us to study generic cycles of the transport current, provided that these are in phase with the magnetic field. An extension to the case where the external magnetic field and the transport current are not in phase with each other has been proved possible, but a compact set of equations cannot be found due to the dependence of the magnetic field of electric penetration on the particular field profile inside the slab. These equations have been tested in various conditions and compared with the results of 1D and 2D FEM models, implemented in COMSOL Multiphysics, to validate their results. The results obtained proved the validity of the formulation presented in this work, although further analysie need to be carried out to finely define the error in employing a formulation for an infinite slab to a finite stack of superconducting tapes.

A method to account for the twisting of the stacked tapes when using the analytical formulae presented has been developed. The substitutive stacks technique has been applied to the calculation of AC losses in the whole REBCO insert of the DEMO CS magnet for a simplified case study. The convergence study performed shows that subdividing a cable twist pitch length, 1 meter long, into 20 sub-elements for the substitutive stacks allows reaching a good accuracy within a reasonable computation time.

A tool for the analytical computation of magnetization losses in HTS twisted stacked conductors for fusion application has also been developed. The model developed allows, using a novel analytical formulation, estimating the AC losses within an acceptable time and is flexible enough to be adapted to different magnet and cable configurations and analytical formulations.

4 *Circuit model for NI-HTS coils*

High-field magnets are key components in many research fields and industrial applications. To achieve the magnetic field needed for these applications the most efficient solution is the use of superconducting magnets. One of the main technical limitations in the use of superconducting magnets is the quench, which can determine irreversible damage to the magnet. A reduction of the risks associated with a quench in high-temperature superconducting (HTS) devices can be achieved through the use of no-insulation (NI) coils [64, 79, 148–151]. The non insulated superconducting technology allows the current to redistribute between turns of the coil during a quench. The radial currents flow from one turn to the adjacent ones, thus reducing the azimuthal current flowing along the normal zone and the corresponding joule losses. This, in turn, mitigates the risk of damage to the superconducting tape [65–67, 152, 153]. The main issues of the non insulated HTS technology are related to the flow of current from turn to turn, also in the absence of quenches, due to inductive effects. This leads to large time constants of both the coil charge and discharge phases [154]. Various solutions were implemented to overcome these shortcomings, ranging from active control of the current source to controlled insulation between turns, (see [155–157]). Superconducting coils are normally designed to work with the same current in each turn. The knowledge of the current redistribution during charges or quenches is useful to predict the coil behavior in terms of time constants and AC losses.

The study of non insulated (NI) high-temperature superconducting (HTS) coils can be undertaken using a 3D finite element method (FEM) model based on the formulation presented in Section 2.3. However, a major drawback of the FEM approach is that it necessitates the use of an extremely fine mesh to accurately represent the behavior of the coil, which often translates into an increase in computational time that may not be feasible during the design phase of the component. Additionally, the increased computational demands and the complexity of the model could lead to non-convergence issues, potentially jeopardizing the validity of the simulations. Therefore, a circuital approach emerges as a more efficient and reliable alternative to the more intricate FEM modeling.

To evaluate the current distribution and AC losses in NI-HTS coils, numerous circuit models were recently developed [76, 152, 158]. However, only a few include the computation of the screening currents in the model [159, 160]. In this work, a nonlinear non-planar 3D circuit model, suited to analyze both radial and screening currents in NI coils, based in part on the concepts defined in [159, 160] and developed in FORTRAN is presented. The code can thus compute the current distribution in operating conditions of the coil and give an estimation of the AC losses.

4.1 Model parameters and solving methods

This first part of this section focuses on the definition of the key parameters defining the geometry of the model and the three kinds of resistances employed therein.

To better represent the phenomenology of the coil, a detailed representation of the tape composing the coil is needed. The tape is subdivided not only across its full length (so across the azimuthal direction of the coil) but also across its width, into a series of sub-elements. This discretization is necessary to study the effect of the magnetization currents, allowing a non-uniform current distribution inside the individual tape. The parameters defining the model geometry are the number of turns of the coil N_t, the number of layers N_l, the number of longitudinal divisions of a turn N_d, and the already mentioned number of sub-elements N_s. The equivalent circuit model of a layer-wound coil is presented in Fig.4.1.1 for the simple case of a coil with two layers and two turns. Each turn in Fig 4.1.1 is divided into two parts ($N_d = 2$) to permit a connection with the adjacent turns through contact resistances. A contact resistance is placed at the end of each division. Although the results proposed in this work are aimed at the study of layer wound NI-HTS coils, the model developed can be applied to the study of tapes, stacks of tapes, or pancake coils just by modifying the topology of the network. The circuit model in Fig. 4.1.1 can also perfectly represent the geometry of a pancake coil, the only differences would be in the calculation of the lumped parameters and thus the geometry data input of the code.

The equivalent lumped parameters circuit depicted in Fig. 4.1.1, is obtained with a two sub-elements division of the tape. The presence of two sub-elements results in two identical planar circuit networks connected by the interelements resistances R_{inter}. Each planar network (highlighted in blue and orange in Fig. 4.1.1) is representative of a sub-element. As the number of sub-elements increases, new planar networks identical to the previous ones are included in the model, and connected via the interelements resistances, the same way the orange circuit is connected to the blue one. The first longitudinal elements of the first layer of each sub-element grid are connected to the source. In this case, an ideal current generator is selected. Alternatively, it is possible to use an ideal voltage generator. The last longitudinal elements of the last layer of each sub-element network are connected to the source so that each planar circuit is closed on it. The longitudinal element is shown in detail in Fig. 4.1.2. The longitudinal inductances and the mutual inductances between them are evaluated numerically from an integration

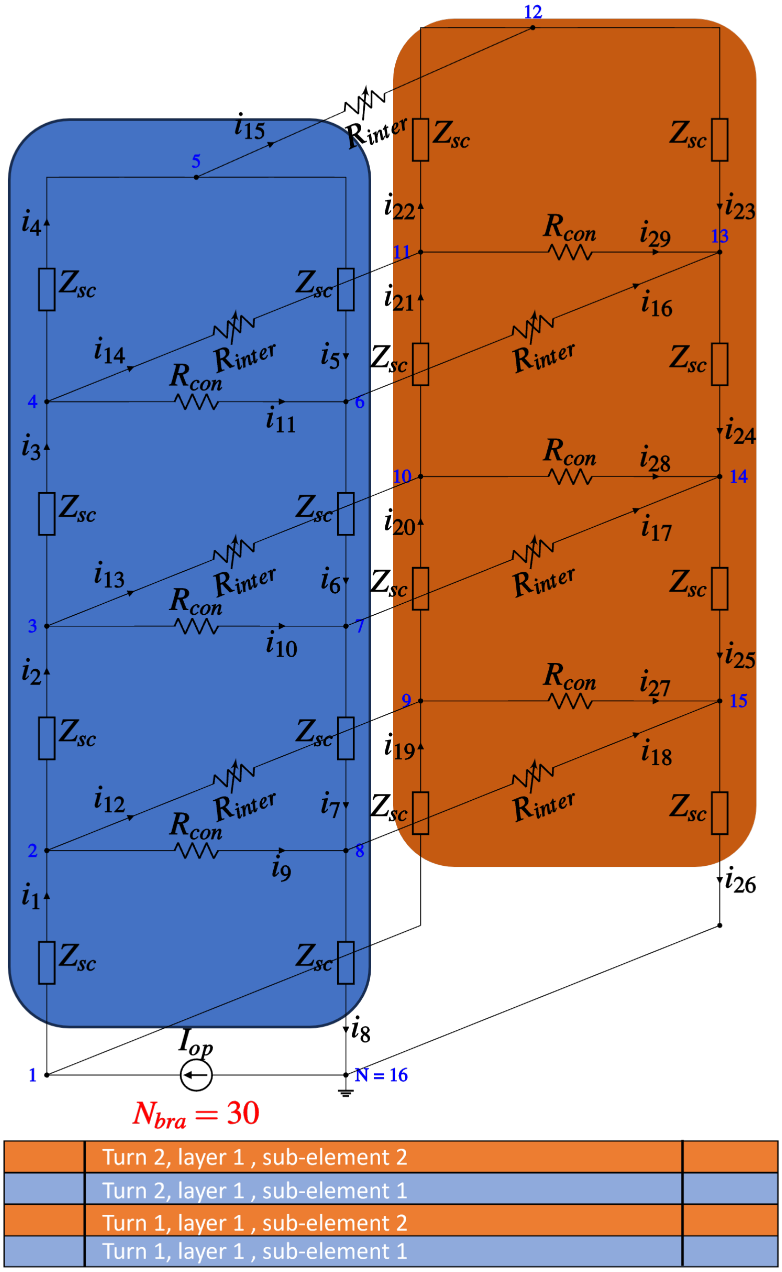

Figure 4.1.1: *Equivalent 3D circuit model for a layer wound coil with two turns and two layers ($N_t = N_l = 2$). Each turn is split in half ($N_d = 2$) to accommodate the connection between layers (R_{con}). The tape is split in half along its width ($N_s = 2$). Below the circuit network a sketch of the cross-section of the coil. In blue the first sub-element, in orange the second one. N_{bra} is the total number of circuit elements. The enumeration of the elements is the same as those of the currents* [21].

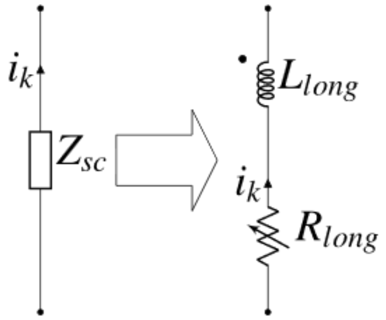

Figure 4.1.2: *Z_{sc} is the series of the longitudinal resistance R_{long} and the longitudianl inductance L_{long}. L_{long} is an inductor mutually coupled with all the other inductors in the network. This configuration is strictly viable when solving the circuit with the loop current method.*

of the scalar potential [145]. The equivalent circuit model defined this way is a nonplanar, nonlinear electric network and can be conveniently solved by the loop currents method. The state equation method was also considered, combined with the nodal analysis. Both solving methods will be discussed later

The formulae for the longitudinal resistance (R_{long}) and the interelements (R_{inter}) resistance, defined by Ohm's law and the power law (2.1.2), are reported in (4.1.1) and (4.1.2). The interelements resistances allow the current redistribution inside the tape by connecting the different subelements.

$$R_{long,i}(J^*_{long,i}) = \rho_{sc}(J^*_{long,i})\frac{L_{long}}{A_{long}} \tag{4.1.1}$$

$$R_{inter,i}(J^*_{inter,i}) = \rho_{sc}(J^*_{inter,i})\frac{L_{inter}}{A_{inter}} \tag{4.1.2}$$

$$\begin{aligned} L_{long} &= L/(N_l N_d N_t), & L_{inter} &= w/N_s \\ A_{long} &= wt/N_s, & A_{inter} &= tL/(N_l N_d N_t) \end{aligned} \tag{4.1.3}$$

It is defined with L the total length of the superconducting tape, w the width of the tape, and t the thickness of the superconducting layer inside of the tape. A_{long} and A_{inter} are the cross sections over which the longitudinal and interelements currents flow respectively. I_{long} is the current flowing in the longitudinal direction, along the resistance R_{long}. I_{inter} is the current flowing between two sub-elements, along the resistance R_{inter}. Both the current I_{inter} and I_{long} are flowing in the AB plane of the superconductor, meaning that for the definition of the longitudinal and interelements resistance (4.1.1) and (4.1.2), it is possible to use the formulae for the resistivity of the superconductor (ρ_{sc}).

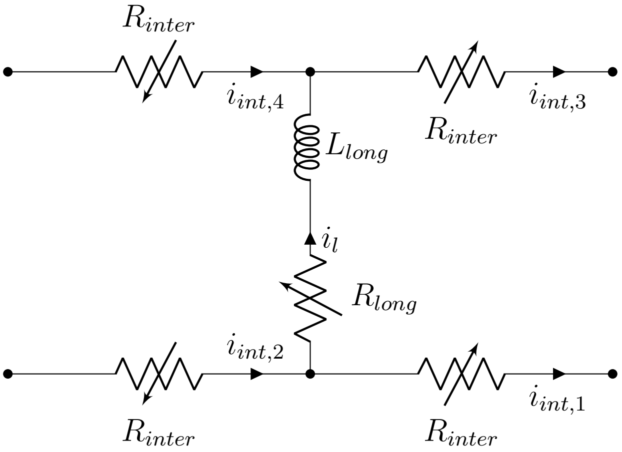

Figure 4.1.3: *Example of one of the possible connections of a longitudinal component, used to determine the value of its current density from the currents in the adjacent branches trough* (4.1.4).

$$J^*_{long,i} = \sqrt{\left(\frac{I_{long,i}}{A_{long}}\right)^2 + \left(\frac{\Delta I_{inter,i}}{FA_{inter}}\right)^2} \tag{4.1.4}$$

$$\Delta I_{inter,i} = \sum_{n=1}^{F} I_{inter,n} \tag{4.1.5}$$

In the case shown in Fig. 4.1.3, the coefficient in (4.1.4) would become as shown in (4.1.6).

$$I_{long,i} = i_l, \quad \Delta I_{inter,i} = \sum_{k=1}^{4} i_{int,k}, \quad F = 4 \tag{4.1.6}$$

Regarding (4.1.4), a brief explanation is necessary. When using a lumped parameters circuit it is necessary to correctly define its parameters, such as the longitudinal resistances via (4.1.1). The resistance is dependent on the modulus of the current density **J**, defined in (4.1.7), where $\hat{l}$ is the unit vector along the longitudinal coordinate, and $\hat{t}$ the unit vector along the transverse one.

$$\mathbf{J} = J_l\hat{l} + J_{int}\hat{t} \tag{4.1.7}$$

However, in a lumped parameters model, sections of the coil are modeled through a single circuit element (R_{long} in the case under exam). This component only represents the longitudinal component of the current density, through the current carried (I_{long}). The flow of the transversal component of **J** can be represented through the interelements resistances R_{inter}. Therefore J_{long}, the longitudinal component of **J**, is equal to I_{long}/A_{long} as if it were constant along the longitudinal direction. Instead, the J_{inter} (transversal component of **J**) is obtained as an average between the value at the start of R_{long} and at its end, see (4.1.5). F is the number of interelements resistances connected to the nodes of the i^{th} longitudinal element (see Fig. 4.1.3). This value is not equal for all the longitudinal circuit elements, it can assume a value of either 2 or 4.

In the author's opinion, this is the best way to correctly represent the longitudinal and transverse current density in the spatial region represented by the longitudinal component R_{long}. Employing (4.1.4) is a necessary step to account for the nonlinearity of the superconductor. The positive direction of the current in all the interelements resistances shown in Fig. 4.1.3 is the same, this condition remains true also when analyzing the real circuit in Fig. 4.1.1 (with the choice of the positive direction of the currents adopted). This condition means that the current density in the transversal direction can be obtained as a simple mean of the current density in each zone represented by the interelements resistances (see (4.1.5)) without any further consideration on the sign of the interelements currents.

$$J^*_{inter,i} = \sqrt{\left(\frac{\Delta I_{long,i}}{SA_{long}}\right)^2 + \left(\frac{I_{inter,i}}{A_{inter}}\right)^2} \tag{4.1.8}$$

$$\Delta I_{long,i} = \sum_{n=1}^{S} I_{long,n} \tag{4.1.9}$$

In the case shown in Fig. 4.1.4, the coefficient in (4.1.8) becomes as shown in (4.1.10).

$$I_{inter,i} = i_i, \quad \Delta I_{long,i} = \sum_{k=1}^{4} i_{long,k}, \quad S = 4 \tag{4.1.10}$$

The same remarks made for (4.1.4) can also be applied to (4.1.8). In the case of a transversal circuit element R_{inter}, the current density along the element is the transversal component of **J**, while the longitudinal component is obtained as an average between all the current densities of the longitudinal elements connected to R_{inter}. As previously shown, even in this case the average between the current

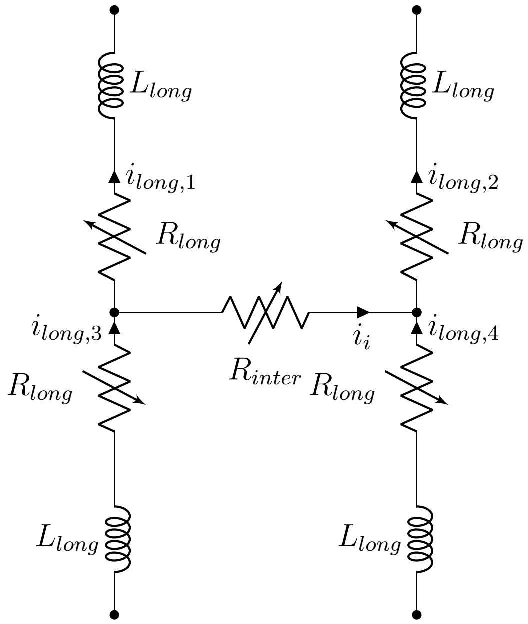

Figure 4.1.4: *Example of one of the possible connections of an interelements resistance, used to determine the value of its current density from the currents in the adjacent branches trough* (4.1.8).

densities in the longitudinal elements can be computed without any changes to the sign of the currents. S is the number of longitudinal elements connected to the nodes of the i^{th} interelements resistance (see Fig. 4.1.4), as F is not constant for all the interelements resistances and can assume a value of either 4 or 2.

The definitions of the longitudinal and interelement resistance given in (4.1.1) and (4.1.2) do not take into consideration the transition of the superconductor towards the normal state expressed in (2.1.3). Before proceeding with the description of the model a quick overview of the impact of this assumption is provided. The superconducting state is in parallel with the normal one, this is expressed in (4.1.11).

$$E = \rho_n J_n = \rho_{sc}(J_{sc})J_{sc} \tag{4.1.11}$$

Where $\rho_{sc}(J_{sc})$ is the resistivity of the superconducting state, and J_{sc} is the current density in the superconducting state see (4.1.12). The term ρ_n is the resistivity of the normal state, and J_n is the current density in the normal state. The total current density in the REBCO can therefore be expressed as in (4.1.13).

$$\rho_{sc} = \frac{E_c}{J_c}\left(\frac{J_{sc}}{J_c}\right)^{n-1} \tag{4.1.12}$$

$$J = J_{sc} + J_n \tag{4.1.13}$$

Equation (4.1.11) can be written as:

$$E = E_c\left(\frac{J_{sc}}{J_c}\right)^{n} = \rho_n(J - J_{sc}) \Rightarrow \frac{\rho_n}{E_c}(J - J_{sc}) - \left(\frac{J_{sc}}{J_c}\right)^{n} = 0 \tag{4.1.14}$$

Knowing the total current density J, it is possible to obtain the superconducting current density J_{sc}, solving numerically (4.1.14). Thus, the resistivity of the superconductor is obtained via (4.1.15).

$$\rho(J) = \frac{\rho_n \rho_{sc}(J_{sc})}{\rho_n + \rho_{sc}(J_{sc})} \tag{4.1.15}$$

If the J_{sc} is not evaluated solving (4.1.14), and instead the resistivity of the superconductor is evaluated via (4.1.16) the error committed becomes non-negligible only at high values of the critical current density see Figs. 4.1.5 and 4.1.6. The parameters of the tape used to obtain Figs. 4.1.5 and 4.1.6 are shown in Table 4.1.1, and the value for ρ_n is taken from [161].

$$\rho(J) = \frac{\rho_n \rho_{sc}(J_{sc})}{\rho_n + \rho_{sc}(J_{sc})} \tag{4.1.16}$$

Table 4.1.1: HTS parameters

ρ_n	$20\ \mu\Omega m$	E_c	$1\ \mu V/cm$
J_c	$10^{10}\ A/m^2$	n	32

The difference between using (4.1.15) or just the power law as done here, is shown in Fig. 4.1.7. The error becomes relevant only after the current density becomes greater than $1.5J_c$, a condition that never occurs in the case studies presented in this thesis.

The contact resistance (R_{con}) depends on the geometry of the coil, i.e. the values of N_d and N_s and the value of the contact resistance between two turns (R_c). R_{con} is the turn-to-turn contact resistance between two turns of different layers in the same sub-element.

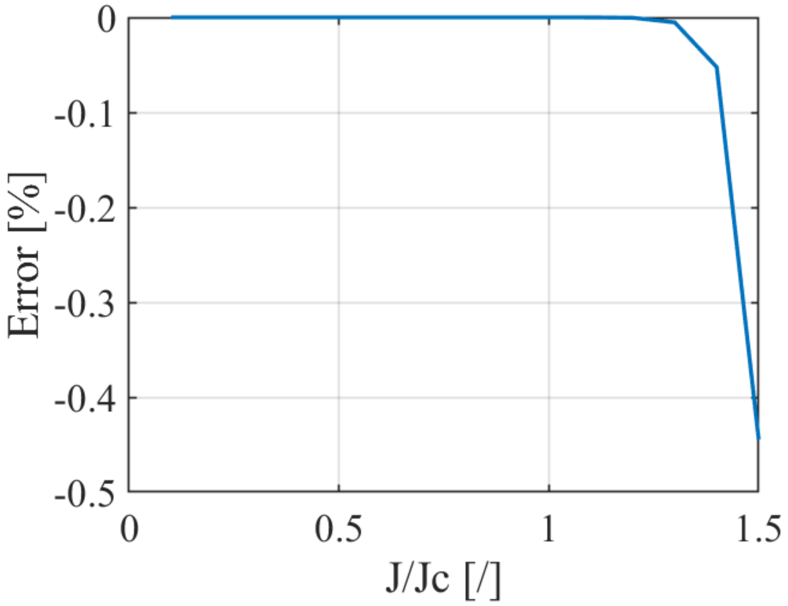

Figure 4.1.5: *Percentage error of the value of the superconducting resistivity between* (4.1.15) *and* (4.1.16) *in the low current density region.*

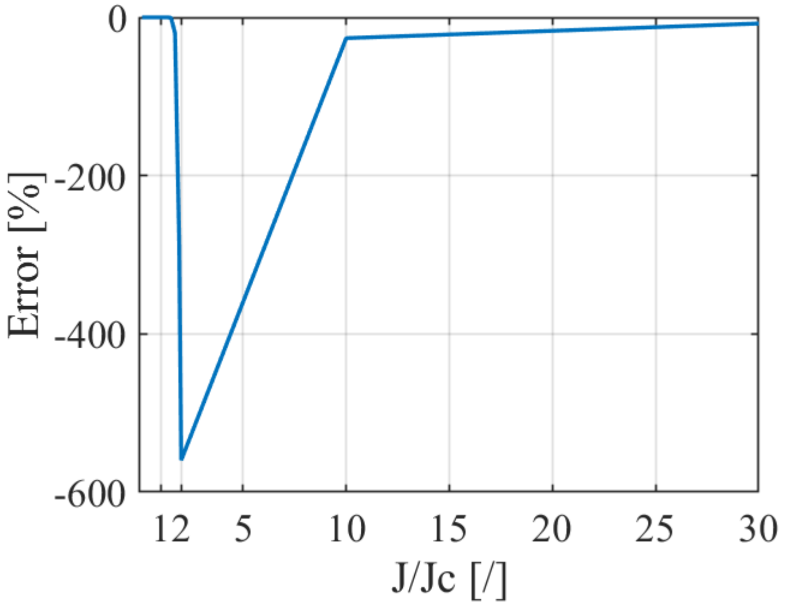

Figure 4.1.6: *Percentage error of the value of the superconducting resistivity between* (4.1.15) *and* (4.1.16) *in the high current density region.*

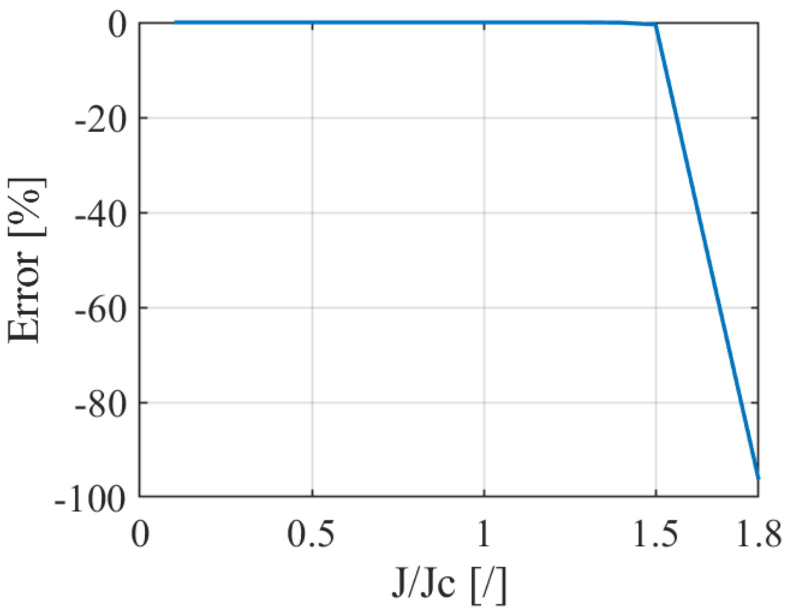

Figure 4.1.7: *Percentage error of the value of the superconducting resistivity between* (4.1.15) *and* (2.1.1).

$$R_{con} = R_c N_d N_s \tag{4.1.17}$$

The total number of longitudinal elements is $N_{long} = (2-m)N_l N_t N_s N_d$, where m is a parameter that takes into account the resolution method used. If the system is solved using the state equations method, the value of m is 0, while using the loop currents method m is 1. The number of inductors is $N_{ind} = N_{long}/(2-m)$, it coincides with the number of longitudinal branches if solving with the loop current method. The matrix of the mutual inductances is a full one with dimension $[N_{ind}, N_{ind}]$, due to each inductor being coupled with all the others. The number of contact resistances between different turns is $N_{cont} = N_s(N_t N_d - 1)(N_l - 1)$, while the number of superconducting interelements resistances is $N_{inter} = (N_s - 1)(N_l N_t N_d - 1)$. The total number of circuit components in the network is $N_{bra} = 1 + N_{long} + N_{cont} + N_{intra}$, where the plus one is due to the source generator. The number of nodes is defined as $N = 2 + N_s(N_{long}/((2-m)N_s) - 1)$. In our model the numeration of the circuit element is not casual, it is chosen to allow one to identify the type of the branch (longitudinal, interelements, contact, source). The first longitudinal element of the first layer of the first subelement is the circuit element number one. After that, the numeration increases following the longitudinal components of the subelement. In each subelement, there are $N_{ln} = N_{ind}/N_s$ longitudinal branches. After all the longitudinal elements of the first subelements are numbered the numeration restarts from the first transversal element of the subelement, and there are $N_{tn} = (N_t N_d - 1)(N_l - 1)$ transversal elements per subelement. Then the interelements elements, if any, are numbered, and in a subelement there are $(N_s - 1)(N_l N_t N_d - 1)/N_s$. Once the first subelement is fully numbered the numeration starts from the second one, following the same principles, and so on. The last circuital element is always the source generator, which is connected between node 1 and the last node of the circuit N. The N^{th} node is taken as the reference node for the state equation method.

4.1.1 State equations method

The state equation method [162–164], also known as the state space approach, is a fundamental technique for analyzing and simulating electrical circuits. Unlike traditional circuit analysis methods that focus on Kirchhoff's laws, the state equation method adopts a more abstract and mathematical approach, transforming the circuit into a dynamic system with a set of state variables and equations. The state variables represent the essential characteristics of the circuit that change over time, such as the voltage in the capacitors or the currents in the inductors. The state equations, on the other hand, describe the relationships between these state variables and the external inputs to the circuit. These equations are typically linear differential equations, which govern the circuit's dynamic behavior.

In the case under analysis, the state variables are the currents flowing in the inductors, and the differential system that needs to be solved is the one in (4.1.18).

$$[M]\frac{d}{dt}\mathbf{I_{ind}} = \mathbf{V}(\mathbf{I_{ind}}) \tag{4.1.18}$$

The matrix [M] is the matrix of the mutual inductances, $\mathbf{I_{ind}}$ is the vector of the state variables, while $\mathbf{V}(\mathbf{I_{ind}})$ is the vector of the voltages of the inductors. To be a system of state equations, $\mathbf{V}(\mathbf{I_i nd})$ has to be expressed as a function of the state variables. To do so, the nodal analysis [164,165] is applied, a brief description is reported here.

The nodal analysis is a solution procedure used for bipolar circuits to determine all the node potentials of the circuit and from these the values of the branch currents and voltages. The main advantage of the nodal analysis is that for a network with n nodes and l branches, it requires the solution of only n-1 equations, with a reduction in the number of equations compared to the n-1 nodal equations and l-n+1 loop equations obtained by directly applying all the linearly independent Kirchhoff laws. The n-1 equations solved in the method are the Kirchhoff laws for the currents in all the nodes except the one chosen as a reference.

The procedure for applying the nodal analysis is as follows:

1. Choose a node of the network as a reference node. The potential in that node is considered known and is commonly set to zero.
2. Assign an orientation to the branches of the circuit under consideration to define whether the currents enter or exit the corresponding nodes.
3. Apply Kirchhoff's current law to the nodes other than the reference node.
4. Use the constitutive laws of the bipolars in each branch to express the branch currents in terms of the node potentials.
5. Solve the system obtained, calculating the voltages at the unknown nodes.

The system of solution equations obtained using the described procedure appears in the following form:

$$[G]\mathbf{V} = \mathbf{H} \tag{4.1.19}$$

Where [G] is the conductance matrix defined in (4.1.20) and (4.1.21), **V** is the vector of the nodal potential, while **H** is the vector of the known term dependent on the source see (4.1.22).

$$[G] = \begin{bmatrix} g_{1,1} & g_{1,2} & \cdots & g_{1,n-1} \\ g_{2,1} & g_{2,2} & & \vdots \\ \vdots & & \ddots & \vdots \\ g_{n-1,1} & \cdots & \cdots & g_{n-1,n-1} \end{bmatrix} \tag{4.1.20}$$

$$g_{i,i} = \sum g_i \quad , \quad g_{i,j} = -\sum_{i \neq j} g_{i,j} \tag{4.1.21}$$

The elements on the diagonal of [G] are the sums of the conductances connected to the nodes for which the equation is written (g_i, generic conductance connected to node i), while the elements off the diagonal are the sum of the conductances between that node and all the others ($g_{i,j}$ conductance between nodes i and j).

$$\mathbf{V} = \begin{Bmatrix} V_1 \\ V_2 \\ \vdots \\ V_{n-1} \end{Bmatrix} \quad , \quad \mathbf{H} = \begin{Bmatrix} h_1 \\ h_2 \\ \vdots \\ h_{n-1} \end{Bmatrix} \quad h_i = \sum \alpha I_i \tag{4.1.22}$$

The elements of the known term $\mathbf{H}$, h_i, are the sum of the currents of the current generators connected to the node i^{th}, which are the currents in the inductors. In the application of the nodal analysis, inductors are considered as current generators. Their impressed current values are the currents of the inductors themselves, which have to be known. The currents are considered negative if they exit the node or positive if they enter it; the direction of the currents is taken into account by the coefficient α. The node potentials are then obtained as in (4.1.23):

$$\mathbf{V} = [G]^{-1}\mathbf{H}(\mathbf{I_{ind}}) \tag{4.1.23}$$

It is now possible to describe how the solving method was implemented and the main issues encountered in its application.

Assuming t_0 as the start time of the simulation and t_f as the end time, the chosen solver (Runge Kutta 4-5 [166], implicit Euler [167], etc.) solves the ordinary differential equations (ODE) with a time step Δt. The time integration step is not necessarily constant and is actively adapted by the routine implemented. At each t (time instant requested by the solver within the Δt) the circuit is solved through the nodal analysis to obtain the voltages in the inductors, which are the known terms of the system of state equations. To apply the nodal analysis, it is necessary to know the values of the resistors in the circuit network. Some of the resistances in the circuit are nonlinear functions of the current. It is assumed that the values of the interelements resistors are constant over time intervals that are longer than the integration time step. The choice to keep the resistances constant over the integration interval is dictated by the need to reduce calculation times.

This assumption in turn determines a first problem with this solution method: the integration step Δt must be sufficiently small to consider the approximation valid. It should be taken into account that the nonlinear resistance depends on the current, which varies during the time interval Δt. The assumption of constant resistance is therefore valid only if the current variations are small during the interval Δt.

A second issue is represented by the presence of inductor cut sets; the studied network is therefore degenerate and cannot be solved. To overcome this problem, it is necessary to add a fictitious resistance R_p in parallel to the series longitudinal inductor and resistance. This results in changing the circuit configuration from that shown in Fig. 4.1.2 to that shown in Fig. 4.1.8. The inclusion of this fictitious resistance makes the circuit less representative of the physical reality and its value (which should tend to infinity for an ideal representation) has a direct impact on the time constant of the circuit and on the calculation time required for its solution. Simulations show that increasing the value of R_p increases the solution time of the circuit. If R_p is sufficiently large, it is possible to reach convergence to a correct value of the solution.

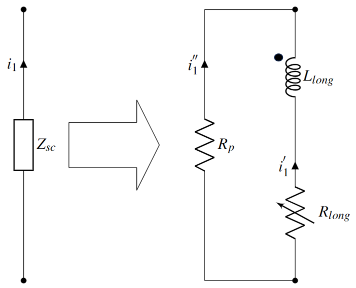

Figure 4.1.8: *Longitudinal component configuration of the circuit model developed, used when solving with the state variable method coupled with the nodal analysis to prevent cut sets of inductor.*

4.1.2 Loop currents method

To address the limitations of the state equation method when combined with nodal analysis, an alternative solver was developed based on the current loop method [164, 168]. In this section, a brief explanation of the method itself will be presented, followed by a detailed discussion on how to implement it in the presented case.

To understand the loop currents method, it is necessary to introduce the definition of tree and cotree [164]. In graph theory, a tree is a set of branches of the graph that connect all the nodes of the circuit without forming any closed path. The cotree is the set of branches of the graph that do not belong to the tree. It is important to note that the tree and the cotree are not uniquely defined.

The loop currents method is a solution procedure for two-terminal circuits that is suitable for determining all the currents in the cotree branches of the circuit network. It can be shown that all the currents in the circuit elements are a linear combination of the cotree currents. The main advantage of the loop currents method is that for a network with n nodes and l branches, it requires the solution of only l-n+1 equations, as opposed to the n-1 nodal equations and the l-n+1 loop equations obtained by directly applying the linearly independent Kirchhoff's laws. The l-n+1 equations considered are Kirchhoff's voltage laws in all the fundamental loops. A fundamental loop is a loop of the circuit containing a single cotree branch, while all the other branches of the loop belong to the tree.

The resolving procedure for the loop currents methods is as follows:

1. Choose a tree of the circuit.
2. Identify the fundamental loops.
3. Assign an orientation to the branches of the circuit under consideration and to the currents of the fundamental loops.
4. Use the constitutive laws of the two-terminal elements in each branch to express the branch voltages in terms of the cotree currents.
5. Write the Kirchhoff's voltage law (KVL) for all the fundamental loops.
6. Solve the resulting system, calculating the cotree currents.

The first step is to identify a tree for the circuit. The structure of the circuital model allows for a straightforward identification of the tree. The longitudinal circuit elements of the first subelement are all part of the tree. All the longitudinal circuit elements (except for the last one in each subelement) of the subsequent subelements are also part of the tree. The source generator is always treated as the last cotree branch. The remaining branches are therefore part of the cotree, which includes all the interelements resistances and all the contact resistances. Looking at the circuit in Fig. 4.1.1, the tree is composed of the circuit elements numbered from 1 to 8 (longitudinal components of the first subelement) and those numbered from 12 to 18. These considerations are implemented in the code developed so that nearly no computational time is spent searching for a tree.

In the absence of current generators in the circuit, the resulting system is as follows:

$$[R]\mathbf{I} = \mathbf{V} \tag{4.1.24}$$

In our model, the source can either be a current generator or a voltage generator. When using the current generator, the loop current method is still applicable, and the number of equations drops by one. It is not necessary to write an equation for the current source because that current is already known. Therefore, (4.1.24) is always valid.

[R] is the matrix of resistances, defined in (4.1.25) and (4.1.26).

$$[R] = \begin{bmatrix} r_{1,1} & r_{1,2} & \cdots & r_{1,l-n+1} \\ r_{2,1} & r_{2,2} & & \vdots \\ \vdots & & \ddots & \vdots \\ r_{l-n+1,1} & \cdots & \cdots & r_{l-n+1,l-n+1} \end{bmatrix} \tag{4.1.25}$$

$$r_{i,i} = \sum r_i \quad , \quad r_{i,j} = -\sum_{i \neq j} r_{i,j} \tag{4.1.26}$$

The elements on the diagonal of [R] are the sum of the resistances of the loop to which the equation corresponds; the elements off the diagonal are the sum of the resistances in common between the loop under consideration and the adjacent loops ($r_{i,j}$ is the resistance in common between loops i and j) taken with a positive or negative sign depending on whether the resistances in common are crossed in the same direction or opposite direction by the two loop currents. The unknowns of the problem (the cotree currents), compose the vector **I** see (4.1.27). The elements of the known term **V** represent the sum of the voltages of the voltage generators in the loop under consideration, see (4.1.28). The coefficient α takes into account the orientation of the loop.

$$\mathbf{I} = \begin{Bmatrix} I_1 \\ I_2 \\ \vdots \\ I_{l-n+1} \end{Bmatrix} \tag{4.1.27}$$

$$\mathbf{V} = \begin{Bmatrix} v_1 \\ v_2 \\ \vdots \\ v_{l-n+1} \end{Bmatrix} \qquad v_i = \sum \alpha V_i \tag{4.1.28}$$

It is now described how to write the equations with the loop current method for the circuit model developed in this work. To obtain a more compact and precise mathematical formulation, let us consider the case where the numeration of the branches is so that the first l-n+1 branches belong to the cotree, and so the first l-n+1 currents of the current vector are the cotree currents. The writing of the generic k^{th} equation of the system assumes that the k^{th} loop is composed of the k^{th} cotree branch and r_k tree branches. The k^{th} equation for the generic loop is shown in Fig. 4.1.9 is therefore:

$$v_k + \sum_{m=1}^{r_k} \alpha_{k,m} v_{k,m} = 0 \tag{4.1.29}$$

Where r_k is the number of tree branches in the k^{th} loop, $a_{k,m}$ is the coefficient that takes into account the positive direction chosen for the loop current. As shown in Fig. 4.1.9, the positive direction of the loop current is chosen in accordance with the positive direction of the current in the cotree branch that identify the loop.

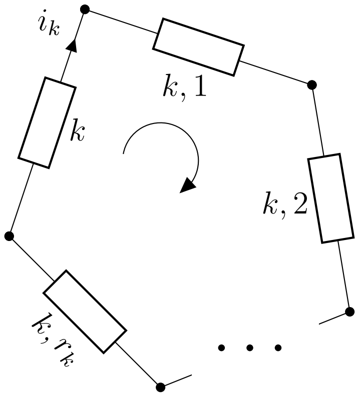

Figure 4.1.9: *Generic representation of the K^{th} fundamental loop. The component labeled as "k" is the cotree branch, while the other are the tree branches. The positive direction of the loop current is shown via the curved arrow line.*

The function s is defined as the loop index function, *s(k,m)* is the index of the m^{th} tree branch in the k^{th} fundamental loop. For example if *s(k,m)* $=10$, it means that the m^{th} tree branch in the k^{th} fundamental loop is the tenth element of the circuit. Equation (4.1.29), always holds, but the expression for the voltage changes depending on whether the component is an inductor, a resistor, or, as it is in the present model, a series of both. The possible cases will now be examined.

If the tree branch of index *s(k,m)* is an inductor, then the constitutive relationship of the branch is as follows:

$$v_{k,m} = \sum_{w=1}^{N_{long}} M_{s(k,m),a(w)} \frac{di_{a(w)}}{dt} \tag{4.1.30}$$

where N_{long} is the number of longitudinal components in the circuit, which in this case coincides with the number of inductors. The function *a(w)* is another index function; it returns the index of the w^{th} inductor. Using another example for the sake of clarity, having *a(w)* $=10$ means that the w^{th} inductor corresponds to the tenth component (circuit element) of the circuit. The coefficients M are the self and mutual inductances.

$$i_{a(w)} = \sum_{h=1}^{l-n+1} c_{a(w),h} i_h \tag{4.1.31}$$

Equation (4.1.31) shows how each current in the circuit can be obtained as a combination of the l-n+1 fundamental loop currents. The currents in the fundamental loops coincide with the cotree currents. The term $c_{a(w),h}$ is a coefficient that can only take the values 0 or 1. Introducing (4.1.31) into (4.1.30) yields:

$$\begin{aligned} v_{k,m} &= \sum_{w=1}^{N_{long}} M_{s(k,m),a(w)} \sum_{h=1}^{l-n+1} c_{a(w),h} \frac{di_h}{dt} \\ &= \sum_{h=1}^{l-n+1} \left(\sum_{w=1}^{N_{long}} M_{s(k,m),a(w)} c_{a(w),h} \right) \frac{di_h}{dt} \\ &= \sum_{h=1}^{l-n+1} M^*_{k,m,h} \frac{di_h}{dt} \end{aligned} \tag{4.1.32}$$

Equation (4.1.32) represents the relationship between the voltage across each inductor and the derivatives of the currents in it and all the other inductors in the circuit.

Instead, if the $s(k,m)^{th}$ circuit element is a pure resistor, the constitutive relation of the branch changes from (4.1.30) to (4.1.33).

$$v_{k,m} = R_{s(k,m)}(J^*_{s(k,m)}) i_{s(k,m)} = R_{s(k,m)}(J^*_{s(k,m)}) \sum_{h=1}^{l-n+1} c_{s(k,m),h} i_h \tag{4.1.33}$$

The same notation used for (4.1.1) and (4.1.2) is used in (4.1.33), denoting that the resistance of the K^{th} branch (which is a tree branch and therefore a superconducting longitudinal resistance), is dependent on the modulus of the current density. The modulus of the current density is in turn dependent not only on the current in the K^{th} branch, as stated by (4.1.4) and (4.1.8).

In the circuit model the tree branches, which as previously stated correspond to the longitudinal circuit elements, are composed only of R-L series components (see Fig. 4.1.2) and never by a single inductor (which is not present at all) or by a single resistor. Therefore, the expression for the voltage of a generic tree branch, $v_{k,m}$, is as in (4.1.34).

$$v_{k,m} = R_{s(k,m)}(J^*_{s(k,m)}) \sum_{h=1}^{l-n+1} c_{s(k,m),h} i_h + \sum_{h=1}^{l-n+1} M^*_{k,m,h} \frac{di_h}{dt} \tag{4.1.34}$$

Having defined a formulation for the tree branches, the same will be proposed for the cotree branches. A cotree branch can be either a pure resistor or an R-L series.

If the k^{th} cotree branch is a pure resistor its voltage v_k can be expressed as:

$$v_k = R_k(J_k^*)i_k = R_k((J_k^*)\sum_{h=1}^{l-n+1} c_{k,h}i_h \tag{4.1.35}$$

Therefore the k^{th} resolving equation is written as:

$$\sum_{h=1}^{l-n+1}\left[\sum_m \alpha_{k,m}M_{k,m,h}^*\right]\frac{di_h}{dt} + \sum_{h=1}^{l-n+1}\left[R_k(J_k^*)c_{k,h} + \sum_m \alpha_{k,m}R_{s(k,m)}(J_{s(k,m)}^*)\right] i_h = 0 \tag{4.1.36}$$

The expressions in (4.1.35) and so in (4.1.36) hold when the k^{th} cotree branch is a superconducting resistor, so the interelements resistances. In case the cotree branch is a contact resistance, the only difference would be that R_k is not a function of the current density.

If the k^{th} cotree branch is an R-L series, its voltage v_k can be expressed as follows:

$$\begin{aligned} v_k &= R_k(J_k^*)i_k + \sum_{w=1}^{N_{long}} M_{a(k),a(w)}\frac{di_{a(k)}}{dt} \\ &= R_k(J_k^*)\sum_{h=1}^{l-n+1} c_{k,h}i_h + \sum_{w=1}^{N_{long}} M_{a(k),a(w)}\sum_{h=1}^{l-n+1} c_{a(w),h}\frac{di_h}{dt} \\ &= R_k(J_k^*)\sum_{h=1}^{l-n+1} c_{k,h}i_h + \sum_{h=1}^{l-n+1}\left(\sum_{w=1}^{N_{long}} M_{a(k),a(w)}c_{a(w),h}\right)\frac{di_h}{dt} \\ &= R_k(J_k^*)\sum_{h=1}^{l-n+1} c_{k,h}i_h + \sum_{h=1}^{l-n+1} M_{k,h}^*\frac{di_h}{dt} \end{aligned} \tag{4.1.37}$$

The k^{th} solving equation is then written as:

$$\begin{gathered} \sum_{h=1}^{l-n+1}\left[M_{k,h}^* + \sum_m \alpha_{k,m}M_{k,m,h}^*\right]\frac{di_h}{dt} + \\ \sum_{h=1}^{l-n+1}\left[R_k(J_k^*)c_{k,h} + \sum_m \alpha_{k,m}R_k(J_k^*)(i_{s(k,m)})\right] i_h = 0 \end{gathered} \tag{4.1.38}$$

The resulting system that needs to be solved can be expressed in matrix form as:

$$[\bar{M}]\frac{d\mathbf{I}}{dt} + [R(\mathbf{I})]\mathbf{I} = 0 \tag{4.1.39}$$

The matrix $[\bar{M}]$ is the matrix of the coefficients and is a combination of the matrix of the mutual inductances. **I** is the vector of the cotree currents, and [R(**I**)] is a nonlinear matrix dependent on the resistances of the circuit.

A simple example is now proposed for the application of the loop current method. The equivalent circuit of a three-turn, two-layer coil is shown in Fig. 4.1.10. For simplicity, each turn is considered as a whole tape: $N_d = N_s = 1$, $N_t = 3$, and $N_l = 2$. The nodes of the circuit are shown in blue, while the circuit element number is shown in red. The positive direction of the currents in each element is shown in Fig. 4.1.10. The tree and cotree of the circuit are highlighted in Fig. 4.1.11.

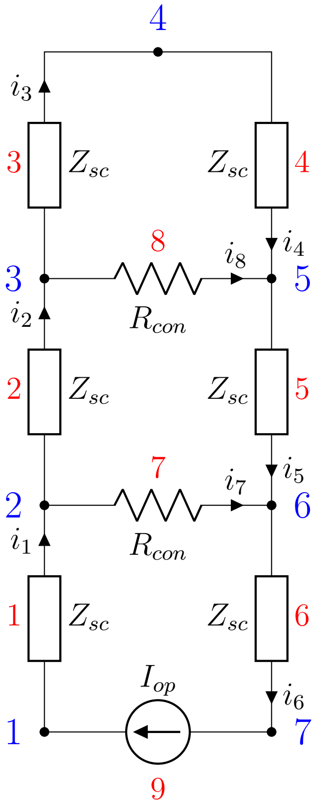

Figure 4.1.10: *Equivalent circuit of a two-layer, three-turns, layer wound coil.*

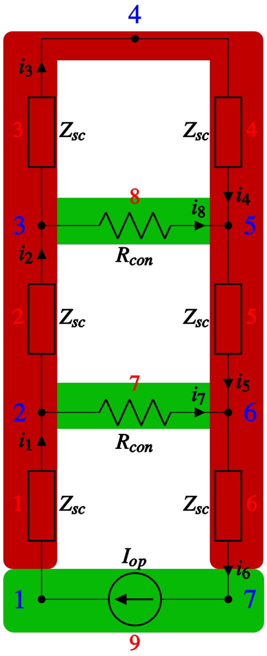

Figure 4.1.11: *Highlighted in red are the tree branches, while in green are the cotree branches.*

The cotree branches are the circuit elements numbered 7, 8, and 9. There are only three cotree branches, one of which is the current source. This means that there are only two unknowns in the problem. $\mathbf{I}$, the vector of the cotree currents, is defined in (4.1.40), while $\mathbf{I_{long}}$ the vector of the tree currents is defined in (4.1.41). The fundamental loop associated with circuit element 7 (first cotree branch) is composed of the following elements: 7-2-3-4-5. The fundamental loop corresponding to the second cotree branch is constituted by the following sequences of branches: 7-2-3-4-5. The resolving equations for the fundamental loops are reported in (4.1.42) and (4.1.43).

$$\mathbf{I} = \begin{Bmatrix} i_7 \\ i_8 \\ i_9 \end{Bmatrix} \tag{4.1.40}$$

$$\mathbf{I_{long}} = \begin{Bmatrix} i_1 \\ i_2 \\ i_3 \\ i_4 \\ i_5 \\ i_6 \end{Bmatrix} \tag{4.1.41}$$

$$\begin{aligned}R_{con}i_7 =&R_{long}(J_2^*)i_2 + \sum_{i=1}^{6} M_{2,i}\frac{di_i}{dt} + R_{long}(J_3^*)i_3 + \sum_{i=1}^{6} M_{3,i}\frac{di_i}{dt}+\\ &R_{long}(J_4^*)i_4 + \sum_{i=1}^{6} M_{4,i}\frac{di_i}{dt} + R_{long}(J_5^*)i_5 + \sum_{i=1}^{6} M_{5,i}\frac{di_i}{dt}\end{aligned} \tag{4.1.42}$$

$$R_{con}i_8 = R_{long}(J_3^*)i_3 + \sum_{i=1}^{6} M_{3,i}\frac{di_i}{dt} + R_{long}(J_4^*)i_4 + \sum_{i=1}^{6} M_{4,i}\frac{di_i}{dt} \tag{4.1.43}$$

All the tree currents are now expressed as a function of the cotree ones:

$$\mathbf{I_{long}}(i) = \sum_{j=1}^{3} c_{i,j}\mathbf{I(j)} \Rightarrow \mathbf{I_{long}} = [C]\mathbf{I} \tag{4.1.44}$$

$$[C] = \begin{bmatrix} 0 & 0 & 1 \\ -1 & 0 & 1 \\ -1 & -1 & 1 \\ -1 & -1 & 1 \\ -1 & 0 & 1 \\ 0 & 0 & 1 \end{bmatrix} \tag{4.1.45}$$

4.1.3 Final considerations on the solving methods

Of the two circuit analysis methods discussed in the previous sections, the loop currents method appears to be the most suited for this circuit and has thus been selected for this study. This is primarily attributable to the employed circuit's resemblance to the actual device being investigated and its reduced number of circuit elements compared to the one needed for the state equation method. However, the formulation still may encounter difficulties in particular cases, as demonstrated in the following example.

Considering the circuit sketched in Fig. 4.1.12, the cotree is composed of the resistors R_a, R_b, R_c, and the current generator. It is possible to express the currents of the tree branches as a combination of the currents i_a, i_b, i_c and I_{op}:

$$\begin{cases} i_1 = i_c - i_a \\ i_2 = i_a - i_b \\ i_3 = i_b - i_c + I_{op} \end{cases} \tag{4.1.46}$$

The resolving system can then be written as follows:

$$\begin{cases} (L_1+L_2)\frac{di_a}{dt} - L_2\frac{di_b}{dt} - L_1\frac{di_c}{dt} = R_1(i_c-i_a) - R_2(i_a-i_b) - R_a i_a \\ -L_2\frac{di_a}{dt} + (L_2+L_3)\frac{di_b}{dt} - L_3\frac{di_c}{dt} = R_2(i_a-i_b) - R_3(i_b+I_{op}-i_c) - R_b i_b - L_3\frac{dI_{op}}{dt} \\ -L_1\frac{di_a}{dt} - L_3\frac{di_b}{dt} + (L_1+L_3)\frac{di_c}{dt} = -R_1(i_c-i_a) + R_3(i_b+I_{op}-i_c) - R_c i_c + L3\frac{dI_{op}}{dt} \end{cases} \tag{4.1.47}$$

As done for the previous example and stated in the method description, the equation of the fundamental loop belonging to the source generator is omitted as that loop current is known and is equal to I_{op}. The system of equations in (4.1.47) can be written in matrix form as:

$$[\bar{M}]\frac{d}{dt}\mathbf{I} = \mathbf{K} \tag{4.1.48}$$

where

$$\bar{M} = \begin{bmatrix} (L_1+L_2) & -L_2 & -L_1 \\ -L_2 & (L_2+L_3) & -L_3 \\ -L_1 & -L_3 & (L_1+L3) \end{bmatrix} \tag{4.1.49}$$

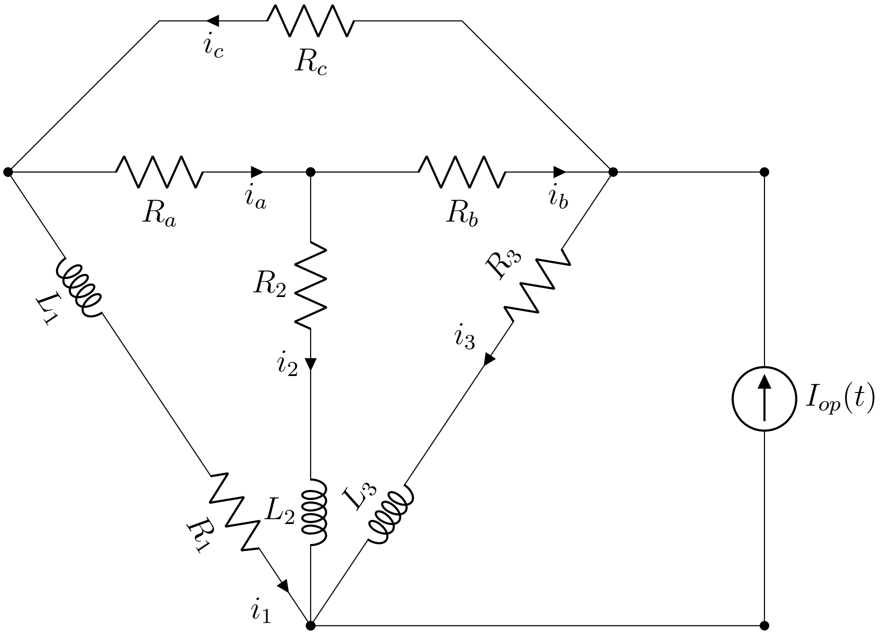

Figure 4.1.12: Generic circuit, comprising all the main elements of the circuit model previously described.

$$\mathbf{I} = \begin{Bmatrix} i_a \\ i_b \\ i_c \end{Bmatrix} \tag{4.1.50}$$

$$\mathbf{K} = \begin{bmatrix} -(R_1 + R_2 + R_a) & R_2 & R_1 \\ R_2 & -(R_2 + R_3 + R_b) & -R_3 \\ R_1 & R_3 & -(R_1 + R_3 + R_c) \end{bmatrix} \begin{Bmatrix} i_a \\ i_b \\ i_c \end{Bmatrix} + \begin{Bmatrix} 0 \\ -L_3 \frac{dI_{op}}{dt} \\ L_3 \frac{dI_{op}}{dt} \end{Bmatrix} \tag{4.1.51}$$

The matrix $[\bar{M}]$ multiplying the time derivative of the cotree currents is the matrix of coefficients, but in this case, it is a singular matrix with a null determinant. Summing all the equations of the system gives an algebraic equation linking the three cotree currents:

$$R_a i_a + R_b i_b + R_c i_c = 0 \tag{4.1.52}$$

The purpose of this simplified example is to demonstrate that: whenever a loop of cotree branches is formed in a circuit with time-dependent elements (inductor or capacitor), and the circuital elements within the loop are purely algebraic, the system of differential equations written through the loop current method cannot be solved using any ordinary differential equation (ODE) solver.

In our circuit model, an algebraic loop of cotree branches is formed for each configuration of the coil that verifies the condition in (4.1.53).

$$N_s > 1 \quad \& \quad N_l > 1 \quad \& \quad (N_t || N_d) > 1 \tag{4.1.53}$$

To overcome this issue several different approaches are available. The first solution is to change the solver of the differential equation. The problem is no longer a system of ODE, but a system of algebraic-differential equations that needs to be solved through a DAE solver [169].

The second option is to include all the inductances linked to the contact resistance in the model so that no algebraic loops can be formed. This would increase the dimension of the matrix of mutual inductances $[M]$ (which is full), increasing the computation burden.

A third possibility is to try to find a different tree of the circuit that could exclude the possible formation of cotree algebraic loops.

The last option is to introduce a small enough quantity, (ϵ), on the diagonal of the coefficient matrix obtained from the original circuit. This last option is akin to introducing an uncoupled inductance in all the cotree branches. This latter option is the solution that was implemented.

4.2 Circuit model applied to straight tapes

The first application of the circuit model is the study of the AC losses due to the transport current in straight tapes. This analysis is necessary to understand if the discretization of the tape proposed is able to represent the characteristic behavior of the current inside the tape (screening currents). The results obtained from the equivalent circuit model were compared with those of a 2D finite element method (FEM) model (using the A-V formulation 2.3.4), developed in [170] and already validated with experimental data and the Norris' formula (2.2.1).

The tape geometry can be obtained by setting $N_l = 1$ and $N_t = 1$, and setting the routine for the evaluation of the mutual inductance matrix to work on 3D parallelepipeds instead of arches with rectangular sections used for the analysis of coils with curved tapes. The longitudinal subdivision of the tape is N_d, and the number of subdivisions across its width is indicated by N_s. The graphical representation of the tape subdivision is presented in Fig. 4.2.1, while in Fig. 4.2.2 the subelements are highlighted on the tape geometry.

4.2.1 Convergence study and experimental validation

The first simulations performed consisted of the evaluation of losses due to a sinusoidal transport current with frequency f and a ratio between the peak current and the critical current set to 0.7. The other relevant data are reported in Table 4.2.1. A convergence study was performed to determine the minimum number of circuit elements required for numerical convergence, namely the values of N_d and N_s. The results of the convergence study are shown in Fig. 4.2.3 and Fig. 4.2.4.

Table 4.2.1: Simulation Parameters 4 mm YBCO tape

Tape Length (L)	0.3 m	J_c	10^{10} A/m^2
Thickness sc. layer (t)	1.5 μm	Tape width (w)	4 mm
frequency	50 Hz	I_c	60 A
n-index	43	Peak current (I_m)	42 A
E_c	100 $\mu V/m$	Simulation time	0.04 s

These results indicate that at least 50 sub-elements across the tape width are needed to correctly represent the screening currents inside a 4 mm tape (see Fig. 4.2.3). Once the right amount of sub-elements N_s needed for a good representation of the screening currents is reached, the impact of the longitudinal discretization N_d is almost negligible Fig. 4.2.4. The average relative difference between the results obtained via the detailed circuit model and the Norris formula is 5.5%, while for the 2D FEM model, it is only 1.3%. The results obtained with the equivalent circuit model are in good agreement with both benchmarks. In the simulations presented here, only the superconducting layer of the tape is modeled with the circuit model. The instantaneous power losses are shown in Fig. 4.2.5. Their behavior in time is coherent with what is expected. The losses are lower during the first magnetization (first peak of the sinusoidal transport current). After that, the losses stabilize to a periodic behavior. The losses are obtained using Ohm's law on each resistive circuit element. Only the second cycle was used in the determination of the AC losses to avoid the influence of the first magnetization and be coherent with the Norris formula.

Fig. 4.2.6 represents the spatial current distribution along the width of the tape as a function of time. Fig. 4.2.6 shows the current over time of selected circuit elements belonging to the first longitudinal element. It is worth noting that the current in the tape is symmetrically distributed across its width: the current in the first subelement ($N_s = 1$) is the same as the last one ($N_S = 100$) and the same is true for all the other subelements. The current is lower in the center of the tape (subelements number 49 and 51) due to the shielding of the external parts of the tape (subelements numberer 1 and 100). The current increases toward the extremities of the tape. It is higher, and even distorted due to nonlinear effects, at the edges of the tape. This behavior is also in accordance with the theoretical predictions. The computation times for all the simulations performed for the circuit model of the 4 mm YBCO straight tape are shown in table 4.2.2. In the table the effecting time to solve the circuit after calculating the matrix of the mutual inductances is indicated as "Solving time". The time for the computation of the matrix of the mutual inductances is indicated as "Time inductance matrix". For comparison, the 2D FEM model requires 66 s to reach a solution. All the simulations were performed on a 4-core, 3.60 GHz Intel(R) Core(TM) i7-7700 processor.

The ODE system was solved by the TRX2 method [171], with the Newton-Rhapson's technique adopted to solve the nonlinear equation at each step of the ODE [172]. An analytic Jacobian matrix is used for this purpose. To ensure the correctness of the results, the ODE system was also solved by the Cash-Karp Embedded Runge-Kutta of 5^{th} order method [166]. Both methods yield the same

Table 4.2.2: Computation time comparison

N_d	N_s	*Time inductance matrix* [s]	*Solving time* [s]
5	5	0.234	0.810
5	10	0.641	0.515
5	20	1.624	1.157
5	30	3.124	1.900
5	40	4.906	2.703
5	50	7.234	3.454
5	60	9.75	5.063
5	70	12.81	6.733
5	80	16.53	8.073
5	90	20.06	11.34
5	100	24.31	14.25
2	60	3.220	1.530
10	60	5.374	14.17
15	60	41.10	27.90
20	60	63.64	48.09

results. The analytical Jacobian calculation method is now presented. The definition of the Jacobian matrix for a generic system **f** dependent on the variables **x** is in the following:

$$[J] = \begin{bmatrix} \frac{\partial f_1}{\partial x_1} & \frac{\partial f_2}{\partial x_1} & \cdots & \frac{\partial f_n}{\partial x_1} \\ \frac{\partial f_1}{\partial x_2} & \frac{\partial f_2}{\partial x_2} & & \vdots \\ \vdots & & \ddots & \vdots \\ \frac{\partial f_1}{\partial x_n} & \cdots & \cdots & \frac{\partial f_n}{\partial x_n} \end{bmatrix} \Rightarrow J_{i,j} = \frac{\partial f_i}{\partial x_j} \tag{4.2.1}$$

In the presented case, when solving with the loop currents method, the system takes the form reported in (4.1.39) and (4.1.48). This means that the function f can be written as:

$$\mathbf{f} = -[R]\mathbf{I}, \quad \mathbf{I} = \begin{Bmatrix} i_1 \\ \vdots \\ i_n \end{Bmatrix} \tag{4.2.2}$$

I is the vector of the cotree currents, while [R] is the matrix of resistances (see example in (4.1.51)). Recalling the definition given in (4.1.2) we can write:

$$f_i = -\sum_{k=1}^{r_i} R_{s(i,k)} \left(\sum_{j=1}^{n} C_{s(i,k),j} i_j \right) \tag{4.2.3}$$

Which yelds:

$$J_{i,m} = -\sum_{k=1}^{r_i} \left[\frac{\partial R_{s(i,k)}}{\partial i_m} \left(\sum_{j=1}^{n} C_{s(i,k),j} i_j \right) + R_{s(i,k)} \left(\sum_{j=1}^{n} C_{s(i,k),j} \frac{\partial i_j}{\partial i_m} \right) \right] \tag{4.2.4}$$

$$\frac{\partial i_j}{\partial i_m} = \begin{cases} 0 & \text{if} \quad j \neq m \\ 1 & \text{if} \quad j = m \end{cases} \tag{4.2.5}$$

$$\frac{\partial R_s(i,k)}{\partial i_m} = \begin{cases} 0 & \text{if } R_s(i,k) \text{ is a contact resistance} \\ A_1 & \text{if } R_s(i,k) \text{ is a longitudinal resistance} \\ A_2 & \text{if } R_s(i,k) \text{ is an interelements resistance} \end{cases} \tag{4.2.6}$$

If the resistance of the k^{th} branch of the i^{th} fundamental loop $R_s(i,k)$ is a longitudinal resistance, we need to address the dependence of that resistance on the interelements resistances connected to the k^{th} branch of the i^{th} fundamental loop. Using the definition of the longitudinal resistance 4.1.1, the power law (2.1.1) and (4.1.4) we can write:

$$A_1 = \frac{\partial R_{long,i}}{\partial i_m} \tag{4.2.7}$$

$$R_{long,i} = \frac{E_c}{J_c} \left(\frac{J^*_{long,i}}{J_c} \right)^{(n-1)} \frac{L_{long}}{A_{long}} \tag{4.2.8}$$

$$\begin{aligned}
\frac{\partial R_{long,i}}{\partial i_m} &= \frac{E_c}{J_c}\frac{L_{long}}{A_{long}}(n-1)\left(\frac{J^*_{long,i}}{J_c}\right)^{(n-2)}\frac{1}{J_c}\frac{\partial J^*_{long,i}}{\partial i_m} \\
&= \frac{E_c}{J_c}\frac{L_{long}}{A_{long}}(n-1)\left(\frac{J^*_{long,i}}{J_c}\right)^{(n-2)}\frac{1}{J_c}\left(\left(\frac{I_{long,i}}{A_{long}}\right)^2+\left(\frac{\sum_{i=1}^{F} I_{inter,i}}{A_{inter}}\right)^2\right)^{-\frac{1}{2}} \\
&\quad \left(\frac{1}{A^2_{long}}\frac{\partial I_{long,i}}{\partial i_m}+\frac{1}{(FA_{inter})^2}\sum_{i=1}^{F}\frac{\partial I_{inter,i}}{\partial i_m}\right) \\
&= \frac{E_c}{J_c}\frac{L_{long}}{A_{long}}(n-1)\left(\frac{J^*_{long,i}}{J_c}\right)^{(n-3)}\frac{1}{J_c^2}\left(\frac{1}{A^2_{long}}\frac{\partial I_{long,i}}{\partial i_m}+\frac{1}{(FA_{inter})^2}\sum_{i=1}^{F}\frac{\partial I_{inter,i}}{\partial i_m}\right) \\
&= K_{long}\left(\frac{J^*_{long,i}}{J_c}\right)^{(n-3)}\frac{1}{J_c^2}\left(\frac{1}{A^2_{long}}\frac{\partial I_{long,i}}{\partial i_m}+\frac{1}{(FA_{inter})^2}\sum_{i=1}^{F}\frac{\partial I_{inter,i}}{\partial i_m}\right) \\
&= F_{long,i}\left(\frac{1}{A^2_{long}}\frac{\partial I_{long,i}}{\partial i_m}+\frac{1}{(FA_{inter})^2}\sum_{i=1}^{F}\frac{\partial I_{inter,i}}{\partial i_m}\right)
\end{aligned} \tag{4.2.9}$$

Where K_{long} is a constant in common to all the longitudinal resistances, and $F_{long,i}$ is a function of $(J^*_{long,i})$. The same treatment of (4.2.9) can be applied to the interelements resistances, which yields:

$$A_2 = \frac{\partial R_{inter,i}}{\partial i_m} = F_{inter,i}\left(\frac{1}{A^2_{inter}}\frac{\partial I_{inter,i}}{\partial i_m}+\frac{1}{(SA_{long})^2}\sum_{i=1}^{S}\frac{\partial I_{long,i}}{\partial i_m}\right) \tag{4.2.10}$$

$$F_{inter,i} = \frac{E_c}{J_c}\frac{L_{inter}}{A_{inter}}(n-1)\left(\frac{J^*_{inter,i}}{J_c}\right)^{(n-3)}\frac{1}{J_c^2} \tag{4.2.11}$$

All the $I_{int,i}$ are cotree currents, so that (4.2.5) can be applied. The $I_{long,i}$ can either be cotree or tree currents if the latter they have to be expressed as a combination of cotree current and then employ (4.2.5).

The results obtained from the code are also compared to the experimental data presented in [170]. The tape and transport current data are in Table 4.2.3. To assess the losses in the low transport current regime $I_m < 0.2I_c$ the number of subelements needs to be increased. The comparison of the losses is presented in Figs. 4.2.7 and 4.2.8. The percentage error between the circuit model results and the experimental data is shown in Fig. 4.2.9.

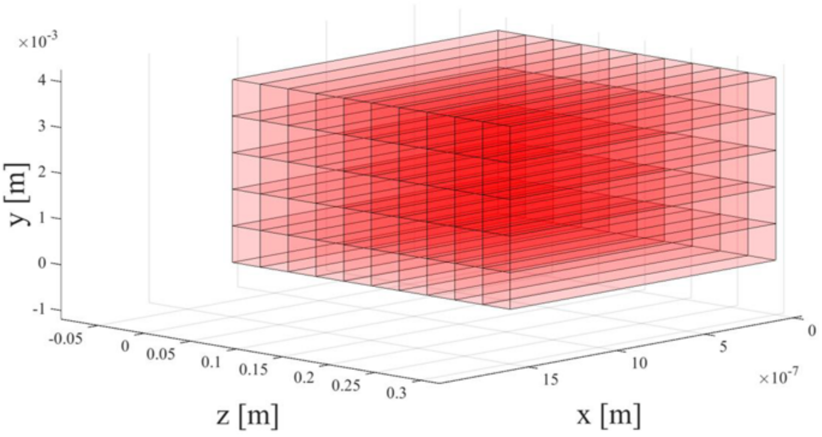

Figure 4.2.1: *Visual representation of the discretization of the superconducting layer of the tape with $N_s = 5$, $N_d = 10$. Each element in figure, is represented by a circuit element as the one in* Fig. 4.1.2

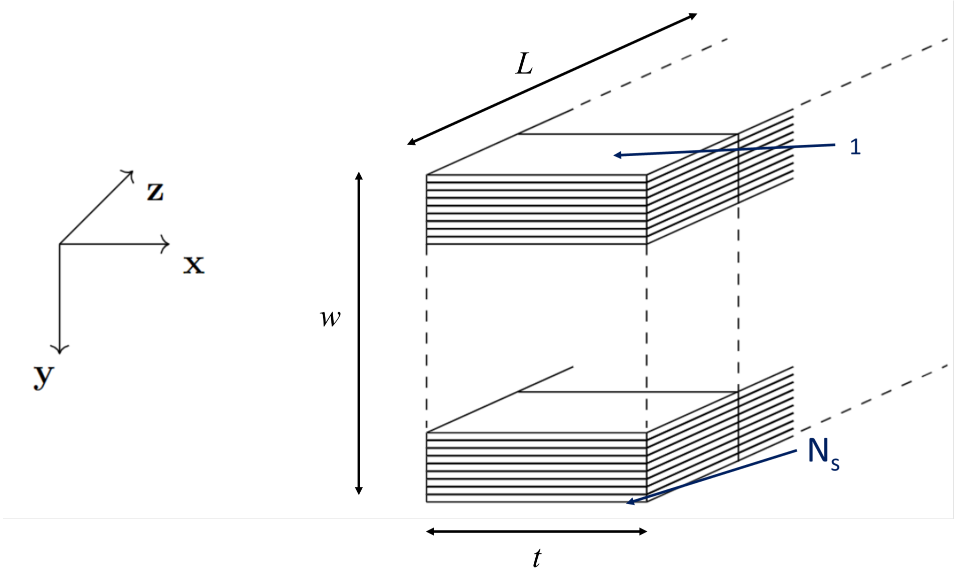

Figure 4.2.2: *Sketch of a tape divided into subelements. In the figure the subelements number 1 and N_s are indicated.*

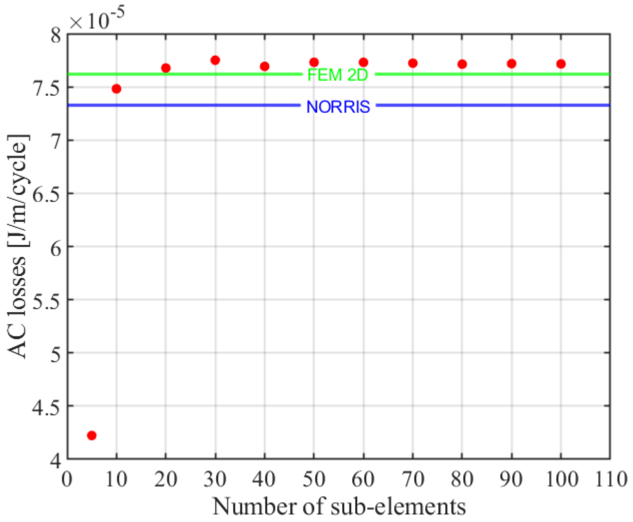

Figure 4.2.3: *Dependence of the AC losses of the tape on the number of sub-elements (N_s), with a fixed number of longitudinal elements ($N_d = 5$). The dotted lines represent respectively the results obtained with the Norris formula and the 2D FEM model.*

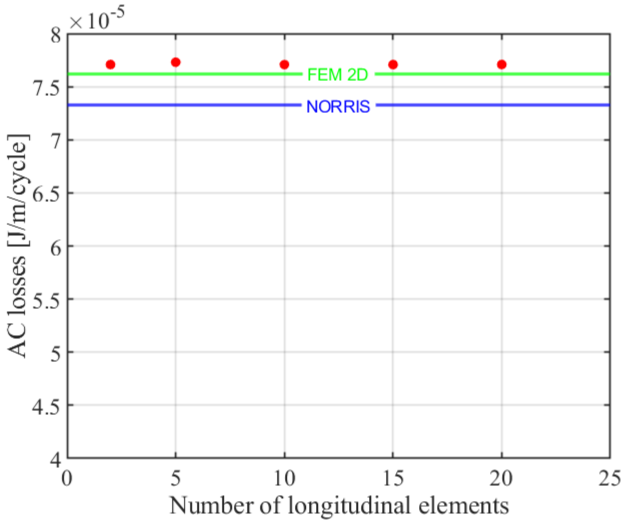

Figure 4.2.4: *Dependence of the AC losses of the tape on the number of longitudinal elements (N_d), with a fixed number of subelements ($N_s = 60$). The dotted lines represent respectively the results obtained with the Norris formula and the 2D FEM model.*

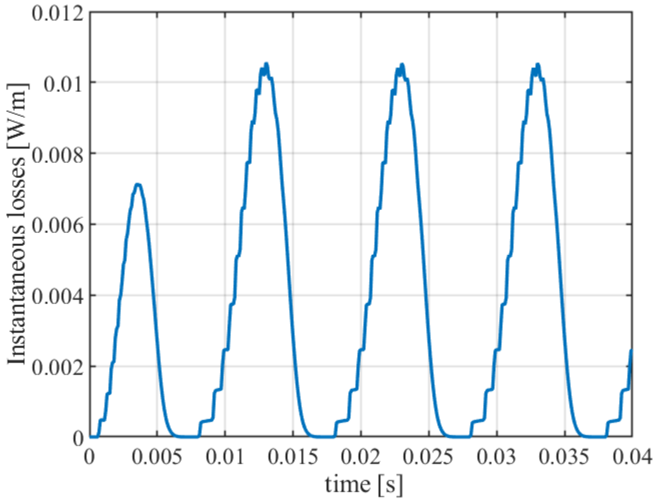

Figure 4.2.5: *Instantaneous power losses of an individual YBCO tape subjected to a sinusoidal transport current. The discretization of the tape employed is with* $N_s = 100$, $N_d = 5$, *and* $N_t = N_l = 1$. *Increasing the number of sub-elements allows one to smooth the curve.*

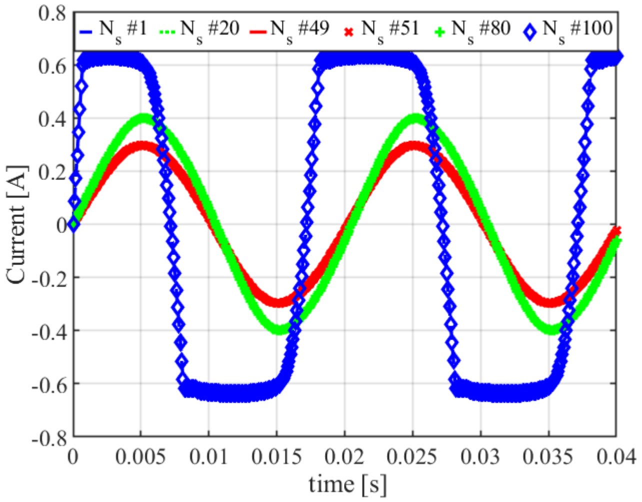

Figure 4.2.6: *Currents in various sub-elements of the first longitudinal element of the tape. The superposition of the curves shows symmetry in the current distribution. The Current in the sub-elements on the edges of the tape is higher than the one in the middle. Simulation performed with* $N_d = 5$ *and* $N_s = 100$.

Table 4.2.3: Tape and current parameters of experimental results

Tape Length (L)	0.1 m	J_c	$4.034 \times 10^{10}\ A/m^2$
Thickness sc. layer (t)	1.5 μm	Tape width (w)	4 mm
frequency	50 Hz	I_c	242 A
n-index	43	Peak current (I_m)	23 - 208 A

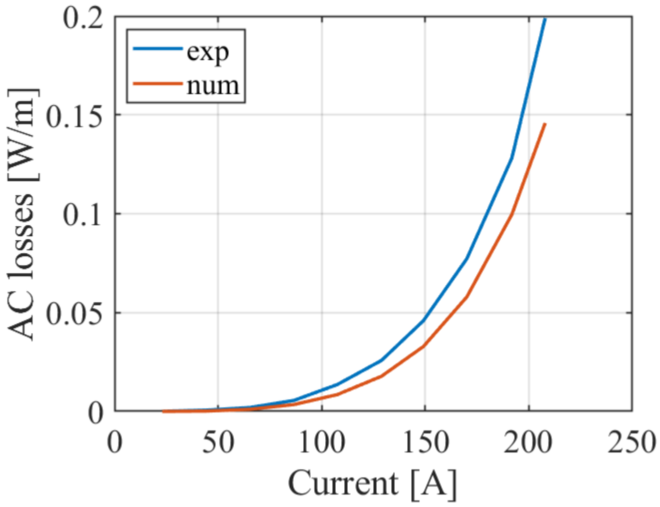

Figure 4.2.7: *Comparison of the AC losses, as the average power dissipated in a cycle, between experimental data and the circuit model.*

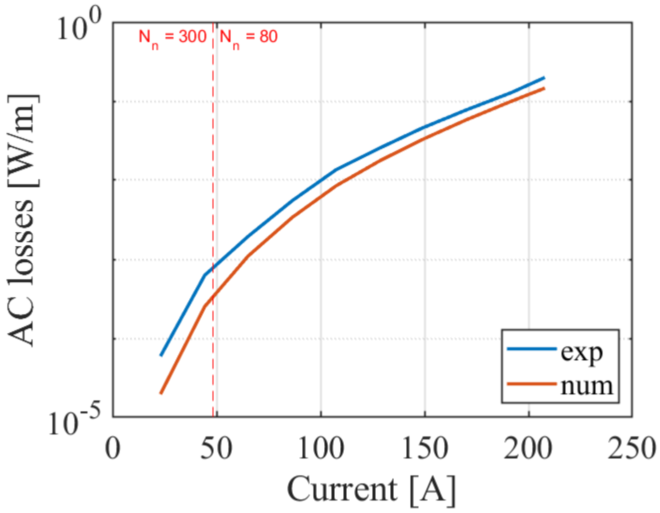

Figure 4.2.8: *Comparison of the AC losses, as the average power dissipated in a cycle, between experimental data and the circuit model.*

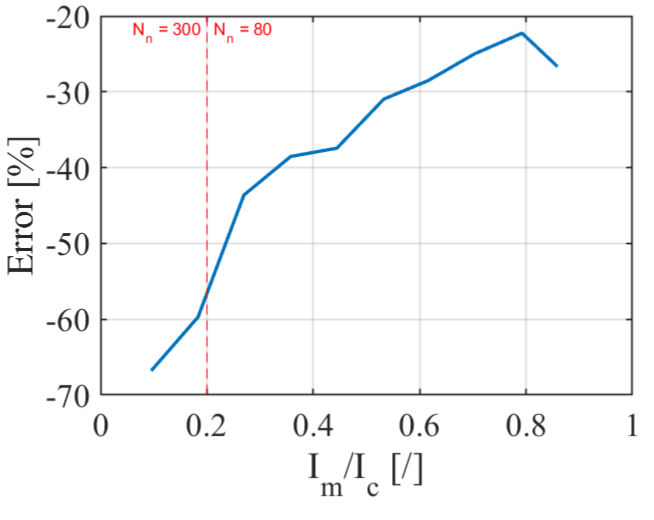

Figure 4.2.9: *Percentage error between the experimental data and the circuit model results. In the region where the peak current is below* $0.2I_c$ *the number of subelements is increased to correctly evaluate the losses.*

4.2.2 Frequency investigation of losses

The circuit model was also applied to simulate the AC losses in a 12 mm Superpower YBCO tape, whose main data are reported in Table 4.2.4, at different frequencies and amplitudes of the sinusoidal transport current. The AC losses of this tape were measured in the laboratories of RSE spa and are compared to the results of the model developed. As for the previous case study, two periods were evaluated. For starter, the results of the circuit model are compared with the Norris formula, and shown in Fig. 4.2.10. A good agreement between the analytical and numerical results is found even in these operating conditions. To reach convergence with this wider tape, the number of sub-elements used was accordingly scaled. This means that at least 150 subelements have to be introduced in the discretization to correctly simulate the effect of the screening currents. In these simulations the number of subelements was set to 180. In Fig. 4.2.11 the AC losses are presented in a linear scale to better emphasize the differences, as can be seen, the circuit model perfectly reproduces the results of the FEM model.

Table 4.2.4: Parameters Superpower Tape

L	0.17 m	J_c	2.75 $\times 10^{10}$ A$/m^2$
t	1.5 μm	w	12 mm
E_c	100 $\mu V/m$	n-index	32

The differences between the analytical formula and the circuit model change depending on both the frequency and the transport current, but stay in good agreement as shown in table 4.2.5. A very good agreement is found between the FEM model and the circuit model as shown in table 4.2.6. Also, in this case, the circuit model results faster than the FEM model. The circuit model requires a total computation time of 68 s for the evaluation of the AC losses in the case of $I_m/I_c = 0.7$ at 50 Hz, (where I_m is the amplitude of the transport current), while the FEM model requires a total of 1231 s.

The comparisons between the experimental results for AC losses and the numerical results predicted by the circuit model are shown in Fig. 4.2.12. The error between the two sets of results is reported in Fig. 4.2.13. There is a good agreement between the two data sets, the relative error decreases as the transport current approaches the critical current.

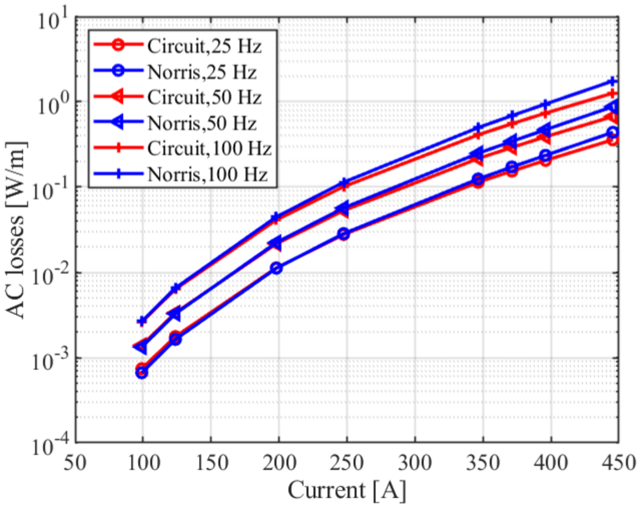

Figure 4.2.10: AC losses (in terms of average power dissipated in a cycle) as a function of both transport current and frequency. Results from a simulation with $N_d = 5$ and $N_s = 180$, the number of sub-elements is increased due to convergence requirements.

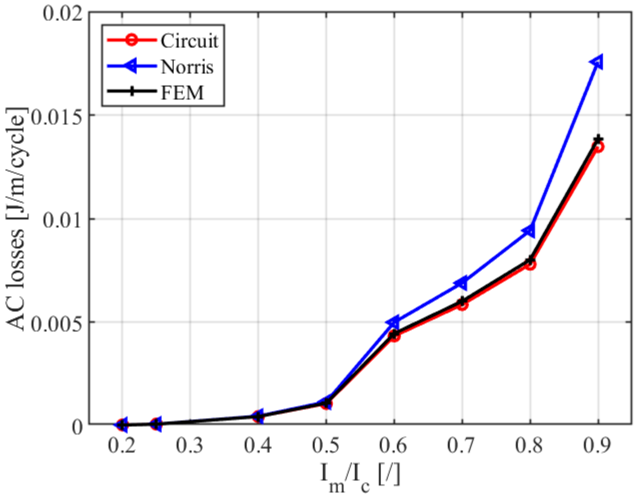

Figure 4.2.11: Comparison of the AC losses at 50 Hz, between the three formulations employed.

Table 4.2.5: Percentage difference circuit model vs analytical formula

I_m/I_c \ Frequency	25 Hz	50 Hz	100 Hz
0.2	-11.4%	-4.9%	1.8%
0.25	-7.8%	-2.2%	2.9%
0.4	-9.8%	3.43%	7.7%
0.5	2.36%	6.8%	10.9%
0.6	8.6%	13.2%	17.6%
0.7	10.4%	15.1%	19.5%
0.8	12.5%	17.3%	21.7%
0.9	18.2%	23.3%	27.9%

Table 4.2.6: Percentage difference circuit model vs FEM at 50 Hz

I_m/I_c	*difference [%]*
0.2	-10.4
0.25	-4.9
0.4	3.1
0.5	1.6
0.6	2.6
0.7	2.6
0.8	2.7
0.9	2.6

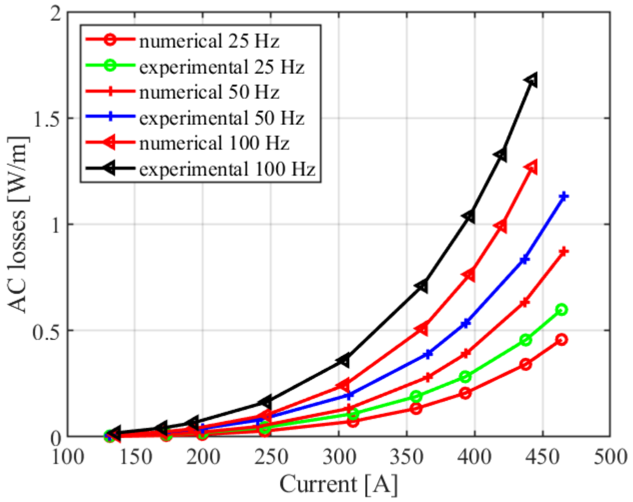

Figure 4.2.12: Comparison of the AC losses, at several frequencies Hz, derived from the circuit model and the experimental measures.

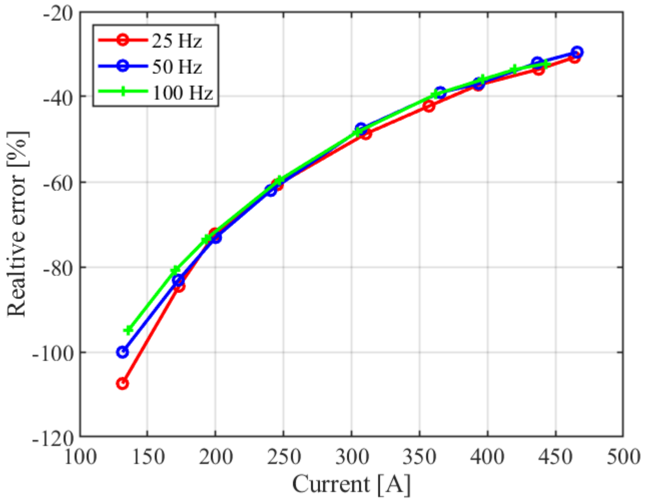

Figure 4.2.13: Relative percentage error between the circuit model and the experimental data presented in Fig. 4.2.12.

4.3 Circuit model applied to coils

After demonstrating the validity of the solving method of the developed code, and demonstrating that the results obtained are in agreement with those of other validated formulations, the circuit model was used to study a NI-HTS coil. The parameters of the coil are reported in Table 4.3.1, the discretization employed is with $N_d = 2$, so every half turn a contact resistance between layers is placed, and $N_s = 50$ (the tape is divided into fifty subelements). The equivalent circuit of the coil is shown in Fig. 4.3.1.

Table 4.3.1: Simulation Parameters NI-HTS coil

Tape Length (L)	2.51 m	J_c	10^{10} A/m^2
Thickness sc. layer (t)	1.5 μm	Tape width (w)	4 mm
frequency	50 Hz	I_c	60 A
n-index	43	Peak current (I_m)	42 A
E_c	100 $\mu V/m$	Simulation time	0.04 s
Tape thickness	150 μm	R_c	0.5 $m\Omega$

The total AC losses amount to $2.53 \times 10^{-6}[J/cycle/m]$, nearly 78% of which are caused by the dissipation in the contact resistances, while the rest occurs in the superconducting material, specifically due to the longitudinal resistances. The losses in the interelements resistances, so due to the dissipation during the current redistribution in the tape, are negligible.

Table 4.3.2: Results simulation NI-HTS coil

Peak instantaneous losses	2.58×10^{-4} W/m
Total AC losses	2.53×10^{-6} J/m/cycle
AC losses of R_{con}	1.97×10^{-6} J/m/cycle
AC losses of R_{long}	5.62×10^{-7} J/m/cycle
AC losses of R_{inter}	5.56×10^{-20} J/m/cycle

The behavior of some of the longitudinal, transversal, and interelements currents of the first layer of the first sub-element is shown in Fig. 4.3.2. The longitudinal currents are much higher than both the transversal and the interelements ones. The transversal currents, flowing along the contact resistances, are plotted in Fig. 4.3.3, while the interelements ones are in Fig. 4.3.4 and Fig. 4.3.5. The

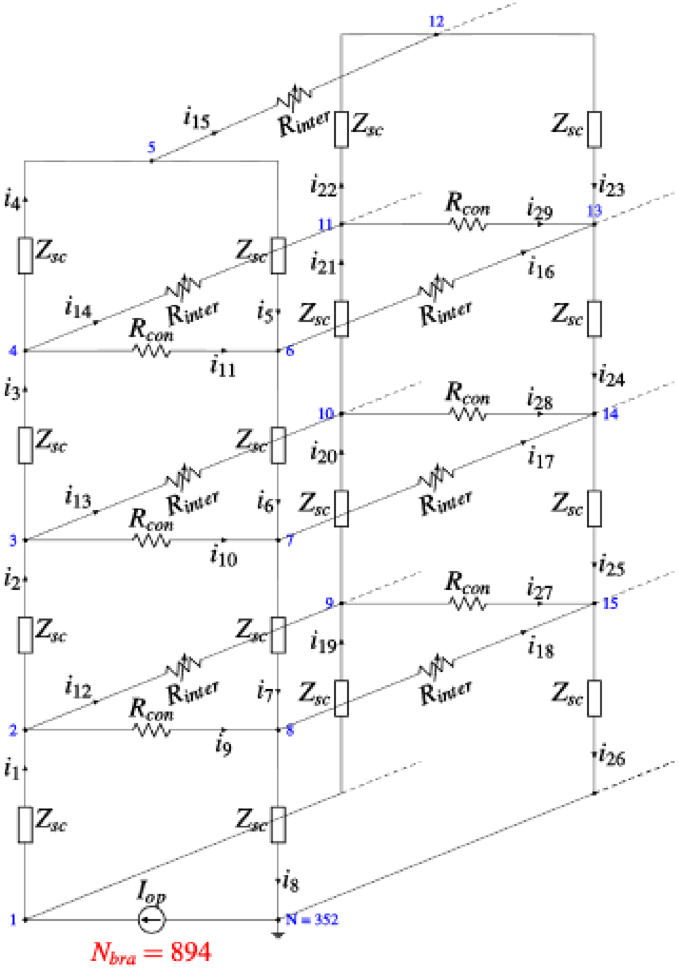

Figure 4.3.1: Part of the equivalent circuit of the NI-HTS coil simulated, the numbers of the currents match those of the components.

currents in the contact resistances have a phase shift compared to those in the longitudinal resistances. This current is flowing due to the inductive effects in the longitudinal branches. The counter-electromotive force arising in the longitudinal inductors is forcing the current to flow on the contact resistances generating a noticeable power dissipation.

The simulation of two periods (0.04 s) takes 4 hours and 24 minutes, of which 1 hour and 5 minutes for the computation of the inductance matrix. The computation of the inductance matrix can be done only once if the geometry of the coil studied does not change.

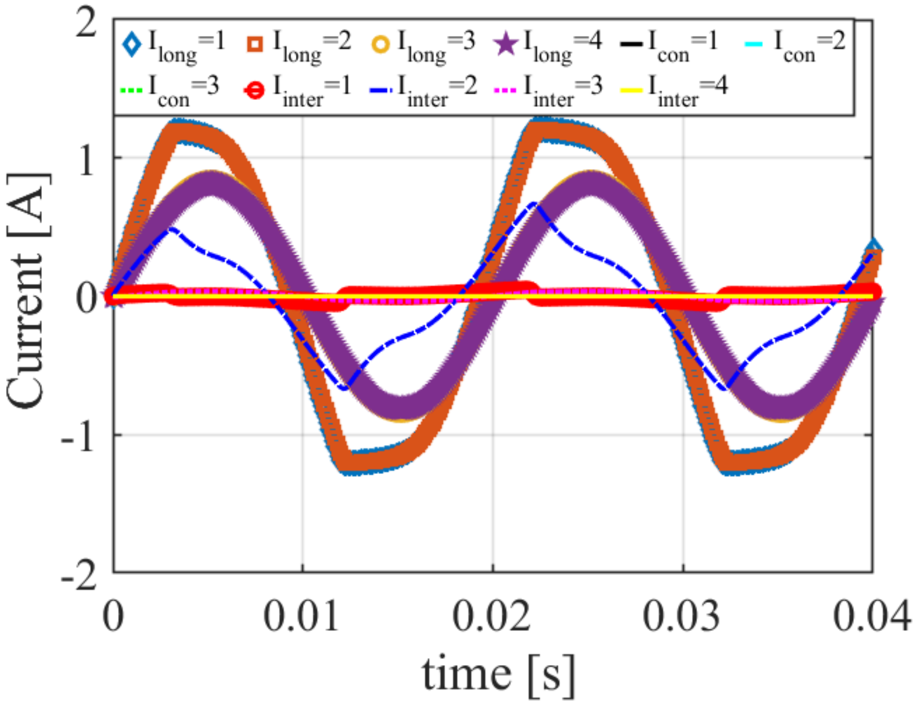

Figure 4.3.2: *Behavior in time of the longitudinal and transversal currents in the first layer of the first sub-element of the coil, and the interelements currents between the first layer of the first sub-element and the first layer of the second sub-element.*

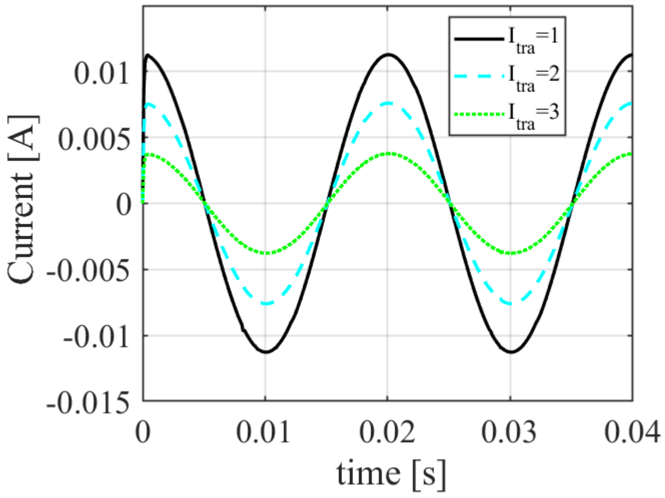

Figure 4.3.3: *Enlarged view of the transversal currents in Fig. 4.3.2.*

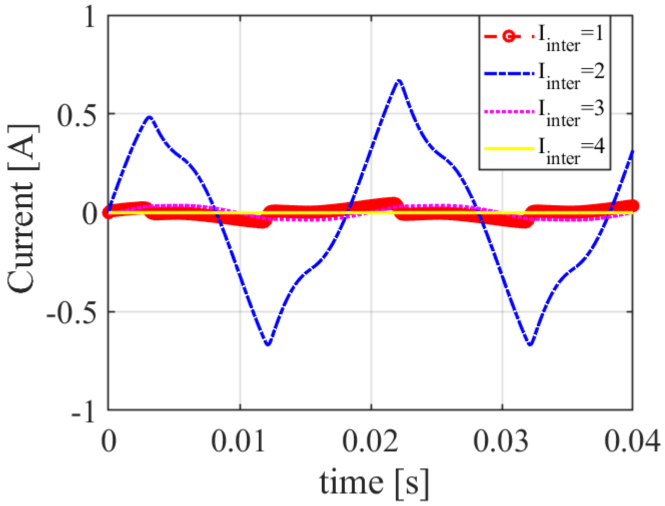

Figure 4.3.4: *Enlarged view of the interelements currents in Fig. 4.3.2.*

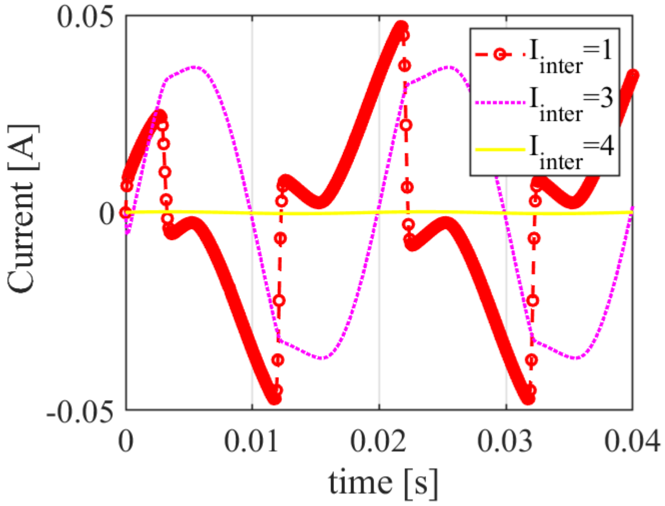

Figure 4.3.5: *Zoom of Fig. 4.3.4*

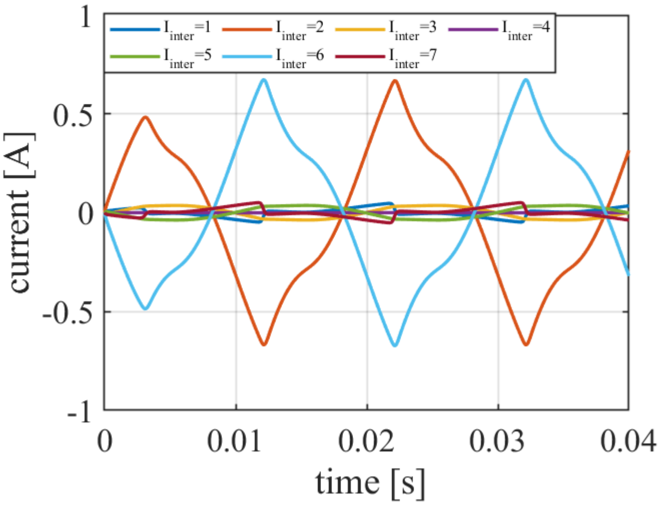

Figure 4.3.6: interelements currents of the first subelement.

In Fig. 4.3.2 the label $I_{long} = x$ means that the longitudinal current plotted belongs to the x^{th} longitudianl components, the same for the contact and interelements currents. In Fig. 4.3.2, only the longitudinal and interelements currents of the first layer are plotted. Due to the symmetry of the problem, the longitudinal currents in the second layer are the same, while the interelements currents are the same with a changed sign. All the interelements currents of the first subelement are shown in Fig. 4.3.6. The longitudinal currents in the first subelement are plotted in Fig. 4.3.7. In Fig. 4.3.4 is possible to see that the current redistribution along the width of the tape mainly occurs at the end of the first turn ($I_{inter} = 2$ corresponds to the current labeled i_{23} in Fig. 4.3.1). In Fig. 4.3.8 and Fig. 4.3.9 the behavior in time of the longitudinal resistances of the first subelement, while in Fig. 4.3.10 the interelements resistances.

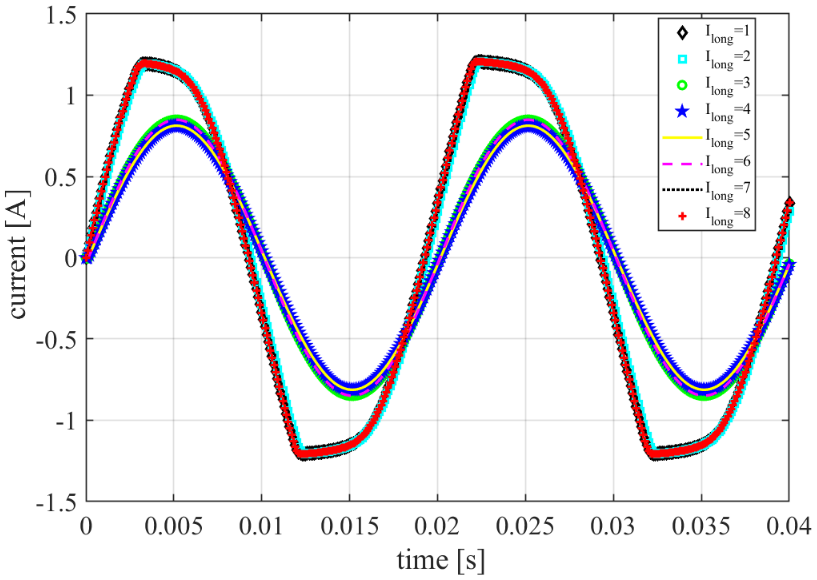

Figure 4.3.7: Longitudinal currents of the first subelement.

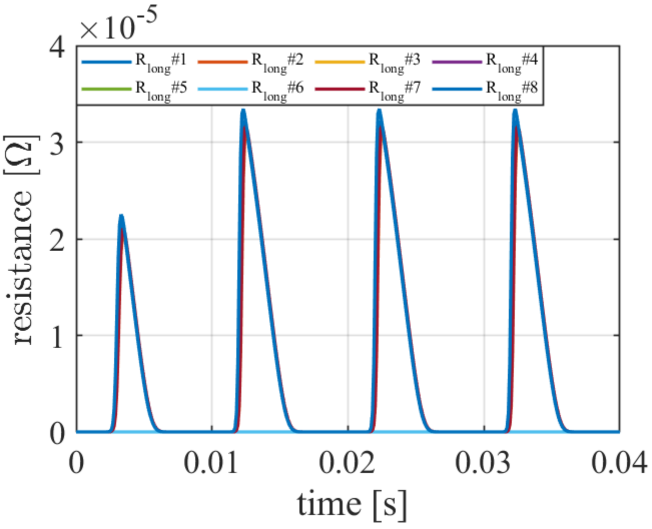

Figure 4.3.8: Longitudinal resistances the first subelement.

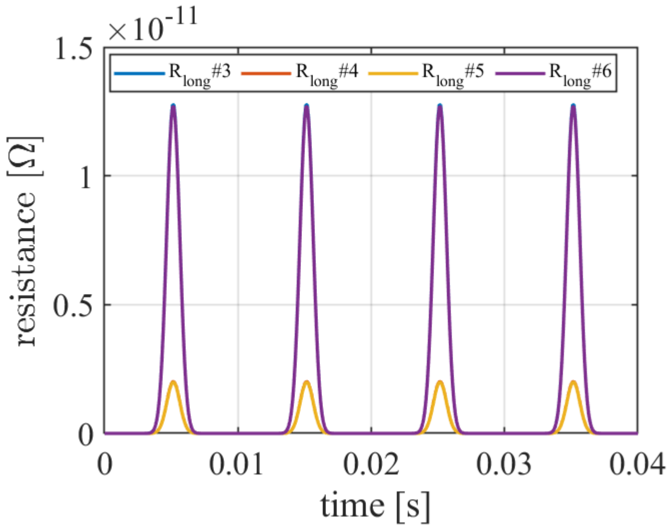

Figure 4.3.9: Longitudinal Resistances of circuit elements number 3 to 6. Essentially an enlarged view of some of the currents in Fig. 4.3.8

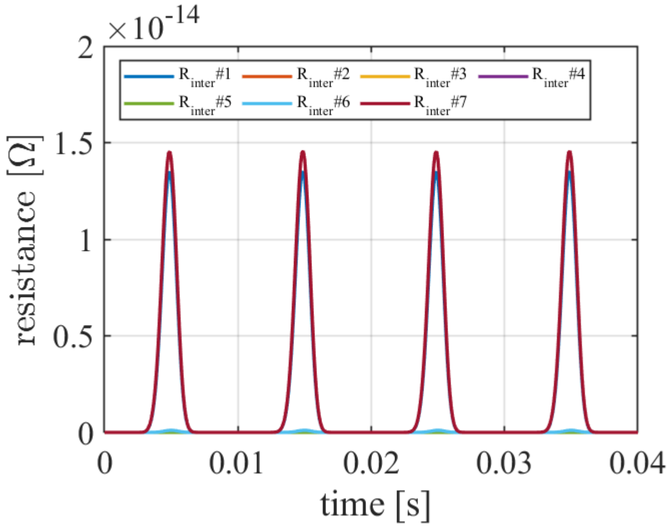

Figure 4.3.10: interelements resistances of the first subelement. The resistances of the interelements elements 2 to 6 are several orders of magnitudes lower than those of the interelements elements 1 and 7.

4.4 Final considerations on the circuit model

This thesis presents the development of a versatile circuit model for the analysis of both insulated and non insulated superconducting coils. The model's adaptability extends beyond coil geometries (both insulated and non-insulated), making it applicable to straight tapes, tape stacks, and various configurations with minor modifications to the circuit topology while maintaining the underlying code structure. This chapter delves into the essential considerations for model development, encompassing the representation of discretized device components using circuit elements and various approaches for circuit analysis. Notably, a promising solution strategy, not covered in this chapter but under ongoing investigation, involves a fusion of the state equation method and the current loops method. This integration could eliminate the need for parallel resistances (see Fig. 4.1.8) and the emergence of algebraic loops in a differential system of equations (see section 4.1.3). A hallmark of this model lies in its ability to accurately compute screening currents within the tape and their impact on AC losses. The importance of the screening currents can be seen in Fig. 4.3.2 where the current flowing along the width of the tape in particular regions, is comparable with the longitudinal currents. The model's efficacy has been successfully demonstrated through comparison with an analytical formula and a 2D FEM model in various case studies involving a single straight tape. The comparison outcomes affirm the model's accurate loss evaluation, validating the feasibility of a circuital model approach for tape analysis. Furthermore, the circuit model albeit being a 3D representation of the tape was capable of performing simulation faster, and with the same accuracy, as a 2D FEM model. Moreover, the model has been successfully applied to analyze a small NI HTS layer-wound coil. Ongoing validation efforts will involve comparing the circuit model to FEM models and experimental data. As of now, the proposed model is a nonlinear electrical circuit incorporating non-thermal behavior. Future investigations will focus on establishing a suitable coupling between the circuit model and a thermal model of the coil.

5 *Conclusions*

This thesis presents a comprehensive review of the established analytical and numerical models proposed in the literature for studying high-temperature superconducting (HTS) devices. Following a careful evaluation of the solutions available in the literature, this work is focused on developing rapid alternatives to the computing demanding finite element method (FEM) models for analyzing complex HTS devices.

The first outcome of the work is a series of analytical formulae that significantly broaden the applicability range of existing formulae. The utility of this novel formulation lies in its ability to provide analytical expressions for assessing the instantaneous power losses resulting from the synergistic action of both an applied current and an external magnetic in a superconducting slab. The formulae proposed can be applied to generic cycles of transport current and magnetic field, provided that they are in phase with each other. The new formulae were validated by comparison with 1D and 2D FEM models. Along with these formulae, a technique for applying the findings developed to the intricate geometry of twisted stacked tapes has been investigated, leading to the concept of "substitutive stacks". Both the developed formulae and the substitutive stacks method have been integrated into a framework capable of providing a qualitative assessment of instantaneous losses in large-scale magnet geometries. The framework has been utilized to analyze the losses in a HTS insert of the DEMO central solenoid.

While the developed analytical formulae are currently restricted to scenarios where the transport current and magnetic field are in phase, the underlying methodology employed to derive them has the potential to determine new formulae that extend beyond this limitation. This potential was realized by deriving a new formula specifically for the case where the magnetic field becomes null while the transport current is still decreasing during a ramp-down operation. This formula was successfully validated against a 1D FEM model, demonstrating the robustness of the proposed methodology. However, the critical parameter, the magnetic field of electric penetration, cannot be solely determined from geometric considerations. The magnetic field of electric penetration is highly dependent on the specific case study, implying that a globally applicable and compact analytical formulation is not currently feasible.

The second significant achievement of the thesis is the development of a nonlinear, nonplanar lumped parameters circuit model specifically tailored for the study of HTS devices, with a particular focus on non insulated HTS coils. The distinguishing feature of this circuit model lies in its capacity to accurately assess the magnetization currents originating within the superconducting tape as well as the radial currents flowing from turn to turn.

A comprehensive study was conducted on the most suitable solution methods for the developed circuit model. This study meticulously evaluated the strengths and weaknesses of each method. The accuracy of the circuit model in assessing magnetization currents within superconducting tapes was validated through rigorous comparison against the findings of analytical formulae and a previously experimentally validated 2D FEM model. These comparisons were conducted across a range of superconducting tapes, varying in width and critical current, encompassing diverse transport current amplitudes and frequencies from 25 Hz to 100 Hz. The circuit model demonstrated a remarkable computational efficiency, achieving significant speedup compared to the 2D FEM model without compromising accuracy. This finding underscores the potential of the circuit model as a viable alternative for computationally demanding HTS studies. An NI-HTS coil geometry was investigated. The model successfully predicts the current redistribution between the coil layers and within the tapes composing it, thus enabling the evaluation of the instantaneous power dissipation.

The developed circuit model is not confined to coil geometries, as evidenced by the successful application to tape studies. Its applicability can even extend to stacked tapes, Roebel cables, CORC cables, CROCO cables and other configurations.

References

[1] D. Van Delft and P. Kes, “The discovery of superconductivity,” *Physics today*, vol. 63, no. 9, pp. 38–43, 2010.

[2] R. G. Sharma, *Superconductivity: Basics and applications to magnets*, vol. 214. Springer Nature, 2021.

[3] A. Musso, “Analysis of electrodynamic transients in high temperature superconducting tapes and coils,” 2021.

[4] `https://www.superpower-inc.com/specification.aspx`.

[5] W. Goldacker, F. Grilli, E. Pardo, A. Kario, S. I. Schlachter, and M. Vojenčiak, “Roebel cables from rebco coated conductors: a one-century-old concept for the superconductivity of the future,” *Superconductor Science and Technology*, vol. 27, no. 9, p. 093001, 2014.

[6] M. Takayasu, L. Chiesa, L. Bromberg, and J. Minervini, “Cabling method for high current conductors made of hts tapes,” *IEEE transactions on applied superconductivity*, vol. 21, no. 3, pp. 2340–2344, 2010.

[7] N. Bykovsky, D. Uglietti, K. Sedlak, , R. Wesche, and P. Bruzzone, “Stacked-tape hts conductors for fusion magnets.” `https://indico.cern.ch/event/445667/contributions/2564547/attachments/1515841/2365587/Tue-Af-Po2.08-02_STACKED-TAPE_HTS_CONDUCTORS_FOR_FUSION_MAGNETS.pdf`. presented at the 25th International Conference on Magnet Technology (MT25), 27 Aug.-1 Sep. 2017, Amsterdam (The Netherlands).

[8] M. J. Wolf, W. H. Fietz, C. M. Bayer, S. I. Schlachter, R. Heller, and K.-P. Weiss, “Hts croco: A stacked hts conductor optimized for high currents and long-length production,” *IEEE Transactions on Applied Superconductivity*, vol. 26, no. 2, pp. 19–24, 2016.

[9] S. Ito, N. Yusa, N. Yanagi, H. Tamura, A. Sagara, and H. Hashizume, “Mechanical and electrical characteristics of a bridge-type mechanical lap joint of hts stars conductors,” *IEEE Transactions on Applied Superconductivity*, vol. 26, no. 2, pp. 1–10, 2016.

[10] Y. Wang, S. Baasansuren, C. Xue, and T. Hasegawa, “Development of a quasi-isotropic strand stacked by 2g wires,” *IEEE Transactions on Applied Superconductivity*, vol. 26, no. 4, pp. 1–6, 2016.

[11] T. Mulder, A. Dudarev, M. Mentink, H. Silva, D. Van Der Laan, M. Dhallé, and H. Ten Kate, "Design and manufacturing of a 45 ka at 10 t rebco-corc cable-in-conduit conductor for large-scale magnets," *IEEE transactions on applied superconductivity*, vol. 26, no. 4, pp. 1–5, 2016.

[12] S. Hahn, K. Radcliff, K. Kim, S. Kim, X. Hu, K. Kim, D. V. Abraimov, and J. Jaroszynski, "'defect-irrelevant'behavior of a no-insulation pancake coil wound with rebco tapes containing multiple defects," *Superconductor Science and Technology*, vol. 29, no. 10, p. 105017, 2016.

[13] K.-H. Müller, "Ac losses in stacks and arrays of ybco/hastelloy and monofilamentary bi-2223/ag tapes," *Physica C: Superconductivity*, vol. 312, no. 1-2, pp. 149–167, 1999.

[14] B. Rozier, *Contribution to electromagnetic and thermal modelling of High Temperature Superconducting REBCO coils for protection purpose.* PhD thesis, Université Grenoble Alpes, 2019.

[15] N. Amemiya, S. Sato, and T. Ito, "Magnetic flux penetration into twisted multifilamentary coated superconductors subjected to ac transverse magnetic fields," *Journal of applied physics*, vol. 100, no. 12, 2006.

[16] J. R. Clem, J. Claassen, and Y. Mawatari, "Ac losses in a finite z stack using an anisotropic homogeneous-medium approximation," *Superconductor Science and Technology*, vol. 20, no. 12, p. 1130, 2007.

[17] E. Pardo, "Calculation of ac loss in coated conductor coils with a large number of turns," *Superconductor Science and Technology*, vol. 26, no. 10, p. 105017, 2013.

[18] E. Berrospe-Juarez, F. Trillaud, V. M. Zermeño, and F. Grilli, "Advanced electromagnetic modeling of large-scale high-temperature superconductor systems based on h and ta formulations," *Superconductor Science and Technology*, vol. 34, no. 4, p. 044002, 2021.

[19] A. Macchiagodena, M. Breschi, D. Buonafine, G. De Marzi, and L. Savoldi, "Analytical modeling of magnetization losses in twisted stacked hts conductors," *IEEE Transactions on Applied Superconductivity*, vol. 33, no. 5, pp. 1–5, 2023.

[20] A. Macchiagodena, M. Breschi, G. De Marzi, F. Grilli, and L. Savoldi, "Analytical formulae for hysteresis power loss in twisted stacked hts cables," *IEEE Transactions on Applied Superconductivity*, vol. 34, no. 3, pp. 1–5, 2024.

[21] M. Breschi, A. Macchiagodena, P. L. Ribani, A. Musso, G. Angeli, and M. Bocchi, "Circuit model of interlayer and screening currents in layer-wound ni hts coils," *IEEE Transactions on Applied Superconductivity*, vol. 34, no. 3, pp. 1–5, 2024.

[22] V. Z. Kresin and S. A. Wolf, *Fundamentals of superconductivity.* Springer Science & Business Media, 2013.

[23] M. G. Hadlow, J. Baylis, and B. Lindley, "Superconductivity and its applications to power engineering," in *Proceedings of the Institution of Electrical Engineers*, vol. 119, pp. 1003–1032, IET, 1972.

[24] M. D. Licker, *McGraw-Hill concise encyclopedia of physics.* McGraw-Hill Companies, 2005.

[25] J. Bardeen, "Theory of the meissner effect in superconductors," *Physical Review*, vol. 97, no. 6, p. 1724, 1955.

[26] E. H. Brandt, "The flux-line lattice in superconductors," *Reports on Progress in Physics*, vol. 58, no. 11, p. 1465, 1995.

[27] K. P. Thakur, A. Raj, E. H. Brandt, J. Kvitkovic, and S. V. Pamidi, "Frequency-dependent critical current and transport ac loss of superconductor strip and roebel cable," *Superconductor Science and Technology*, vol. 24, p. 065024, apr 2011.

[28] R. Zhang, P. Gao, and X. Wang, "Strain dependence of critical superconducting properties of nb3sn with different intrinsic strains based on a semi-phenomenological approach," *Cryogenics*, vol. 86, pp. 30–37, 2017.

[29] J. Guo, Q. Wu, and L. Sun, "Advanced high-pressure transport measurement system integrated with low temperature and magnetic field," *Chinese Physics B*, vol. 27, no. 7, p. 077402, 2018.

[30] J. N. Rjabinin and L. Shubnikow, "Magnetic properties and critical currents of supra-conducting alloys," *Nature*, vol. 135, no. 3415, pp. 581–582, 1935.

[31] V. L. Ginzburg, "On the theory of superconductivity," *Il Nuovo Cimento (1955-1965)*, vol. 2, pp. 1234–1250, 1955.

[32] A. A. Abrikosov, "The magnetic properties of superconducting alloys," *Journal of Physics and Chemistry of Solids*, vol. 2, no. 3, pp. 199–208, 1957.

[33] L. Cooley, A. Ghosh, and R. Scanlan, “Costs of high-field superconducting strands for particle accelerator magnets,” *Superconductor Science and Technology*, vol. 18, no. 4, p. R51, 2005.

[34] M. Parizh, Y. Lvovsky, and M. Sumption, “Conductors for commercial mri magnets beyond nbti: requirements and challenges,” *Superconductor Science and Technology*, vol. 30, no. 1, p. 014007, 2016.

[35] L. Bottura, G. De Rijk, L. Rossi, and E. Todesco, “Advanced accelerator magnets for upgrading the lhc,” *IEEE Transactions on Applied Superconductivity*, vol. 22, no. 3, pp. 4002008–4002008, 2012.

[36] J. G. Bednorz and K. A. Müller, “Possible high t c superconductivity in the ba- la- cu- o system,” *Zeitschrift für Physik B Condensed Matter*, vol. 64, no. 2, pp. 189–193, 1986.

[37] A. Strnad, C. Hempstead, and Y. Kim, “Dissipative mechanism in type-ii superconductors,” *Physical Review Letters*, vol. 13, no. 26, p. 794, 1964.

[38] F. Grilli, E. Pardo, A. Stenvall, D. N. Nguyen, W. Yuan, and F. Gömöry, “Computation of losses in hts under the action of varying magnetic fields and currents,” *IEEE Transactions on Applied Superconductivity*, vol. 24, no. 1, pp. 78–110, 2013.

[39] M. Daibo, S. Fujita, M. Haraguchi, Y. Iijima, and T. Saitoh, “Evaluation of the normal-zone propagation characteristics of rebco coated conductors with laminated cu tape,” *IEEE transactions on applied superconductivity*, vol. 21, no. 3, pp. 2428–2431, 2011.

[40] Z. Zhao and Y. Iwasa, “Normal zone propagation in adiabatic superconducting magnets part 1: Normal zone propagation velocity in superconducting composites,” *Cryogenics*, vol. 31, no. 9, pp. 817–825, 1991.

[41] O. Maruyama, T. Ohkuma, T. Masuda, M. Ohya, S. Mukoyama, M. Yagi, T. Saitoh, N. Aoki, N. Amemiya, A. Ishiyama, *et al.*, “Development of rebco hts power cables,” *Physics Procedia*, vol. 36, pp. 1153–1158, 2012.

[42] E. P. Volkov, V. S. Vysotsky, and V. P. Firsov, “First russian long length hts power cable,” *Physica C: Superconductivity and its Applications*, vol. 482, pp. 87–91, 2012.

[43] X.-Y. Xiao, Y. Liu, J.-X. Jin, C.-S. Li, and F.-W. Xu, “Hts applied to power system: Benefits and potential analysis for energy conservation and emission reduction,” *IEEE Transactions on Applied Superconductivity*, vol. 26, no. 7, pp. 1–9, 2016.

[44] S. Hahn, K. Kim, K. Kim, X. Hu, T. Painter, I. Dixon, S. Kim, K. R. Bhattarai, S. Noguchi, J. Jaroszynski, *et al.*, “45.5-tesla direct-current magnetic field generated with a high-temperature superconducting magnet,” *Nature*, vol. 570, no. 7762, pp. 496–499, 2019.

[45] Q. Wang, J. Liu, J. Zheng, J. Qin, Y. Ma, Q. Xu, D. Wang, W. Chen, T. Qu, X. Zhang, *et al.*, “Progress of ultra-high-field superconducting magnets in china,” *Superconductor Science and Technology*, vol. 35, no. 2, p. 023001, 2021.

[46] H. Maeda and Y. Yanagisawa, “Recent developments in high-temperature superconducting magnet technology,” *IEEE Transactions on applied superconductivity*, vol. 24, no. 3, pp. 1–12, 2013.

[47] D. Uglietti, “A review of commercial high temperature superconducting materials for large magnets: from wires and tapes to cables and conductors,” *Superconductor Science and Technology*, vol. 32, no. 5, p. 053001, 2019.

[48] S. Nagaya, N. Hirano, T. Katagiri, T. Tamada, K. Shikimachi, Y. Iwatani, F. Saito, and Y. Ishii, “The state of the art of the development of smes for bridging instantaneous voltage dips in japan,” *Cryogenics*, vol. 52, no. 12, pp. 708–712, 2012.

[49] J. Ciceron, A. Badel, P. Tixador, R. Pasquet, and F. Forest, “Test in strong background field of a modular element of a rebco 1 mj high energy density smes,” *IEEE Transactions on Applied Superconductivity*, vol. 28, no. 4, pp. 1–5, 2018.

[50] Y. Iwasa, “Hts and nmr/mri magnets: Unique features, opportunities, and challenges,” *Physica C: Superconductivity and its applications*, vol. 445, pp. 1088–1094, 2006.

[51] J. Bascuñán, S. Hahn, Y. Kim, and Y. Iwasa, “A new high-temperature superconducting (hts) 700-mhz insert magnet for a 1.3-ghz lts/hts nmr magnet,” *IEEE transactions on applied superconductivity*, vol. 23, no. 3, pp. 4400304–4400304, 2012.

[52] B. J. Parkinson, R. Slade, M. J. Mallett, and V. Chamritski, “Development of a cryogen free 1.5 t ybco hts magnet for mri,” *IEEE transactions on applied superconductivity*, vol. 23, no. 3, pp. 4400405–4400405, 2012.

[53] A. Labbé, G. Authelet, B. Baudouy, C. J. van Der Beek, J. Briatico, L. Darrasse, and M. Poirier-Quinot, “Recent advances and challenges in the development of radiofrequency hts coil for mri,” *Frontiers in Physics*, vol. 9, p. 705438, 2021.

[54] J. Lloberas, A. Sumper, M. Sanmarti, and X. Granados, “A review of high temperature superconductors for offshore wind power synchronous generators,” *Renewable and Sustainable Energy Reviews*, vol. 38, pp. 404–414, 2014.

[55] A. Bergen, R. Andersen, M. Bauer, H. Boy, M. t. Brake, P. Brutsaert, C. Bührer, M. Dhallé, J. Hansen, H. Ten Kate, *et al.*, “Design and in-field testing of the world’s first rebco rotor for a 3.6 mw wind generator,” *Superconductor science and technology*, vol. 32, no. 12, p. 125006, 2019.

[56] M. R. Barzegar-Bafrooei, A. Akbari Foroud, J. Dehghani Ashkezari, and M. Niasati, “On the advance of sfcl: a comprehensive review,” *IET Generation, Transmission & Distribution*, vol. 13, no. 17, pp. 3745–3759, 2019.

[57] C. A. Baldan, Y. Weijia, C. Y. Shigue, and E. Ruppert Filho, “Performance of modular sfcl using rebco coated conductor tapes under repetitive overcurrent tests,” *IEEE Transactions on Applied Superconductivity*, vol. 26, no. 3, pp. 1–5, 2016.

[58] M. Song, C. Sheng, T. Ma, Y. Huang, C. Yang, Y. Xin, H. Jin, T. Yang, J. Xiong, C. Li, *et al.*, “Current limiting tests of a prototype 160 kv/1 ka resistive dc superconducting fault current limiter,” *Superconductor Science and Technology*, vol. 34, no. 1, p. 014002, 2020.

[59] M. Takayasu, L. Chiesa, P. D. Noyes, and J. V. Minervini, “Investigation of hts twisted stacked-tape cable (tstc) conductor for high-field, high-current fusion magnets,” *IEEE Transactions on Applied Superconductivity*, vol. 27, no. 4, pp. 1–5, 2017.

[60] D. Uglietti, N. Bykovsky, K. Sedlak, B. Stepanov, R. Wesche, and P. Bruzzone, “Test of 60 ka coated conductor cable prototypes for fusion magnets,” *Superconductor Science and Technology*, vol. 28, no. 12, p. 124005, 2015.

[61] N. Bykovsky, D. Uglietti, K. Sedlak, B. Stepanov, R. Wesche, and P. Bruzzone, “Performance evolution of 60 ka hts cable prototypes in the edipo test facility,” *Superconductor Science and Technology*, vol. 29, no. 8, p. 084002, 2016.

[62] G. Celentano *et al.*, “Design of an industrially feasible twisted-stack hts cable-in-conduit conductor for fusion application,” *IEEE transactions on applied superconductivity*, vol. 24, no. 3, pp. 1–5, 2013.

[63] G. De Marzi *et al.*, “Bending tests of hts cable-in-conduit conductors for high-field magnet applications,” *IEEE Transactions on Applied Superconductivity*, vol. 26, no. 4, pp. 1–7, 2016.

[64] S. Hahn, D. K. Park, J. Bascunan, and Y. Iwasa, "Hts pancake coils without turn-to-turn insulation," *IEEE transactions on applied superconductivity*, vol. 21, no. 3, pp. 1592–1595, 2010.

[65] S. Kim, A. Saitou, J. Joo, and T. Kadota, "The normal-zone propagation properties of the non-insulated hts coil in cryocooled operation," *Physica C: Superconductivity and its applications*, vol. 471, no. 21-22, pp. 1428–1431, 2011.

[66] K. R. Bhattarai, K. Kim, S. Kim, S. Lee, and S. Hahn, "Quench analysis of a multiwidth no-insulation 7-t 78-mm rebco magnet," *IEEE Transactions on Applied Superconductivity*, vol. 27, no. 4, pp. 1–5, 2017.

[67] M. Cho, S. Noguchi, J. Bang, J. Kim, U. Bong, J. T. Lee, S. B. An, K. R. Bhattarai, K. Kim, K. Kim, *et al.*, "Combined circuit model to simulate post-quench behaviors of no-insulation hts coil," *IEEE Transactions on Applied Superconductivity*, vol. 29, no. 5, pp. 1–5, 2019.

[68] Y. Wang, W. K. Chan, and J. Schwartz, "Self-protection mechanisms in no-insulation (re) ba2cu3ox high temperature superconductor pancake coils," *Superconductor Science and Technology*, vol. 29, no. 4, p. 045007, 2016.

[69] O. Kwon, K. Kim, Y. Choi, H. Shin, S. Hahn, Y. Iwasa, and H. Lee, "Effects of turn-to-turn compactness in the straight sections of hts racetrack coils on thermal and electrical characteristics," *Superconductor Science and Technology*, vol. 26, no. 8, p. 085025, 2013.

[70] Y. Suetomi, K. Yanagisawa, H. Nakagome, M. Hamada, H. Maeda, and Y. Yanagisawa, "Mechanism of notable difference in the field delay times of no-insulation layer-wound and pancake-wound rebco coils," *Superconductor Science and Technology*, vol. 29, no. 10, p. 105002, 2016.

[71] S. Choi, H. C. Jo, Y. J. Hwang, S. Hahn, and T. K. Ko, "A study on the no insulation winding method of the hts coil," *IEEE transactions on applied superconductivity*, vol. 22, no. 3, pp. 4904004–4904004, 2011.

[72] D. Liu, W. Zhang, H. Yong, and Y. Zhou, "Numerical analysis of thermal stability and mechanical response in a no-insulation high-temperature superconducting layer-wound coil," *Superconductor Science and Technology*, vol. 32, no. 4, p. 044001, 2019.

[73] Y. Suetomi, S. Takahashi, T. Takao, H. Maeda, and Y. Yanagisawa, "A novel winding method for a no-insulation layer-wound rebco coil to provide a short

magnetic field delay and self-protect characteristics," *Superconductor Science and Technology*, vol. 32, no. 4, p. 045003, 2019.

[74] T. Oki, A. Ikeda, T. Wang, A. Ishiyama, S. Noguchi, K. Monma, T. Watanabe, and S. Nagaya, "Evaluation on quench protection for no-insulation rebco pancake coil," *IEEE Transactions on Applied Superconductivity*, vol. 26, no. 4, pp. 1–5, 2016.

[75] S. Noguchi, R. Miyao, H. Okusa, T. Tatsuta, H. Ueda, and S. Kim, "Turn-to-turn contact resistance measurement of no-insulation rebco pancake coils," *IEEE Transactions on Applied Superconductivity*, vol. 29, no. 5, pp. 1–5, 2019.

[76] T. Wang, S. Noguchi, X. Wang, I. Arakawa, K. Minami, K. Monma, A. Ishiyama, S. Hahn, and Y. Iwasa, "Analyses of transient behaviors of no-insulation rebco pancake coils during sudden discharging and overcurrent," *IEEE Transactions on Applied Superconductivity*, vol. 25, no. 3, pp. 1–9, 2015.

[77] H. Song and Y. Wang, "Simulations of nonuniform behaviors of multiple no-insulation (re) ba 2 cu 3 o 7-x hts pancake coils during charging and discharging," *IEEE Transactions on Applied Superconductivity*, vol. 26, no. 4, pp. 1–1, 2015.

[78] Y. Kakimoto, T. Ichikawa, H. Onoshita, T. Kinpara, A. Ishiyama, and S. Noguchi, "Evaluation of electromagnetic behavior of no-insulation rebco pancake coil with multiple defects," *IEEE Transactions on Applied Superconductivity*, vol. 29, no. 5, pp. 1–5, 2019.

[79] S. Hahn, Y. Kim, J. Ling, J. Voccio, D. K. Park, J. Bascuñán, H.-J. Shin, H. Lee, and Y. Iwasa, "No-insulation coil under time-varying condition: Magnetic coupling with external coil," *IEEE transactions on applied superconductivity*, vol. 23, no. 3, pp. 4601705–4601705, 2013.

[80] A. Zappatore, W. H. Fietz, R. Heller, L. Savoldi, M. J. Wolf, and R. Zanino, "A critical assessment of thermal–hydraulic modeling of hts twisted-stacked-tape cable conductors for fusion applications," *Superconductor Science and Technology*, vol. 32, no. 8, p. 084004, 2019.

[81] C. P. Bean, "Magnetization of hard superconductors," *Physical review letters*, vol. 8, no. 6, p. 250, 1962.

[82] C. P. Bean, "Magnetization of high-field superconductors," *Reviews of modern physics*, vol. 36, no. 1, p. 31, 1964.

[83] W. Norris, "Calculation of hysteresis losses in hard superconductors carrying ac: isolated conductors and edges of thin sheets," *Journal of Physics D: Applied Physics*, vol. 3, no. 4, p. 489, 1970.

[84] E. H. Brandt and M. Indenbom, "Type-ii-superconductor strip with current in a perpendicular magnetic field," *Physical review B*, vol. 48, no. 17, p. 12893, 1993.

[85] Y. Mawatari, "Critical state of periodically arranged superconducting-strip lines in perpendicular fields," *Physical Review B*, vol. 54, no. 18, p. 13215, 1996.

[86] Y. Iwasa, *Case studies in superconducting magnets: design and operational issues.* Springer science & business media, 2009.

[87] K. Kajikawa, K. Funaki, K. Shikimachi, N. Hirano, and S. Nagaya, "Numerical evaluation of ac loss properties in assembled superconductor strips exposed to perpendicular magnetic field," *Physica C: Superconductivity*, vol. 469, no. 15-20, pp. 1436–1438, 2009.

[88] H. London, "Alternating current losses in superconductors of the second kind," *Phys. Letters*, vol. 6, 1963.

[89] N. Schönborg, *"Development of loss models for a high-temperature superconducting tape"*. Phd thesis, Royal institute of technology, Stockholm, Sweden, December 2001.

[90] N. Schönborg, "Hysteresis losses in a thin high-temperature superconductor strip exposed to ac transport currents and magnetic fields," *Journal of Applied Physics*, vol. 90, no. 6, pp. 2930–2933, 2001.

[91] S. Awaji *et al.*, "Ac losses of an hts insert in a 25-t cryogen-free superconducting magnet," *IEEE Transactions on Applied Superconductivity*, vol. 25, no. 3, pp. 1–5, 2014.

[92] K. Kajikawa, S. Awaji, and K. Watanabe, "Ac loss evaluation of an hts insert for high field magnet cooled by cryocoolers," *Cryogenics*, vol. 80, pp. 215–220, 2016.

[93] K. Kajikawa, S. Awaji, and K. Watanabe, "Numerical evaluation of ac losses in an hts insert coil for high field magnet during its energization," *arXiv preprint arXiv:1405.7765*, 2014.

[94] F. Sirois and F. Grilli, "Potential and limits of numerical modelling for supporting the development of hts devices," *Superconductor Science and Technology*, vol. 28, no. 4, p. 043002, 2015.

[95] F. Grilli, R. Brambilla, and L. Martini, "Modeling high-temperature superconducting tapes by means of edge finite elements," *IEEE Transactions on Applied Superconductivity*, vol. 17, no. 2, pp. 3155–3158, 2007.

[96] B. Shen, F. Grilli, and T. Coombs, "Overview of h-formulation: A versatile tool for modeling electromagnetics in high-temperature superconductor applications," *IEEE access*, vol. 8, pp. 100403–100414, 2020.

[97] B. Shen, F. Grilli, and T. Coombs, "Review of the ac loss computation for hts using h formulation," *Superconductor Science and Technology*, vol. 33, no. 3, p. 033002, 2020.

[98] K. Kajikawa, T. Hayashi, R. Yoshida, M. Iwakuma, and K. Funaki, "Numerical evaluation of ac losses in hts wires with 2d fem formulated by self magnetic field," *IEEE transactions on applied superconductivity*, vol. 13, no. 2, pp. 3630–3633, 2003.

[99] F. Liang, W. Yuan, M. Zhang, Z. Zhang, J. Li, S. Venuturumilli, and J. Patel, "Ac loss modelling and experiment of two types of low-inductance solenoidal coils," *Superconductor Science and Technology*, vol. 29, no. 11, p. 115006, 2016.

[100] V. Lahtinen, A. Stenvall, F. Sirois, and M. Pellikka, "A finite element simulation tool for predicting hysteresis losses in superconductors using an h-oriented formulation with cohomology basis functions," *Journal of Superconductivity and Novel Magnetism*, vol. 28, pp. 2345–2354, 2015.

[101] Z. Hong, *Numerical solution of critical state in superconductivity by finite element method.* PhD thesis, University of Cambridge, 2008.

[102] S. Stavrev, F. Grilli, B. Dutoit, N. Nibbio, E. Vinot, I. Klutsch, G. Meunier, P. Tixador, Y. Yang, and E. Martinez, "Comparison of numerical methods for modeling of superconductors," *IEEE transactions on magnetics*, vol. 38, no. 2, pp. 849–852, 2002.

[103] S. Stavrev, F. Grilli, B. Dutoit, I. Klutsch, E. Vinot, P. Tixador, G. Meunier, P. Skov-Hansen, and J. B. Hansen, "Numerical modelling of bi-2223 multifilamentary tapes with position-dependent jc," *Physica C: Superconductivity*, vol. 372, pp. 1800–1805, 2002.

[104] S. Otten and F. Grilli, “Simple and fast method for computing induced currents in superconductors using freely available solvers for ordinary differential equations,” *IEEE transactions on applied superconductivity*, vol. 29, no. 8, pp. 1–8, 2019.

[105] E. H. Brandt, “Superconductors of finite thickness in a perpendicular magnetic field: Strips and slabs,” *Physical review B*, vol. 54, no. 6, p. 4246, 1996.

[106] N. Nibbio, S. Stavrev, and B. Dutoit, “Finite element method simulation of ac loss in hts tapes with b-dependent ej power law,” *IEEE transactions on applied superconductivity*, vol. 11, no. 1, pp. 2631–2634, 2001.

[107] H. Tonsho, S. Fukui, T. Sato, M. Yamaguchi, S. Torii, T. Takao, and K. Ueda, “Theoretical and experimental study on ac loss in hts tape in ac magnetic field carrying ac transport current,” *IEEE transactions on applied superconductivity*, vol. 13, no. 2, pp. 2368–2371, 2003.

[108] N. Amemiya, “" numerical modelings of superconducting wires for ac loss calculations"," finite element analysis of ac loss in non-twisted bi-2223 tape carrying ac transport current and/or exposed to dc or ac external magnetic field,” in *ICMC Topical Conference 1998*, 1998.

[109] A. Stenvall and T. Tarhasaari, “Programming finite element method based hysteresis loss computation software using non-linear superconductor resistivity and t- φ formulation,” *Superconductor Science and Technology*, vol. 23, no. 7, p. 075010, 2010.

[110] F. Grilli, S. Stavrev, Y. Le Floch, M. Costa-Bouzo, E. Vinot, I. Klutsch, G. Meunier, P. Tixador, and B. Dutoit, “Finite-element method modeling of superconductors: From 2-d to 3-d,” *IEEE Transactions on Applied Superconductivity*, vol. 15, no. 1, pp. 17–25, 2005.

[111] N. Enomoto and N. Amemiya, “Electromagnetic field analysis of rectangular high tc superconductor with large aspect ratio,” *Physica C: Superconductivity*, vol. 412, pp. 1050–1055, 2004.

[112] E. Berrospe-Juarez, F. Trillaud, V. M. Zermeño, F. Grilli, H. W. Weijers, and M. D. Bird, “Screening currents and hysteresis losses in the rebco insert of the 32 t all-superconducting magnet using ta homogenous model,” *IEEE Transactions on Applied Superconductivity*, vol. 30, no. 4, pp. 1–5, 2020.

[113] F. Liang, S. Venuturumilli, H. Zhang, M. Zhang, J. Kvitkovic, S. Pamidi, Y. Wang, and W. Yuan, "A finite element model for simulating second generation high temperature superconducting coils/stacks with large number of turns," *Journal of Applied Physics*, vol. 122, no. 4, 2017.

[114] T. Benkel, M. Lao, Y. Liu, E. Pardo, S. Wolfstädter, T. Reis, and F. Grilli, "T–a-formulation to model electrical machines with hts coated conductor coils," *IEEE Transactions on Applied Superconductivity*, vol. 30, no. 6, pp. 1–7, 2020.

[115] C. R. Vargas-Llanos, S. Lengsfeld, and F. Grilli, "Ta formulation for the design and ac loss calculation of a superconducting generator for a 10 mw wind turbine," *IEEE Access*, vol. 8, pp. 208767–208778, 2020.

[116] S. Fu, M. Qiu, J. Zhu, H. Zhang, J. Gong, X. Zhao, W. Yuan, and J. Guo, "Numerical study on ac loss properties of hts cable consisting of ybco coated conductor for hts power devices," *IEEE Transactions on Applied Superconductivity*, vol. 28, no. 4, pp. 1–5, 2018.

[117] A. Stenvall, V. Lahtinen, and M. Lyly, "An h-formulation-based three-dimensional hysteresis loss modelling tool in a simulation including time varying applied field and transport current: the fundamental problem and its solution," *Superconductor Science and Technology*, vol. 27, no. 10, p. 104004, 2014.

[118] H. Zhang, M. Zhang, and W. Yuan, "An efficient 3d finite element method model based on the t–a formulation for superconducting coated conductors," *Superconductor Science and Technology*, vol. 30, no. 2, p. 024005, 2016.

[119] E. Vinot, *Modélisation des supraconducteurs HTC Applications au calcul des pertes AC*. PhD thesis, Institut National Polytechnique de Grenoble-INPG, 2000.

[120] J. K. Sykulski, M. Rotaru, and R. L. Stoll, "2d modeling of field diffusion and ac losses in high temperature superconducting tapes," *IEEE transactions on magnetics*, vol. 36, no. 4, pp. 1178–1182, 2000.

[121] J. Sykulski, R. Stoll, A. Mahdi, and C. Please, "Modelling htc superconductors for ac power loss estimation," *IEEE Transactions on magnetics*, vol. 33, no. 2, pp. 1568–1571, 1997.

[122] J. Sykulski, M. Rotaru, and R. Stoll, "Highly non-linear field diffusion in htc superconducting tapes," *COMPEL-The international journal for computation and mathematics in electrical and electronic engineering*, vol. 18, no. 2, pp. 215–224, 1999.

[123] E. Vinot, G. Meunier, and P. Tixador, "Different formulations to model superconductors," *IEEE Transactions on Magnetics*, vol. 36, no. 4, pp. 1226–1229, 2000.

[124] C. Multiphysics, "Introduction to comsol multiphysics®," *COMSOL Multiphysics, Burlington, MA, accessed Feb*, vol. 9, p. 2018, 1998.

[125] A. Campbell, "An introduction to numerical methods in superconductors," *Journal of superconductivity and novel magnetism*, vol. 24, no. 1-2, pp. 27–33, 2011.

[126] A. Campbell, "A new method of determining the critical state in superconductors," *Superconductor Science and Technology*, vol. 20, no. 3, p. 292, 2007.

[127] S. Kasai and N. Amemiya, "Numerical analysis of magnetization loss in finite-length multifilamentary ybco coated conductors," *IEEE transactions on applied superconductivity*, vol. 15, no. 2, pp. 2855–2858, 2005.

[128] A. E. Ruehli, "Equivalent circuit models for three-dimensional multiconductor systems," *IEEE Transactions on Microwave theory and techniques*, vol. 22, no. 3, pp. 216–221, 1974.

[129] L. Prigozhin and V. Sokolovsky, "Computing ac losses in stacks of high-temperature superconducting tapes," *Superconductor Science and Technology*, vol. 24, no. 7, p. 075012, 2011.

[130] E. Pardo, A. Sanchez, and C. Navau, "Magnetic properties of arrays of superconducting strips in a perpendicular field," *Physical Review B*, vol. 67, no. 10, p. 104517, 2003.

[131] V. M. Zermeno, A. B. Abrahamsen, N. Mijatovic, B. B. Jensen, and M. P. Sørensen, "Calculation of alternating current losses in stacks and coils made of second generation high temperature superconducting tapes for large scale applications," *Journal of Applied Physics*, vol. 114, no. 17, 2013.

[132] V. M. Zermeño and F. Grilli, "3d modeling and simulation of 2g hts stacks and coils," *Superconductor Science and Technology*, vol. 27, no. 4, p. 044025, 2014.

[133] F. Romanelli *et al.*, "Fusion electricity: A roadmap to the realization of fusion energy," *U.K.: Eur. Fusion Develop. Agreement*, 2012.

[134] V. Corato *et al.*, "The demo magnet system–status and future challenges," *Fusion engineering and design*, vol. 174, p. 112971, 2022.

[135] V. Corato *et al.*, "Strategy for developing the eu-demo magnet system in the concept design phase," *IEEE Transactions on Applied Superconductivity*, vol. 32, no. 6, pp. 1–7, 2022.

[136] K. Sedlak *et al.*, "Advance in the conceptual design of the european demo magnet system," *Superconductor science and technology*, vol. 33, no. 4, p. 044013, 2020.

[137] L. Savoldi *et al.*, "Thermal–hydraulic modeling of a novel hts cicc for nuclear fusion applications," *IEEE Transactions on Applied Superconductivity*, vol. 26, no. 3, pp. 1–7, 2016.

[138] D. Uglietti, N. Bykovsky, R. Wesche, and P. Bruzzone, "Development of hts conductors for fusion magnets," *IEEE Transactions on Applied Superconductivity*, vol. 25, no. 3, pp. 1–6, 2014.

[139] R. Wesche, X. Sarasola, K. Sedlak, N. Bykovsky, B. Stepanov, D. Uglietti, and P. Bruzzone, "Demo central solenoid design based on the use of hts sections at highest magnetic field," *IEEE Transactions on Applied Superconductivity*, vol. 28, no. 3, pp. 1–5, 2018.

[140] R. Liu, W. Yang, D. Song, J. Zhu, and X. Li, "Effect of dynamic resistance on ac loss in stacked superconducting tapes," *IEEE Transactions on Applied Superconductivity*, vol. 30, no. 4, pp. 1–5, 2020.

[141] A. Zappatore, G. De Marzi, and D. Uglietti, "Impact of hysteresis losses in hybrid (hts-lts) coils for fusion applications," *IEEE Access*, 2023.

[142] K. Yagotintsev, V. Anvar, P. Gao, M. Dhalle, T. Haugan, D. Van Der Laan, J. Weiss, M. Hossain, and A. Nijhuis, "Ac loss and contact resistance in rebco corc®, roebel, and stacked tape cables," *Superconductor science and technology*, vol. 33, no. 8, p. 085009, 2020.

[143] J. Han, W.-S. Kim, K. Choi, and J.-K. Lee, "Magnetization loss of multilayered corc according to various winding types," *IEEE Transactions on Applied Superconductivity*, vol. 32, no. 6, pp. 1–5, 2022.

[144] A. Radovinsky and S. Kuznetsov, "Motive systems comprising a high temperature superconductor (hts) cable," Dec. 30 2021. US Patent App. 17/358,261.

[145] M. Breschi, M. Ciotti, and P. L. Ribani, "Analysis of inductance coefficients in multistrand cables: analytical, numerical, and experimental results," *IEEE transactions on applied superconductivity*, vol. 15, no. 3, pp. 3797–3807, 2005.

[146] T. M. Inc., “Matlab version: 9.13.0 (r2022b),” 2022.

[147] G. De Marzi, M. Corradini, L. Muzzi, L. Giannini, and A. D. Corte, “High field-rate losses in cable-in-conduit- conductors carrying transport current,” *presented at CHATS, 2021*, pp. 1–26, doi: 10.13140/RG.2.2.33159.93607.

[148] S. Hahn, Y. Kim, J. Song, J. Voccio, J. Ling, J. Bascunan, and Y. Iwasa, “A 78-mm/7-t multi-width no-insulation rebco magnet: Key concept and magnet design,” *IEEE transactions on applied superconductivity*, vol. 24, no. 3, pp. 1–5, 2013.

[149] T. Lécrevisse and Y. Iwasa, “A (re) bco pancake winding with metal-as-insulation,” *IEEE Transactions on Applied Superconductivity*, vol. 26, no. 3, pp. 1–5, 2016.

[150] S. Yoon, J. Kim, K. Cheon, H. Lee, S. Hahn, and S.-H. Moon, “26 t 35 mm all-gdba2cu3o7–x multi-width no-insulation superconducting magnet,” *Superconductor Science and Technology*, vol. 29, no. 4, p. 04LT04, 2016.

[151] J. Liu, Y. Dai, and L. Li, “Progress in the development of a 25 t all superconducting nmr magnet,” *Cryogenics*, vol. 79, pp. 79–84, 2016.

[152] S. Noguchi, R. Itoh, S. Hahn, and Y. Iwasa, “Numerical simulation of superconducting coil wound with no-insulation nbti wire,” *IEEE transactions on applied superconductivity*, vol. 24, no. 3, pp. 1–4, 2013.

[153] G. Kim, A. Musso, J. Bang, J. T. Lee, C. Im, K. Choi, J. Kim, M. Breschi, K. J. Han, and S. Hahn, “A numerical method for spatially-distributed transient simulation to replicate nonlinear ‘defect-irrelevant’behaviors of no-insulation hts coil,” *Superconductor Science and Technology*, vol. 34, no. 11, p. 115004, 2021.

[154] A. Musso, G. Angeli, M. Ascade, M. Bocchi, G. Pasini, P. Ribani, V. Rossi, and M. Breschi, “Comparing electrodynamic losses during transport current cycles in insulated and non-insulated hts coils,” *IEEE Transactions on Applied Superconductivity*, vol. 33, no. 5, pp. 1–5, 2023.

[155] S. Kim, S. Hahn, K. Kim, and D. Larbalestier, “Method for generating linear current-field characteristics and eliminating charging delay in no-insulation superconducting magnets,” *Superconductor Science and Technology*, vol. 30, no. 3, p. 035020, 2017.

[156] M.-H. Sohn, K. Sim, B. Eom, H.-S. Ha, H.-Y. Kim, and K. Seong, “Controllability of the contact resistance of 2g hts coil with metal insulation,” *IEEE Transactions on Applied Superconductivity*, vol. 28, no. 3, pp. 1–5, 2018.

[157] D. G. Yang, J.-B. Song, Y. H. Choi, S.-G. Kim, Y. S. Choi, and H. Lee, "A study on electrical characteristics of multilayered metallic-insulation coils," *IEEE Transactions on Applied Superconductivity*, vol. 27, no. 4, pp. 1–6, 2017.

[158] A. Musso, G. Angeli, M. Ascade, M. Bocchi, P. L. Ribani, V. Rossi, A. Valzasina, and M. Breschi, "Electrical characteristics of hts coils with and without insulation in a layer-wound configuration," *IEEE Transactions on Applied Superconductivity*, vol. 31, no. 5, pp. 1–5, 2021.

[159] L. Qin, L. Wang, J. Liu, K. Wang, B. Zhou, H. Sun, and Q. Wang, "Refined circuit model for current distribution of the no-insulation hts insert magnet," *Superconductor Science and Technology*, vol. 34, no. 7, p. 075002, 2021.

[160] S. Noguchi and S. Hahn, "A newly developed screening current simulation method for rebco pancake coils based on extension of peec model," *Superconductor science and technology*, vol. 35, no. 4, p. 044005, 2022.

[161] N. Riva, F. Sirois, C. Lacroix, W. De Sousa, B. Dutoit, and F. Grilli, "Resistivity of rebco tapes in overcritical current regime: Impact on superconducting fault current limiter modeling," *Superconductor Science and Technology*, vol. 33, no. 11, p. 114008, 2020.

[162] F. Verhulst, *Nonlinear differential equations and dynamical systems.* Springer Science & Business Media, 2006.

[163] P. Kundur, "Power system stability," *Power system stability and control*, vol. 10, pp. 7–1, 2007.

[164] L. Chua, C. Desoer, and E. Kuh, *Linear and Nonlinear Circuits.* Electrical & electronic engineering, McGraw-Hill, 1987.

[165] P. Dimo, "Nodal analysis of power systems," 1975.

[166] J. R. Cash and A. H. Karp, "A variable order runge-kutta method for initial value problems with rapidly varying right-hand sides," *ACM Transactions on Mathematical Software (TOMS)*, vol. 16, no. 3, pp. 201–222, 1990.

[167] U. M. Ascher and L. R. Petzold, *Computer methods for ordinary differential equations and differential-algebraic equations*, vol. 61. Siam, 1998.

[168] H. William, J. E. Kemmerly, and S. M. Durbin, *Engineering circuit analysis.* McGraw-Hill Higher Education, 2007.

[169] A. C. Hindmarsh, P. N. Brown, K. E. Grant, S. L. Lee, R. Serban, D. E. Shumaker, and C. S. Woodward, “Sundials: Suite of nonlinear and differential/algebraic equation solvers,” *ACM Transactions on Mathematical Software (TOMS)*, vol. 31, no. 3, pp. 363–396, 2005.

[170] A. Musso, M. Breschi, P. L. Ribani, and F. Grilli, “Analysis of ac loss contributions from different layers of hts tapes using the a- v formulation model,” *IEEE Transactions on Applied Superconductivity*, vol. 31, no. 2, pp. 1–11, 2020.

[171] M. Hosea and L. Shampine, “Analysis and implementation of tr-bdf2,” *Applied Numerical Mathematics*, vol. 20, no. 1-2, pp. 21–37, 1996.

[172] E. Süli and D. F. Mayers, *An introduction to numerical analysis.* Cambridge university press, 2003.